ΠΑΝΕΠΙΣΤΗΜΙΟ ΙΩΑΝΝΙΝΩΝ

ΣΧΟΛΗ ΘΕΤΙΚΩΝ ΕΠΙΣΤΗΜΩΝ

ΤΜΗΜΑ ΦΥΣΙΚΗΣ

Μικροσκοπία Φωτοϊονισμού στο Άτομο του Μαγνησίου

Παναγιώτης Καλαϊτζής

ΔΙΔΑΚΤΟΡΙΚΗ ΔΙΑΤΡΙΒΗ

ΙΩΑΝΝΙΝΑ 2020

UNIVERSITY OF IOANNINA

SCHOOL OF SCIENCES

DEPARTMENT OF PHYSICS

Photoionization Microscopy of the Magnesium Atom

Panagiotis Kalaitzis

Ph.D. THESIS

IOANNINA 2020

Advisory Committee:

Samuel Cohen, Associate Professor, Physics Department, University of Ioannina (Supervisor)

Constantine Kosmidis, Professor, Physics Department, University of Ioannina

Spyridon Kaziannis, Assistant Professor, Physics Department, University of Ioannina

Examination Committee:

Samuel Cohen, Associate Professor, Physics Department, University of Ioannina (Supervisor)

Constantine Kosmidis, Professor, Physics Department, University of Ioannina

Spyridon Kaziannis, Assistant Professor, Physics Department, University of Ioannina

Emmanouil Benis, Assistant Professor, Physics Department, University of Ioannina

Paraskevas Tzallas, Research Director, FORTH, Institute of Electronic Structure and Laser, Heraklion Crete

Christian Bordas, Directeur de recherche, CNRS, Institut Lumière Matière, Université Claude Bernard Lyon 1, Lyon, France

Franck Lépine, Chargé de recherche, CNRS, Institut Lumière Matière, Université Claude Bernard Lyon 1, Lyon, France

Dedication

Η παρούσα ερευνητική εργασία εκπονήθηκε στο Εργαστήριο Ατομικής και μοριακής Φυσικής (ATOMOL) του Τμήματος Φυσικής, του Πανεπιστημίου Ιωαννίνων και σε συνεργασία με το Γαλλικό Ινστιτούτο Institut Lumière Matière, CNRS, Université Claude Bernard, Lyon 1. Μέρη της έρευνας χρηματοδοτήθηκαν από Ευρωπαϊκούς και κρατικούς πόρους. Η παρούσα διατριβή αποτελεί προϊόν συλλογικού μόχθου προσώπων στα οποία θα ήθελα να αναφερθώ ατομικά.

Ευχαριστώ τα μέλη της τριμελούς συμβουλευτικής επιτροπής, δηλαδή

…τον επιβλέποντα καθηγητή, κ. Σαμουήλ Κοέν για την υπομονή και την εμπιστοσύνη που έδειξε σε εμένα τα 5 χρόνια της συνεργασία μας. Υπήρξε ο κύριος καθοδηγητής και εμπνευστής του κάθε βήματος της έρευνας καθώς και πρότυπο εργατικότητας για εμένα.

…τον κ. Κωσταντίνο Κοσμίδη για θερμή του υποδοχή στο εργαστήριο και την εμπιστοσύνη που μου έδειξε από την πρώτη μέρα. Επίσης, είχα την αμέριστη στήριξη του σε όλες της πτυχές του βίου μου ως υποψήφιος διδάκτορας.

…τον κ. Σπυρίδων Καζιάννη για την στήριξη του και την θέρμη που επέδειξε στην αντιμετώπιση όλων των δυσκολιών που αντιμετώπισα στο εργαστήριο.

Θα ήθελα επίσης να ευχαριστήσω,

…τον κ. Σωτήριο Ντανάκα για τον άψογο επαγγελματισμό του και την καθημερινή του ψυχολογική υποστήριξη σε εμένα.

…τους κ.κ. Christian Bordas και Franck Lépine για την εποικοδομητική και ευχάριστη συνεργασία μας καθώς και την φιλοξενία τους στην πόλη της Λυών.

…τον κ. Εμμανουήλ Μπενή για την συνεργασία μας και την συμμετοχή του στην εξεταστική επιτροπή αυτής της διατριβής.

…τον κ. Παρασκευά Τζάλλα για την συμμετοχή του στην εξεταστική επιτροπή αυτής της διατριβής.

Ευχαριστώ ακόμη τους καθηγητές Α. Οικιάδη και Κ. Φουντά, καθώς και τα μέλη του τεχνικού προσωπικού Ε. Δημητριάδη και Π. Τριανταφύλλου. Στην δουλειά αυτή χρησιμοποιήθηκε εξοπλισμός στον οποίον έχουν βασιστεί προηγούμενες εργασίες· μεταξύ άλλων και των κ.κ. Α. Δημητρίου και Ε. Παύλου. Κατά την διάρκεια της μελέτης είχα την τύχη να εργάζομαι πλάι στους διδακτορικούς φοιτητές και φίλους Κ. Φερεντίνου, Ε. Κεχάογλου και Δ. Σπασόπουλο. Ευχαριστώ τους Γιώργο Σταματίου και Κέλη Κουμψάκη και όλους τους φίλους μου, που στάθηκαν πλάι μου σε αυτήν την προσπάθεια. Ιδιαίτερα ευχαριστώ την σύντροφο μου Αλεξάνδρα Σινάνη για τις υπέροχες στιγμές που περάσαμε μαζί από τα πρώτα έτη του πτυχίου μας. Τέλος, ευχαριστώ την οικογένεια μου για την ολόπλευρη στήριξη τους. Ήταν και θα είναι για πάντα οι ήρωες μου. Γνωρίζω ότι θα έχω τους έχω στο πλευρό μου, σε κάθε μου βήμα.

Αφιερώνω αυτή την δουλειά στα αγαπητά μου ξαδέρφια, Ερμιόνη και Γιάννη.

Είμαστε ρεαλιστές, επιδιώκουμε το αδύνατο.

Abstract

Photoionization Microscopy (PM) is an experimental technique aiming at the observation of the squared modulus of the wave function of electrons emitted during the photoionization of neutral atoms in the presence of a uniform static electric field. This is achieved by imaging the two-dimensional flux of these slow (meV) photoelectrons. The present work is devoted to the magnesium atom (Z=12), ionized by two-photon absorption out of its ground state. Particularly, in this thesis the following three directions have been examined:

The first direction concerns the recording and characterization of Mg resonant images. Indeed, images exhibiting resonant features are recorded just above the saddle point energy. Although these manifestations are found to be rather faint, they have been achieved for the heaviest atom so far, since all other resonant images were observed in small-size atoms ($Z\leq3$).

In the second direction, the aim is the detailed recording of the (primarily non-resonant) momentum distributions of the outgoing electron transversely to the static electric field. The purpose here is the exploration of the global (i.e. of that met in any atom and irrespective of excitation conditions) information these distributions may provide through the analysis of their rich interference patterns. Particularly, it is shown that the oscillations of the signal at the center of the images as a function of energy, is closely related to the dynamics of the electron motion towards the detector.

Finally, in the third direction we explore the effects observed in slow photoelectron images when the linear polarization vector of the ionizing-laser is rotated with respect to the static field axis. It is shown that two-photon ionization out of the Mg m=0 initial state allows for the population of $|m|$=0,1,2 final Stark states, causing observable m-beating effects. Additionally, based on these observations, we discuss the challenges posed on the applicability of tomographic reconstruction techniques when meV electrons are involved.

In all of the above directions, experimental results are supported and verified by our hydrogenic non-perturbative calculations.

Περίληψη

Η κβαντική περιγραφή των φυσικών συστημάτων είναι βασισμένη στην έννοια της κυματοσυνάρτησης. Νέες τεχνικές στοχεύουν στην ανακατασκευή ή την παρατήρηση αυτής μέσω τομογραφικών τεχνικών ή της χρήσης «ασθενών» μετρήσεων αντίστοιχα. Επιπλέον άλλες τεχνικές όπως η ηλεκτρονική μικροσκοπία σήραγγας και η τεχνική που αφορά την παρούσα εργασία, Μικροσκοπία Φωτοϊονισμού (ΜΦ), στοχεύουν στην απευθείας καταγραφή του τετραγωνισμένου μέτρου της ηλεκτρονιακής κυματοσυνάρτησης (πυκνότητα πιθανότητας). Πιο συγκεκριμένα η ΜΦ είναι μια απεικονιστική τεχνική που έχει ως στόχο την καταγραφή της ροής του ηλεκτρονιακού ρεύματος, το οποίο εκπέμπεται κατά την διαδικασία φωτοϊονισμού ουδετέρου ατόμου, υπό την παρουσία στατικού και ομογενούς πεδίου. Υπό αυτές τις συνθήκες η κυματοσυνάρτηση του εκπεμπόμενου ηλεκτρονίου είναι δέσμια στην διεύθυνση κάθετα στο πεδίο ενώ εκτείνεται σε μακροσκοπικές αποστάσεις στην διεύθυνση παράλληλα με αυτό, εξ ού και ο όρος μικροσκοπία. Η καταγραφή της ροής του ηλεκτρονιακού ρεύματος επιτυγχάνετε με χρήση ανιχνευτή υψηλής χωρικής διακριτικής ικανότητας. Στην περίπτωση όπου τα ηλεκτρόνια είναι μικρής κινητικής ενέργειας την στιγμή του φωτοϊονισμού («αργά» ηλεκτρόνια), στην οθόνη παρατηρείται η εμφάνιση κροσσών κβαντικής συμβολής. Αυτό το μοτίβο συμβολής συνδέεται άμεσα με την πυκνότητα πιθανότητας της ηλεκτρονιακής κυματοσυνάρτησης του φωτοηλεκτρονίου και έτσι η ΜΦ είναι μια από τις λίγες τον αριθμό πειραματικές τεχνικές που στοχεύουν στην άμεση μέτρηση του τετραγωνισμένου μέτρου της ηλεκτρονιακής κυματοσυνάρτησης, δηλαδή χωρίς την χρήση ανακατασκευαστικών τεχνικών ή άλλων υποθέσεων.

Η περιγραφή του μη-διαταρατικού φαινομένου Stark βασίζεται στο ημι-παραβολικό (ή ισοδύναμα στο παραβολικό και το μικτό) σύστημα συντεταγμένων (χ,υ,φ). Η παρουσία του ηλεκτρικού πεδίου σε συνδυασμό με την χρήση αργών ηλεκτρονίων είναι υπεύθυνα για την εμφάνιση μοναδικών χαρακτηριστικών στις εικόνες των φωτοηλεκτρονίων. Ενδιαφέρον είναι το γεγονός πως για ενέργειες μικρότερες της ενέργειας ιονισμού απουσία πεδίου και μεγαλύτερες από την ενέργεια σαγματικού σημείου, συνυπάρχουν καταστάσεις του συνεχούς και συντονισμοί (ιονισμός μέσω του φαινομένου σήραγγας). Τα πρώτα πειράματα στο άτομο του Ξένου (Xe, Z=54) αποτύπωσαν μια ομαλή συμπεριφορά της θέσης και του αριθμού των κόμβων των εικόνων ΜΦ ως συνάρτηση της ενέργειας. Αυτή η συμπεριφορά δείχνει να αγνοεί την ύπαρξη συντονισμών,

γεγονός που οφείλεται στο ότι οι καταστάσεις Stark στα πολυηλεκτρονιακά άτομα μπορούν να γραφούν ως γραμμικός συνδυασμός υδρογονικών συντονιστικών καταστάσεων και καταστάσεων του συνεχούς. Με άλλα λόγια, λόγω των αλληλεπιδράσεων μεταξύ του διεγερμένου ηλεκτρονίου και του ιόντος, ο πληθυσμός που βρίσκεται στην κατάσταση συντονισμού μεταφέρεται στις ενεργειακά εκφυλισμένες καταστάσεις του συνεχούς.

Οι θεωρητικές προβλέψεις για τα χαρακτηριστικά των εικόνων συντονισμού επαληθεύτηκαν από πειράματα στο υδρογόνο (H, Z=1) και τα μικρά άτομα του ήλιου (He, Z=2) και λίθου (Li, Z=3). Η εμφάνιση αυτών των χαρακτηριστικών επιτεύχθηκε λόγο του μικρού ατομικού αριθμού και την επιλογή της ενεργειακής περιοχής κοντά σε αλληλοαπωθούμενους συντονισμούς στα πειράματα του λιθίου και ηλίου αντιστοίχως. Στην προσπάθεια επέκτασης της μεθόδου σε μεγαλύτερα άτομα, θεωρητικές μελέτες έδειξαν ότι υπό την παρουσία βέλτιστων συνθηκών (αρκούντος στενό φασματικό εύρος, κατάλληλη επιλογή της έντασης του στατικού πεδίου) η παρατήρηση συντονισμών είναι εφικτή ακόμα και στην περίπτωση του ξένου, δηλαδή ατόμων με μεγάλο ατομικό αριθμό.

Εξαιρετικής σημασίας είναι οι πρόσφατες μελέτες που έδειξαν ότι η ενεργειακή συμπεριφορά των εικόνων του συνεχούς και οι αντίστοιχες ακτινικές κατανομές των εικόνων αυτών (τουλάχιστον στην περίπτωση εικόνων με κέντρο συμμετρίας το κέντρο της εικόνας, αζιμουθιακά συμμετρικές εικόνες) συνδέονται με την δυναμική των ηλεκτρονίων. Συγκεκριμένα, αναζητάται η διαφορά χρόνων πτήσης μεταξύ συγκεκριμένου ζεύγους ηλεκτρονιακών τροχιών από το άτομο στόχο έως και τον ανιχνευτή. Για τυπικές τιμές του πεδίου ~1 kV/cm οι χαρακτηριστικοί χρόνου του συστήματος Coulomb-Stark αφορούν χρόνους τάξης μεγέθους μερικών picosecond. Τέτοιου είδους μελέτες βασίζονται στην αντιστοίχιση χρονικών διαφορών σε διαφορές φάσης όπως αυτές αποτυπώνονται στο μοτίβο συμβολής των εικόνων.

Ακόμα, είναι γνωστό πως ο άξονας του στατικού ηλεκτρικού πεδίου επιβάλει μια προτιμητέα διεύθυνση στον χώρο. Τότε ο άξονας κβάντωσης αυτού του συστήματος είναι ο άξονας του στατικού ηλεκτρικού πεδίου όπως έχει αποδειχθεί θεωρητικά και πειραματικά. Αντιθέτως, σε εφαρμογές ηλεκτρονίων υψηλής κινητικής ενέργειας την στιγμή του φωτοϊονισμού, η κατανομή ταχυτήτων «χτίζεται» γύρο από το διάνυσμα της πόλωσης. Δηλαδή, ο άξονας κβάντωσης είναι το διάνυσμα της πόλωσης μιας δέσμης laser ενώ το στατικό πεδίο προβάλει την τρισδιάστατη κατανομή ταχυτήτων στο επίπεδο του ανιχνευτή. Έτσι, η περιστροφή της πόλωσης περιστρέφει την τρισδιάστατη κατανομή η οποία παραμένει αναλλοίωτη. Οι παραπάνω παραδοχές

χρησιμοποιούνται στην τομογραφική ανακατασκευή της τρισδιάστατης γωνιακής κατανομής ενώ η εφαρμογή των τεχνικών αυτών στις περιπτώσεις όπου αφορούν αργά ηλεκτρόνια είναι υπό μελέτη.

Η παραπάνω συζήτηση αποτέλεσε πηγή έμπνευσης της παρούσης εργασίας της οποίας ο στόχος είναι η απάντηση στα εξής ερωτήματα, όπως αυτά χωρίζονται σε τρεις επιμέρους άξονες:

(i) Η χρησιμότητα της μεθόδου της ΜΦ είναι περιορισμένη εξαιτίας του γεγονότος ότι εικόνες συντονισμού έχουν παρατηρηθεί μόνο σε μικρά άτομα. Έτσι εγείρεται το ερώτημα του εάν είναι δυνατόν να παρατηρηθούν συντονιστικές καταστάσεις σε άτομα μεγαλύτερα του λιθίου χωρίς την χρήση κάποιας εξειδικευμένης τεχνικής, π.χ. όπως η χρήση αλληλοαπωθούμενων συντονισμών.

(ii) Ποια είναι η συμπεριφορά των εικόνων και των αντίστοιχων ακτινικών τους κατανομών ως συνάρτηση της ενέργειας; Ποια τα κοινά χαρακτηριστικά μεταξύ πολυηλεκτρονιακών και υδρογονικών δεδομένων και ποια πληροφορία που σχετίζεται με την δυναμική του συστήματος μπορεί να εξαχθεί από αυτά;

και τέλος

(iii) Τι πληροφορία μπορούμε να εξάγουμε από την περιστροφή του διανύσματος γραμμικής πόλωσης της δέσμης laser σε σχέση με την διεύθυνση του στατικού ηλεκτρικού πεδίου; Επιπλέον, ποιες είναι προκλήσεις που αντιμετωπίζουν οι τεχνικές τομογραφικής ανακατασκευής σε πειράματα όπου εμπλέκονται αργά ηλεκτρόνια;

Με σκοπό την εξερεύνηση των παραπάνω ερωτημάτων, η εργασία αυτή αφορά στην μικροσκοπία φωτοϊονισμού στο άτομο του μαγνησίου με χρήση διφωτονικού σχήματος διέγερσης ξεκινώντας από την βασική κατάσταση. Τα πειραματικά δεδομένα υποστηρίχθηκαν από θεωρητικούς υπολογισμούς που περιγράφουν τον φωτοϊονισμό του υδρογόνου υπό την παρουσία στατικού πεδίου. Οι υπολογισμοί αυτοί αναφέρονται σε κλασικούς, ημι-κλασικούς και αριθμητικούς κβαντικούς υπολογισμούς στο ημι-παραβολικό σύστημα συντεταγμένων. Πέρα από την άμεση ποιοτική σύγκριση με τα δεδομένα του μαγνησίου, οι υπολογισμοί αυτοί προβλέπουν επί της αρχής τα φαινόμενα που παρατηρούνται σε αυτή την εργασία.

Πιο συγκεκριμένα, η κλασική περιγραφή επιτρέπει τον χαρακτηρισμό των τροχιών σε άμεσες (direct) και έμμεσες (indirect) τροχιές καθώς και την εξαγωγή ποσοτήτων όπως ο χρόνος πτήσης. Αυτές οι εξισώσεις κίνησης σε συνδυασμό με στοιχεία από την θεωρία σκέδασης

προβλέπουν τα γενικά χαρακτηριστικά του φωτοϊονισμού αργών ηλεκτρονίων με έναν διαισθητικό τρόπο. Στην ημι-κλασική περιγραφή το κινούμενο ηλεκτρόνιο συνδέεται με μια φάση που υπολογίζεται από το ολοκλήρωμα δράσης στην πορεία της κλασικής διαδρομής. Αυτή η επέκταση του μοντέλου προβλέπει φαινόμενα συμβολής και μπορεί να προβλέψει τα γενικά χαρακτηριστικά των εικόνων μικροσκοπίας φωτοϊονισμού.

Το κυρίως θεωρητικό εργαλείο σε αυτή την εργασία αποτελεί η κβαντική περιγραφή του *υδρογονικού* συστήματος Coulomb-Stark. Η εξίσωση Schrödinger λύνεται στο ημι-παραβολικό σύστημα συντεταγμένων, γεγονός που επιτρέπει την ανάπτυξη ενός αποδοτικού και σχετικά γρήγορου κώδικα. Σε αυτή την πιο πλήρη περιγραφή το συγκεκριμένο σχήμα διέγερσης και η αρχική κατάσταση περιγράφονται από στοιχεία πίνακα που συνδέουν τις αρχικές με τις τελικές καταστάσεις μέσω ενός διπολικού τελεστή. Το παραπάνω γεγονός καθώς και η συνεισφορά συντονιστικών καταστάσεων επηρεάζει το τελικό ρεύμα πιθανότητάς (εικόνα ΜΦ). Μελετώντας πιο γενικά διφωτονικά σχήματα διέγερσης όπου το διάνυσμα της πόλωσης είναι στραμμένο κατά μια γωνία σε σχέση με τον άξονα διεύθυνσης του πεδίου, εξάγουμε υδρογονικές εκφράσεις για το ρεύμα πιθανότητας που αποτυπώνεται στις εικόνες ΜΦ και επιπλέον υδρογονικές και πολυηλεκτρονιακές εκφράσεις για την ολική ενεργό διατομή.

Η πειραματική διάταξη που χρησιμοποιήθηκε για τις ανάγκες των μετρήσεων αποτελείται από ένα laser χρωστικής, το σύστημα βαθμονόμησης της συχνότητας της ακτινοβολίας, ένα φασματόμετρο απεικόνισης ταχυτήτων των σωματιδίων (VMI) και τέλος τα διάφορα συστήματα ανίχνευσης και καταγραφής δεδομένων. Η ακτινοβολία του ορατού βαθμονομείται με την χρήση κροσσών συμβολής από συμβολόμετρο τύπου Fabry-Perot και φασματικές γραμμές γνωστής ενέργειας με χρήση του οπτογαλβανικού φαινομένου στο αέριο μιας λυχνίας εκκένωσης. Η δεύτερη αρμονική της βαθμονομημένης ακτινοβολίας χρησιμοποιείται στις μετρήσεις και αναφέρεται σε παλμούς χρονικής διάρκειας μερικών ns ($1\text{ns} = 10^{-9}$ s) στην φασματική περιοχή του υπεριώδους ~300 nm ($1\text{ nm} = 10^{-9}$ m). Η δέσμη αυτή εισέρχεται σε κατάλληλα οπτικά στοιχεία με σκοπό την χειραγώγηση της γραμμικής της πόλωσης και έπειτα εστιάζεται σε στο θάλαμο κενού (10^{-6} mbar) στον οποίο περιέχεται το φασματόμετρο.

Η ατομική δέσμη μαγνησίου παράγεται από φούρνο εξάχνωσης και κατευθύνεται στον χώρο αλληλεπίδραση, εντός του φασματομέτρου, όπου και αλληλοεπιδρά με την δέσμη laser υπό την παρουσία στατικού ηλεκτρικού πεδίου. Η διεύθυνση της δέσμης laser είναι κάθετη στον άξονα

του φασματομέτρου και την ατομική δέσμη. Η κατασκευή του φασματομέτρου βασίζεται στην, τυπική σε φασματόμετρα απεικόνισης ταχυτήτων, γεωμετρία τριών ηλεκτροδίων. Η περιοχή αλληλεπίδρασης βρίσκεται ανάμεσα από τα πρώτα δυο ηλεκτρόδια. Το μη ομογενές ηλεκτρικό πεδίο, που δημιουργείται λόγο της μορφής των ηλεκτροδίων (το πρώτο εκ των οποίων είναι συμπαγές ενώ τα άλλα δυο έχουν κυκλική οπή) και έπειτα από κατάλληλη επιλογή των τάσεων, οδηγεί στον σχηματισμό εικόνας στον ανιχνευτή (συνθήκη απεικόνισης ταχυτήτων). Επιπλέον το φασματόμετρο περιλαμβάνει ηλεκτροστατικό φακό τύπου Einzel με την χρήση του οποίου επιτυγχάνεται η μεγέθυνση της αρχικής εικόνας έως και 20 φορές. Το φασματόμετρο καλύπτεται από προστατευτικά φύλλα φερρομαγνητικού κράματος τύπου μ-metal με σκοπό την ελαχιστοποίηση του μαγνητικού πεδίου στο εσωτερικό του. Η ανίχνευση των ιόντων/ηλεκτρονίων γίνεται από σειρά μικροκαναλικών πλακιδίων και οθόνη φωσφόρου/ανόδου. Μια ccd κάμερα καταγράφει και ολοκληρώνει το σήμα σε χρόνο μερικών χιλιάδων παλμών του laser και μεταφέρει τις εικόνες σε ηλεκτρονικό υπολογιστή.

Τα αποτελέσματα αυτής της εργασίας απαντούν στα ερωτήματα των τριών ερευνητικών αξόνων που καθορίστηκαν παραπάνω. Αρχικά, η αναζήτηση των συντονισμών επικεντρώθηκε στην ενεργειακή περιοχή ακριβώς επάνω από την ενέργεια σαγματικού σημείου όπου ο αριθμός των διαθέσιμων καταστάσεων του συνεχούς είναι μικρός. Ως πρώτο βήμα, το κβαντικό υδρογονικό μας μοντέλο μπόρεσε να αναπαράγει τα πειραματικά δεδομένα της βιβλιογραφίας. Σε αυτές τις πειραματικές υδρογονικές εικόνες, και αντίστοιχα στις θεωρητικά υπολογισμένες, καταγράφεται μια εικόνα συντονισμού. Τα χαρακτηριστικά που παρατηρούνται είναι η αύξηση του αριθμού των σκοτεινών κροσσών της εικόνας (που αντιστοιχούν σε κόμβους της κυματοσυνάρτησης) καθώς και το επαυξημένο μέγεθος της εικόνας σε σχέση πάντα με τις γειτονικές εικόνες που αντιστοιχούν σε μη-συντονιστικές καταστάσεις. Το τελευταίο χαρακτηριστικό μεταφράζεται σε μια μη-μονότονη συμπεριφορά στα γραφήματα των έξωθεν σημείων καμπής των ακτινικών κατανομών ως συνάρτηση της ενέργειας. Επιπλέον οι εικόνες των καταστάσεων του συνεχούς βρέθηκαν να παρουσιάζουν ενδιαφέρον λόγο της μονότονης μεν αλλά ασυνεχούς δε συμπεριφοράς του μεγέθους των εικόνων ως συνάρτηση της ενέργειας, γεγονός που χαρακτηρίζει τα ενεργειακά κατώφλια των μετατροπών των καναλιών σε συνεχή.

Με τα παραπάνω υδρογονικά αποτελέσματα ως οδηγό, αναλύσαμε πειραματικές εικόνες ΜΦ του μαγνησίου που αφορούν διφωτονικό ιονισμό καταστάσεων με μαγνητικούς κβαντικούς

αριθμούς $|m|=0$ και 2 (πόλωση κάθετη στο στατικό πεδίο). Λόγω της ταυτόχρονης παρουσίας καταστάσεων πολλαπλών αριθμών $|m|$ έγινε δυνατή μια εκτίμηση των δυο ενεργειών σαγματικών σημείων για $|m|=0$ και 2. Τα γραφήματα των έξωθεν σημείων καμπής των ακτινικών κατανομών ως συνάρτηση της ενέργειας βρέθηκαν να χαρακτηρίζουν κάποια από τα ενεργειακά κατώφλια των μετατροπών των καναλιών σε συνεχή, σε συμφωνία με τα υδρογονικά αποτελέσματα. Επίσης, στο μέγιστο μιας φασματικής γραμμής παρατηρήθηκε μη-μονότονη συμπεριφορά του μεγέθους των εικόνων εξαιτίας μιας εξωτερικής αχλής στις εικόνες. Αυτό το χαρακτηριστικό μπορεί να ερμηνευτεί ότι προέρχεται από τον μερικό σχηματισμό ενός επιπλέον κροσσού στην εικόνα λόγω της ταυτόχρονης παρουσίας συνεχών και μιας συντονιστικής κατάστασης. Με αυτή την μελέτη έγινε δυνατή η παρατήρηση χαρακτηριστικών συντονισμού στο μαγνήσιο. Τα χαρακτηριστικά αυτά είναι λιγότερο εμφανή από ότι στο λίθιο, πιθανώς λόγω της ταυτόχρονης διέγερσης καταστάσεων με πολλαπλούς μαγνητικούς κβαντικούς αριθμούς και το σχετικά μεγάλο ατομικό αριθμό του μαγνησίου (σε σχέση με αυτόν του λιθίου).

Όσον αφορά στον δεύτερο ερευνητικό άξονα, μελετήθηκαν οι ακτινικές κατανομές εικόνων ως συνάρτηση της ενέργειες στην περιοχή $-1\leq\varepsilon\leq1$ (ε: η ενέργεια εκφρασμένη σε μονάδες απόλυτης ενέργειας σαγματικού σημείου). Οι εικόνες ΜΦ αφορούν διφωτονικό ιονισμό καταστάσεων με μαγνητικό κβαντικό αριθμό $m=0$ (πόλωση παράλληλη στο στατικό πεδίο). Οι δισδιάστατες απεικονίσεις των ακτινικών κατανομών, $R(\rho,\varepsilon)$, παρουσιάζουν έντονα φαινόμενα κβαντικής συμβολής όπως μοτίβα που στην βιβλιογραφία αναφέρονται ως μοτίβα σκακιέρας. Τα πειραματικά δεδομένα αντιπαραβάλλονται με αντίστοιχα γραφήματα της υδρογονικής θεωρίας στην περίπτωση της μονοφωτονικής και διφωτονικής διέγερσης τελικών καταστάσεων $m=0$ από την βασική κατάσταση του υδρογόνου. Με αυτό τον τρόπο μελετήθηκαν τόσο τα φαινόμενα συμβολής που είναι καθολικά και μπορούν να περιγραφούν αρκούντος από ημι-κλασικά μοντέλα, όσο και φαινόμενα που εξαρτώνται από την αρχική κατάσταση, το σχήμα διέγερσης και το άτομο-στόχο. Η δουλειά αυτή αποτελεί έναν οδηγό των φαινομένων συμβολής στην περιοχή ασθενών ηλεκτρικών πεδίων (~1 kV/cm) και χαμηλών ενεργειών.

Ιδιαίτερα αναλύθηκε η ταλαντωτική συμπεριφορά της σκέδασης τύπου δόξης (glory) και τόξου (bow) δηλαδή, το σήμα στο κέντρο του ανιχνευτή και το έντονο σήμα στα άκρα των δακτυλίων των εικόνων ΜΦ. Πιο συγκεκριμένα το σήμα τύπου glory στο μαγνήσιο παρουσιάζει μια απλή συμπεριφορά στις θετικές ενέργειες που χαρακτηρίζεται από μια ταλάντωση μιας κάποιας φέρουσας συχνότητας και κάποια ελάχιστα ή μέγιστα συμβολής. Έπειτα έγινε σύγκριση

με τα φάσματα της υδρογονικής θεωρίας τα οποία παρουσιάζουν ταλαντωτική συμπεριφορά λόγω της παρουσίας καταστάσεων που επάγονται από το στατικό ηλεκτρικό πεδίο σε θετικές ενέργειες. Επίσης, κατ' αναλογία με προηγούμενες μελέτες της βιβλιογραφίας, έγινε μια προσπάθεια σύνδεσης της ταλάντωσης glory με τους χρόνους πτήσης (όπως υπολογίζονται κλασικά) των άμεσων τροχιών που καταλήγουν στο κέντρο του ανιχνευτή. Η εξαγόμενη πληροφορία αφορά στην δυναμική των ηλεκτρονίων στο δυναμικό Coulomb-Stark και δείχνει να επηρεάζεται ασθενώς από την ηλεκτρονιακή δομή του ατόμου-στόχου.

Τέλος, όσον αφορά τον τρίτο άξονα, εκμεταλλευόμενοι το περίπλοκο (σχέση με το μονοφωτονικό) διφωτονικό σχήμα διέγερσης έγινε ένας ενδελεχής έλεγχος των προβλέψεων του θεωρητικού μοντέλου. Στην περίπτωση τυχαίου προσανατολισμού του διανύσματος πόλωσης σε σχέση με τον άξονα του στατικού πεδίου οι εικόνες ΜΦ παρουσιάζουν περίπλοκη ακτινική κατανομή και φαινόμενα συμβολής λόγω της ταυτόχρονης παρουσίας καταστάσεων με μαγνητικούς αριθμούς $|m|=0,1,2$. Αυτό το γεγονός και ειδικά η μη-τετριμμένη παρουσία του χαρακτήρα $|m|=1$ αποδεικνύεται και από την ανάλυση των πειραματικών φασμάτων. Με χρήση των βασικών στοιχείων πολυηλεκτρονιακών θεωριών και μιας σειράς πειραματικών φασμάτων, μπορούν να εξαχθούν τα αποσυντεθειμένα φάσματα μιας τιμής του κβαντικού αριθμού $|m|$. Παραδείγματος χάριν, οι φασματικές γραμμές του αποσυντεθειμένου φάσματος $|m|=1$ υποδηλώνουν συντονισμούς του συγκεκριμένου κβαντικού αριθμού των οποίων τα χαρακτηριστικά είναι εμφανή και στις αντίστοιχες εικόνες ΜΦ.

Η παραπάνω ανάλυση οδήγησε στην ανάπτυξη μεθοδολογίας η οποία μπορεί να χαρακτηρίσει στοιχεία της γεωμετρίας της διάταξης, όπως οι διευθύνσεις της διάδοσης της ακτινοβολίας laser σε σχέση με το στατικό ηλεκτρικό πεδίο και το διάνυσμα της πόλωσης σε σχέση με τον άξονα της ανίχνευσης (κάμερα). Ενδιαφέρον παρουσιάζει ακόμα, η σύγκριση με μελέτες που αφορούν στην τομογραφική ανακατασκευή των τρισδιάστατων τροχιακών. Στην περίπτωση της ΜΦ, υπάρχει συνεισφορά συνιστωσών διαφορετικού κβαντικού αριθμού $|m|$ οι οποίες μπορεί να περιέχουν ακόμα και συντονισμούς επαυξημένου αριθμού κόμβων της ακτινικής κατανομής. Επίσης, η περιστροφή του διανύσματος της πόλωσης μεταβάλει την συνεισφορά των διαφόρων συνιστωσών διαφορετικού $|m|$ και επακόλουθα το εξερχόμενο ρεύμα πιθανότητας μεταβάλλεται αναλόγως. Αντιθέτως στην τομογραφική ανακατασκευή η κατανομή ταχυτήτων των ηλεκτρονίων θεωρείται ως το αντικείμενο το οποίο περιστρέφεται μαζί με το διάνυσμα της πόλωσης και κατά τα άλλα παραμένει αναλλοίωτο.

Table of Contents

List of Abbreviations

Arb. units	Arbitrary units
ASE	Amplified Spontaneous Emission
Au	Atomic Units
Alu	Arbitrary Length Units
BBO	Barium Borate (BaB_2O_4)
DoS	Density of States
E.g.	Exempli gratia (“for example”)
FSR	Free Spectral Range
I.e.	Id est (“in other words”)
Ip	Ionization potential
KDP	Potassium Dihydrogen Phosphate (KH_2PO_4)
LAIR	Laser-Atom Interaction Region
FTT	Frame Transformation Theory
MCP	Micro-Channel Plate
OGE	Optogalvanic Element
PAD	Photoelectron Angular Distribution
PM	Photoionization Microscopy
PSD	Position Sensitive Detector
SFIS	Static Field Induced States
SHG	Second Harmonic Generation
SP	Saddle Point
TDSE	Time Dependent Schrodinger Equation
TS	Tunneling State
VMI	Velocity Map Imaging
VMIS	Velocity Map Imaging Spectrometer
Nd:YAG	Neodymium-doped yttrium aluminum garnet

Introduction

The quantum description of physical systems at the atomic scale is heavily based on the concept of the wave function, which is obtained by solving the Schrödinger equation. Traditionally, however, experimental information on the wave function is only inferred by comparing theoretically calculated and experimentally measured observables, such as absorption or emission spectra. The wave function itself is generally not measured directly, while it is quite evident that access to it would allow for much more insight into the structure of the quantum systems under study. This reasoning explains the considerable recent achievements towards the development of experimental approaches aiming to the observation of the wave function itself. On the one hand, microscopy techniques, such as Scanning Tunneling and Atomic Force microscopies (STM and AFM, respectively), were employed for the detection of photoemission from a single molecule deposited on a surface [1,2] and allowed for the reconstruction of its molecular orbitals [3]. In another approach, the interaction of atoms and small molecules with strong laser fields, in conjunction with imaging methods, permitted the tomographic reconstruction of the electron density of their ground states [4,5]. Furthermore, the application of weak measurements concepts [6,7] led to the complete (amplitude and phase) determination of the wave function of the photon [8].

The work of the present thesis concerns another imaging technique, so-called photoionization microscopy (PM), capable of experimentally observing the squared modulus of the wave function of an electron emitted from an atom. This is achieved by measuring the two-dimensional flux of slow (meV) electrons ejected during the photoionization of neutral atoms in the presence of a uniform static electric field. The term “microscopy” is justified by the fact that the wave function of the outgoing photoelectrons in the direction of the field extends over macroscopically large distances. Transversely to the field, however, the wave function is bound. The electron current probability density is imaged by a position sensitive detector (PSD) and the low energy of the liberated electrons allows for the observation of quantum interferences on the recorded images. In turn, it can be shown [9,10,11] that, indeed, these interference structures are directly related to the squared modulus of the electronic wave-function. Although the wave function’s phase cannot be measured, PM appears nowadays to be the only method where the

squared modulus of the wave function is directly projected on the surface of the detector without any requirements for further hypotheses or reconstruction processes.

The concept of PM was introduced during the early 1980s [9,12] and analyzed in detail over the whole decade by Kondratovitch and Ostrovsky [10,11] within the framework of the hydrogenic Stark effect, which was described semi-classically and in terms of so-called parabolic wave functions [13,14]. In fact, the role of the static electric field is not to just guide the free electrons towards the detector. On the one hand, experimental measurements [15] and predictions based on classical trajectory calculations for an electron in the combined Coulomb-Stark field [16] showed that slow photoelectron images present interesting features and striking differences with respect to high-electron-energy images. On the other hand, and perhaps more importantly, just above the field-induced ionization threshold and up to the zero-field threshold, the field presence leads to the coexistence of continuum and quasi-bound Stark states (resonances). PM may provide access to the wave function of one or the other, but its inventors where particularly interested for resonant wave function imaging. Nevertheless, the first partial experimental realization was achieved in studies dealing with photodetachment [17], the latter characterized by the presence of purely continuum states, but not resonances.

On the quest for resonant images, the first PM experiments were performed with xenon atoms [18,19,20]. Remarkably, in these experiments, the number and position of nodes of the recorded wave function evolved smoothly with photon energy, and remained to a large extent insensitive to the presence of resonances. These observations were explained by the fact that non-hydrogenic atoms are characterized by the emergence of short-range interactions induced by the penetration of the excited electron's wave-function into the residual ionic core. As a consequence, their Stark states are expressed as mixtures of hydrogenic quasi-bound and continuum parabolic states. Then, a significant portion of an initially prepared resonant state population spreads out over several degenerate continua (i.e. a form of autoionization), while resonant and continuum excitation amplitudes out of a given initial state become comparable. Thus, the image resonant features may be rather weak and hard to observe and these difficulties grow with increasing ionic core size. Hence, the absence of resonant effects in Xe (atomic number Z=54) may be explained by the large ionic core size.

As a next step towards the search of resonant signatures, experiments on the light Li (Z=3) [21,22] and He (Z=2) [23] atoms, as well as on Hydrogen atom [24] itself were performed almost

during the same period. The Hydrogen experiment fully verified the first 30-year old predictions [10,11], as well as very recent ones [25,26,27]. The resonant signatures were also clearly observed in the Li experiment, despite the fact that they were found to be fairly weaker than the hydrogenic ones. As for the He experiment, resonant manifestations were found to be almost equally intense with the hydrogenic, because the recording were performed near avoided crossings between pairs of interacting resonances [28], with the resonance of interest being effectively decoupled from the continua. The observations of the above experiments on light non-hydrogenic atoms were fully compatible with accompanying theoretical predictions [22,23,29]. In fact, some theoretical work was devoted even to Xe itself [30], and predicted that under favorable conditions (spatial resolution spectral resolution excitation laser line-width, proper choice of field strength, etc.) it would be possible to record resonant images even for this heavy atom. Other theoretical work on non-hydrogenic atoms concerned the Alkali metal atoms such as Na [31,32]. One of the interesting predictions in that work is that the dominance of resonances on PM images depends nontrivially on and varies with the field strength [33], which then should be chosen carefully.

Remarkably, quite recent experimental and theoretical work on either hydrogen or more complex atoms [34,35,36,37] implied that the scope of PM is not limited to the recording of resonant images. Instead, it was also demonstrated that the evolution of images and corresponding radial distributions as a function of energy may be related to the dynamics characterizing the Coulomb-Stark problem. Particularly, the main quantity of interest here is the time delay between the arrivals on the detector, when selected pairs of electron trajectories are considered. Despite the fact that the typical time scales of the Stark effect fall within the picosecond range [38], this kind of information, as well as the methods that may be used to extracted it, is central in the frontier atto-physics science [39,40]. The recent proposals deal with the encoding of time-delays into phase differences associated with the aforementioned trajectory pairs, and the extraction of these phase differences from the energy dependence of the radial distributions. Additionally, it appears that the positive energy range is the best suited for such studies, while the presence of resonances would complicate the analysis. Nevertheless, this picture did not always provide meaningful results and left some unanswered questions. Particularly, it was not known if this picture is global enough to be obtained by performing relevant experiments in non-hydrogenic atoms, or it is strictly restricted to the hydrogenic case.

Last but not least, it is long ago known and proved experimentally that the presence of an electric field imposes a quantization axis, i.e. a preferable direction in space [41,42]. This seems to be particularly true when meV electrons are involved. On the other hand, imaging spectrometers make use of an electric field to guide the ionized electrons to the detector. When, however, electrons of fairly high energy are involved, the analysis of photoelectron angular distributions (PADs) is based on the assumption that they are built with respect to the linear laser polarization vector (see for example [43,44,45,46]). In other words, it is accepted that the polarization vector is the quantization axis and the possible implication of the static extraction field is ignored. It is, furthermore, assumed that rotation of the polarization vector will rotate the whole PAD, which will remain otherwise unaffected. This is reminiscent of the recording of PADs with electron spectrometers other than the imaging ones and where electric fields in the laser/atoms intersection point are practically absent [47]. The above postulations allowed the tomographic reconstruction of the 3D PADs from the 2D images on the PSD [48,49]. Nevertheless, many questions on the limits of applicability of such tomographic methods remained open.

Motivated by the above discussion, the purpose of the present work is to provide a number of answers into the following three directions:

(i) Evidently, the fact that resonant images were recorded so far solely in small complex atoms poses some limits on the usefulness of PM. Is it possible to record resonant images in non-hydrogenic atoms considerably heavier than Li and without applying any particular strategy (such as recordings near avoided crossings, etc.)?

(ii) How do non-resonant images and radial distributions evolve with energy in a non-hydrogenic atom, what are the common characteristics with the hydrogenic data and what can be learned or extracted from such data?

and

(iii) What can be learned from the rotation of the linear laser polarization vector with respect to the static electric field? Particularly, what are the challenges that tomographic PAD reconstruction techniques face when slow photoelectrons are involved?

In order to deal with the above directions, the present work is devoted to the photoionization microscopy of the magnesium atom via a two-photon excitation scheme out of its

ground state [Ne]$3s^2$. The singly and highly excited [Ne]3s*nk* configurations of Mg are composed by an outer electron in an $|nk\rangle$ Stark state with principal quantum number $n\approx30$, outside of a [Ne]3s Mg^+ ionic core which is open but spherically symmetric. Thus, in a first approximation the magnesium atom resembles the Alkali atoms (which possess a valence electron outside closed spherically symmetric subshells). Additionally, due to its middle size (Z=12) it stands between the two limiting cases of He (Z=2)/Li(Z=3) and Xe (Z=54).

Our experimental study is supported by a robust and efficient resolution method of the quantum hydrogenic Coulomb-Stark problem, where Schrödinger equation is separated in semi-parabolic coordinates. This coordinate system appears to be quite advantageous, easily dealing with the wave function's macroscopic extension as well as its peculiarities at small distances. Depending on the question at hand, these results are occasionally accompanied with the insightful predictions of a classical [16,34,50] and semi-classical [11,18,34,51] formulation that are presented here in a simple and dense format. In fact, in the course of this work it was also found insightful to connect the classical description of slow photoelectron imaging with notions borrowed from classical scattering theory [52]. Finally, quantum and semi-classical descriptions provide a global PM theoretical framework that will be used to decode our experimental PM results.

Briefly commenting on the achieved goals, we mention first that we made use of the well-established information [21,22], that the resonant character of the recorded images is more prominent in the energy range just above the ionization threshold, where the number of continua is small. In fact, in order to avoid any misinterpretations, the characteristics of the continuum images were additionally studied in more detail than before within this energy range. As a result, we have indeed recorded a number of resonant manifestations in Mg atom.

Second, the experimental exploration of the specificities of the differential (radial and angular distribution) as well as of the total photoionization cross-sections in a wide energy range, revealed new phenomena that were known up to now mainly at a theoretical level [15,34,53]. We particularly focused on the structure of the electron's momentum distribution transversely to the field and as a function of energy. These 2D-maps offer a complete landscape of the relevant quantum interference effects whose gross features remain unnoticed on single images. A qualitative comparison between experimental magnesium and calculated hydrogenic observables corresponding to different initial states and excitation schemes helped identifying the features of

"universal" nature while, highlighted the possible differences. Moreover, these momentum distribution maps where employed for extracting information on electron dynamics. More specifically, we focused on the critical effect of glory scattering, i.e. the signal at the center of the photoelectron momentum distribution, which is a dominant feature of the images when the laser polarization vector is parallel to the static electric field vector. It will be shown that indeed, while this observable is easy to record and analyze, it incorporates important information about the electron dynamics in the Coulomb-Stark potential.

Finally, we have experimentally (in Mg) and theoretically (in H) demonstrated the simultaneous excitation of different m (azimuthal quantum number) final states, after two-photon excitation from an m=0 ground state. It is proved that the rotation of the linear ionizing-laser-beam polarization with respect to the electric field direction gives rise to m-beating effects, due to the coherent contributions of multiple-m states in the outgoing electron flux. In fact, our set-up and experiment are similar to those employed in tomographic techniques, but the presence of the static electric field in addition to the Coulomb attraction is shown to pose new challenges for tomographic reconstruction techniques involving slow (meV) electrons.

Chapter 1: Theoretical Framework of Photoionization Microscopy

1.1 Classical and Semi-Classical Treatment of the Hydrogenic Stark Effect

Many important aspects of the simultaneous interaction of slow electrons with a Coulomb field and with a homogeneous static electric field are of classical origin. The following section is devoted to the description of these aspects and their manifestation on the recorded images. Special attention is paid to the description of basic concepts and definitions along with important connections to classical scattering theory. The mathematical tools necessary for calculating the main classical features of a Photoionization Microscopy (PM) image are also presented here. Finally, this section ends with a brief semi-classical treatment of quantum interference effects that will allow a more comfortable connection with the fully quantum mechanical framework presented in the next section.

1.1.1 Classical Description

Let a negatively charged particle (electron) move under the influence of both, a homogenous static electric field directed along the positive z axis and an attractive Coulombic center located at the origin. The relevant combined potential is presented in Figure 1 and is written in atomic units (a.u., $\hbar=m_e=e=(4\pi\epsilon_o)^{-1}=1$) as:

$$V = -\frac{Z}{r} + Fz \tag{1}$$

where F is the strength of the uniform field, Z is equal to the charge of a structureless ion (Z=1 for the hydrogen atom) and $r = (x^2+ y^2+ z^2)^{1/2}$. Two characteristic energies are marked on the z-(x,y) potential surface of Figure 1 namely, the zero-field ionization threshold in the absence of the static

field (F=0) which is set at energy E=0 and the field-induced ionization limit i.e. the classical saddle point energy which is written as:

$$E_{sp}^{cl} = -2(ZF)^{1/2} \quad (2)$$

or $E_{sp}^{cl}[\mathrm{cm}^{-1}] \approx -6.1212 \times \sqrt{F[\mathrm{V/cm}]}$ in spectroscopic units.

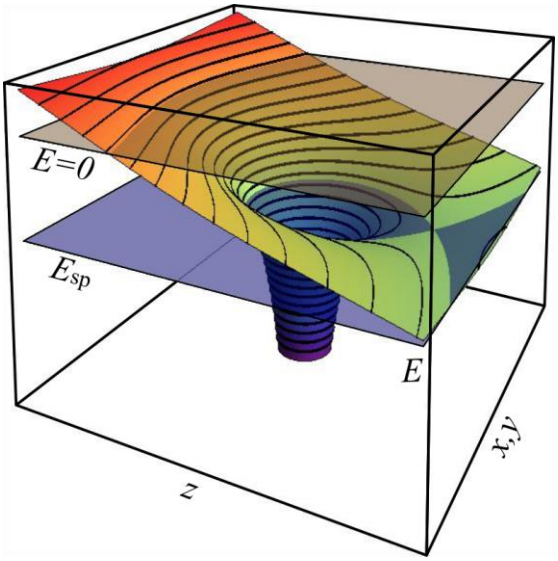

Figure 1. Schematic representation of the combined Coulomb and Stark field potential energy in Cartesian coordinates. Equipotential curves (black lines) exhibit open bottleneck-like shape. The saddle point energy E_{sp} is a function of the uniform static field strength. Classically, for $E > E_{sp}$ the electron can escape the Coulomb well. The unique shape of the potential leads to complicated classical trajectories.

Interestingly, the electron motion in this potential is equivalent to the motion of a celestial object orbiting a mass center (e.g. Earth) while a constant force is acted upon it (e.g. solar pressure or constant thrust) [54,55]. Due to the axial symmetry of the potential the general three-dimensional classical motion is separable in either the semi-parabolic coordinate system (χ,υ,φ) [41,51,55] defined by,

$$\chi = \sqrt{r+z} \geq 0$$
$$\upsilon = \sqrt{r-z} \geq 0 \quad (3)$$
$$\varphi = \tan^{-1}(y/x)$$

or the parabolic coordinate system ($\xi=\chi^2,\eta=\upsilon^2,\varphi$) [10,11,16,41] or even the mixed parabolic system (χ,η,φ). For the sake of consistency between classical and the quantum formulation to be discussed later on, semi-parabolic coordinates are used throughout this thesis and we also provide here the inverse relations

$$\begin{aligned} x &= \chi\upsilon\cos(\varphi) \\ y &= \chi\upsilon\sin(\varphi) \\ z &= (\chi^2-\upsilon^2)/2 \end{aligned} \tag{4}$$

while $r=(\chi^2+\upsilon^2)/2$. The angle φ is the azimuthal angle measured from the x axis. Following the coordinate system transformation of Eq. (3), the Hamiltonian is written as [55]:

$$H=\frac{1}{2}\left[\frac{({p_\chi}^2+{p_\upsilon}^2)}{2\,(\chi^2+\upsilon^2)}+\frac{{p_\varphi}^2}{\chi^2\upsilon^2}\right]-\frac{2Z}{\chi^2+\upsilon^2}+F\frac{(\chi^2-\upsilon^2)}{2}=E \tag{5}$$

where the quantities (p_χ, p_υ, p_φ) are reduced generalized momenta, related to the ordinary momenta ($dq_i/dt=\dot{q}_i$) as follows:

$$\begin{aligned} p_\chi &= \frac{\mathrm{d}t}{\mathrm{d}\tau_1}\dot{\chi}=(\chi^2+\upsilon^2)\dot{\chi} \\ p_\upsilon &= \frac{\mathrm{d}t}{\mathrm{d}\tau_1}\dot{\upsilon}=(\chi^2+\upsilon^2)\dot{\upsilon} \\ p_\varphi &= \frac{\mathrm{d}t}{\mathrm{d}\tau_2}\dot{\varphi}=\chi^2\upsilon^2\dot{\varphi} \end{aligned} \tag{6}$$

These generalized momenta involve two reduced "time" variables (τ_1,τ_2), which connect the physical time t with the spatial coordinates χ,υ:

$$\begin{aligned} d\tau_1 &= \frac{dt}{\chi^2+\upsilon^2}=\frac{dt}{2r} \\ d\tau_2 &= \frac{\mathrm{d}t}{\chi^2\upsilon^2} \end{aligned} \tag{7}$$

The azimuthal angular momentum is not present in the Hamiltonian of Eq. (5), while the azimuthal momentum p_φ is conserved [10,16,55]. This is related to the quantum number $m(=p_\varphi)$ being a "good" quantum number [14] discussed in section 1.2.

After appropriate manipulations, the Hamiltonian (5) can be separated into the following three uncoupled equations describing the electron motion:

$$\frac{p_\chi^2}{2} + U_\chi^{cl} = 2\,Z_1 \quad , \quad U_\chi^{cl} = \frac{F}{2}\,\chi^4 - E\,\chi^2 + \frac{{p_\varphi}^2}{2\,\chi^2} \tag{8}$$

$$\frac{p_\upsilon^2}{2} + U_\upsilon^{cl} = 2\,Z_2 \quad , \quad U_\upsilon^{cl} = -\frac{F}{2}\,\upsilon^4 - E\,\upsilon^2 + \frac{{p_\varphi}^2}{2\,\upsilon^2} \tag{9}$$

$$p_\varphi = \frac{\varphi - \varphi_0}{\tau_2}\,. \tag{10}$$

The conservation of mechanical energy applies in the pseudo-form of "*K*"+"*V*" ="*E*", where "*K*"= $\frac{p_\chi^2}{2}$ or $\frac{p_\upsilon^2}{2}$, "*V*"= U_χ^{cl} or U_υ^{cl} and "*E*"= $2Z_1$ or $2Z_2$ for the χ and υ coordinates respectively. The two separation constants Z_1 and Z_2 are related through the relation [16]:

$$Z_1 + Z_2 = Z\,. \tag{11}$$

In what follows the discussion will be limited to the case of zero-azimuthal momentum p_φ=0. This condition leads to a planar electron motion restricted to a plane defined by the initial azimuthal angle φ_0 (see Eq.(10)) and allows for numerous simplifications; concerning particularly the initial electron launch conditions. As a result, one obtains fairly simple mathematical expressions that predict the majority of the classical features of a PM image. On the other hand, those features which are attributed to a non-zero momentum and are somehow connected to the present work are briefly commented at the end of this subsection.

Before proceeding further, it is convenient to define the reduced energy variable,

$$\varepsilon \equiv \frac{E}{2\sqrt{Z\,F}} = \frac{E}{|E_{sp}^{cl}|}\,. \tag{12}$$

with the help of which the solutions are more clearly expressed. As we already mentioned, the major consequence of the external static electric field is to lower the ionization limit by an amount equal to the saddle point energy. E_{sp}^{cl}, which separates the energy range into two regions: (i) the $E< E_{sp}^{cl}$ (ε<–1) one, where the electron is classically trapped and can never escape the attractive Coulomb center and (ii) the $E>E_{sp}^{cl}$ (ε>–1) one, where the electron is energetically allowed to escape (i.e. to ionize) towards infinity ($z\rightarrow-\infty$). Therefore, in photoionization studies we are primarily interested for the ε>–1 energy range. We assume next that the electron is initially at the axes origin and that it is "launched" with an angle β with respect to the positive *z* axis. Uphill or downhill ejection with respect to the field direction corresponds to β=0 or β=π, respectively.

This initial ejection angle β is connected to the separation constants of Eqs. (8,9) through the relations [10,16]:

$$\begin{aligned} Z_1 &= Z\cos^2\left(\frac{\beta}{2}\right) \\ Z_2 &= Z\sin^2\left(\frac{\beta}{2}\right) \end{aligned} \tag{13}$$

Within the $-1<\varepsilon<0$ energy range the motion may be bound or unbound according to a reduced-energy-dependent critical ejection angle $\beta_c = 2\sin^{-1}(|\varepsilon|)$ [16]. For $\beta<\beta_c$ the electron is trapped and does not ionize (although this is energetically possible), while for $\beta>\beta_c$ the electron escapes towards a detection plane perpendicular to the z-axis and placed at some large distance $z_{det}<0$. For positive energies β_c loses its meaning and the electron can reach the detector's plane for all launch angles β within the full $[0,\pi]$ range.

The classical trajectories can be calculated analytically [11,16,50,54,55]. Integration of Eqs. (8,9) for $p_\varphi=0$ provides the equation of motion for χ and υ as a function of the reduced time variable τ_1 (the derivation of the general $p_\varphi\neq0$ equations of motion and the arbitrary-initial-point ejection equations of motion can be found in Ref. [55]). Specifically, the motion along the χ potential is described by [55]

$$\chi(\mathbf{t}) = \chi_+\left|\mathrm{CN}\left[\mathrm{K}\left[m_\chi\right](2\mathbf{t}-1), m_\chi\right]\right|, \tag{14}$$

where CN is the Jacobi elliptic cosine function and K the complete elliptic integral of the first kind, while the elliptic modulus m_χ and the oscillation amplitude χ_+ are given by

$$\begin{aligned} m_\chi &= \frac{1}{2}\left[1+\frac{\varepsilon}{\left[\varepsilon^2+\cos^2\left[\frac{\beta}{2}\right]\right]^{\frac{1}{2}}}\right] \\ \chi_+ &= 2^{1/2}\left[\frac{Z}{F}\right]^{1/4}\left[\varepsilon+\left[\varepsilon^2+\cos^2\left[\frac{\beta}{2}\right]\right]^{\frac{1}{2}}\right]^{\frac{1}{2}} \end{aligned} \tag{15}$$

As it turns out from Eq. (14) the function $\chi(\mathbf{t})$ is always bound and periodic with a period of $2T_\chi$ where

$$T_\chi = \frac{\mathrm{K}[m_\chi]}{(F\,Z)^{1/4}\left(\varepsilon^2+\cos^2\left[\frac{\beta}{2}\right]\right)^{\frac{1}{4}}} \tag{16}$$

In fact, the reduced time **t** above is measured in half-period T_χ units, i.e. $\mathbf{t}\equiv\tau_1/T_\chi$ (note in passing that for p_φ=0 the reduced time $d\tau_2$ is irrelevant and does not enter to the problem).

As for the υ-equations of motion for $\beta>\beta_c$, there are two classes of solutions. Assuming that the electron transfer from υ=0 up to $\upsilon\to\infty$ ($z\to$-∞) is achieved within a reduced time $\tau_1=T_\upsilon$, the first type of solution is

a) the so-called Type I solution,

$$\upsilon(\mathbf{t}) = \upsilon_+ \left| \frac{C - \mathrm{SC}\left[\mathrm{F}\left[\tan^{-1}[C], m_\upsilon\right]\left(1-\frac{2\mathbf{t}}{\mathcal{R}}\right), m_\upsilon\right]}{C + \mathrm{SC}\left[\mathrm{F}\left[\tan^{-1}[C], m_\upsilon\right]\left(1-\frac{2\mathbf{t}}{\mathcal{R}}\right), m_\upsilon\right]} \right| \text{, holding for } \sin\left(\frac{\beta}{2}\right) > |\varepsilon| \text{ and } \varepsilon>-1 \qquad (17)$$

where SC is the Jacobi elliptic tangent function and F the incomplete elliptic integral of the first kind. The elliptic modulus m_υ, the oscillation amplitude υ_+ and the parameter C are given by,

$$\begin{aligned} m_\upsilon &= 1 - \frac{1}{C^4} \\ \upsilon_+ &= 2^{1/2}\left[\frac{Z}{F}\right]^{1/4}\left[\sin\left[\frac{\beta}{2}\right]\right]^{1/2} \\ C &= \left[\frac{2\sin\left[\frac{\beta}{2}\right]}{\sin\left[\frac{\beta}{2}\right]-\varepsilon}\right]^{1/2} \end{aligned} \qquad (18)$$

while the dimensionless ratio

$$\mathcal{R} \equiv \frac{T\upsilon}{T\chi} \qquad (19)$$

counts the number of oscillations in the χ coordinate until the electron reaches infinity in the υ direction. Note that, this quantity is closely connected to the quantity "$N^{+/-}$" originally introduced in Refs. [11,19]. The second type of solution is

b) the so-called Type II one,

$$\upsilon(\mathbf{t}) = \upsilon_+ \left| \mathrm{SC}\left[\mathrm{K}[m_\upsilon]\frac{\mathbf{t}}{\mathcal{R}}, m_\upsilon\right] \right| \text{, holding for } \sin\left(\frac{\beta}{2}\right) < \varepsilon \text{ and } \varepsilon>0 \qquad (20)$$

where now,

$$m_{\upsilon} = 1 - \left(\frac{\varepsilon - \left(\varepsilon^2 - \sin^2\left[\frac{\beta}{2}\right]\right)^{\frac{1}{2}}}{\varepsilon + \left(\varepsilon^2 - \sin^2\left[\frac{\beta}{2}\right]\right)^{\frac{1}{2}}} \right)$$
$$\upsilon_+ = 2^{1/2}\left(\frac{Z}{F}\right)^{1/4}\left[\varepsilon - \left(\varepsilon^2 - \sin^2\left[\frac{\beta}{2}\right]\right)^{\frac{1}{2}}\right]^{\frac{1}{2}}. \quad (21)$$

Note that 0<**t**<$\mathcal{R}$. Finally, the ratio $\mathcal{R}$ is equal to,

$$\mathcal{R}_{\mathrm{I}} = 2\frac{\left[\varepsilon^2 + \cos^2\left[\frac{\beta}{2}\right]\right]^{\frac{1}{4}}}{\left[2\sin\left[\frac{\beta}{2}\right]\right]^{1/2} + \left[\sin\left[\frac{\beta}{2}\right] - \varepsilon\right]^{1/2}} \frac{\left|\mathrm{F}\left[\tan^{-1}[C], m_{\upsilon}\right]\right|}{\mathrm{K}[m_{\chi}]}$$
$$\mathcal{R}_{\mathrm{II}} = \frac{\left[\varepsilon^2 + \cos^2\left[\frac{\beta}{2}\right]\right]^{\frac{1}{4}}}{2^{1/2}\left[\varepsilon + \left(\varepsilon^2 - \sin^2\left[\frac{\beta}{2}\right]\right)^{\frac{1}{2}}\right]^{\frac{1}{2}}} \frac{\mathrm{K}[m_{\upsilon}]}{\mathrm{K}[m_{\chi}]} \quad (22)$$

for the Type I and Type II solution, respectively.

The analysis of the above equations shows that for the examined planar motion, the form of the trajectories depends on the physical time *t* only through the reduced time τ_1 or alternatively through **t**. On the other hand, the actual time of flight is of importance for a number of studies and it should then be explicitly computed. This is achieved by introducing the equations of motion in Eq. (7) that relates the reduced and physical time and then integrating either numerically or analytically this so-called Stark equation [55], i.e.

$$t = \int_0^{\tau_1} \{\chi^2(\tau_1') + \upsilon^2(\tau_1')\} d\tau_1' \quad (23)$$

Figure 2(a) shows the effective potentials U_{χ}^{cl}, U_{υ}^{cl} (see Eqs. (8,9) and the discussion therein) for some selected ε, F, β values. The pseudo-energy values $2Z_1$, $2Z_2$ determine the range of motion i.e. from the origin to their crossing point with the effective potentials. In addition, Figure 2(b) shows the semi-parabolic equations of motion for β=61 >β_c=60 degrees.

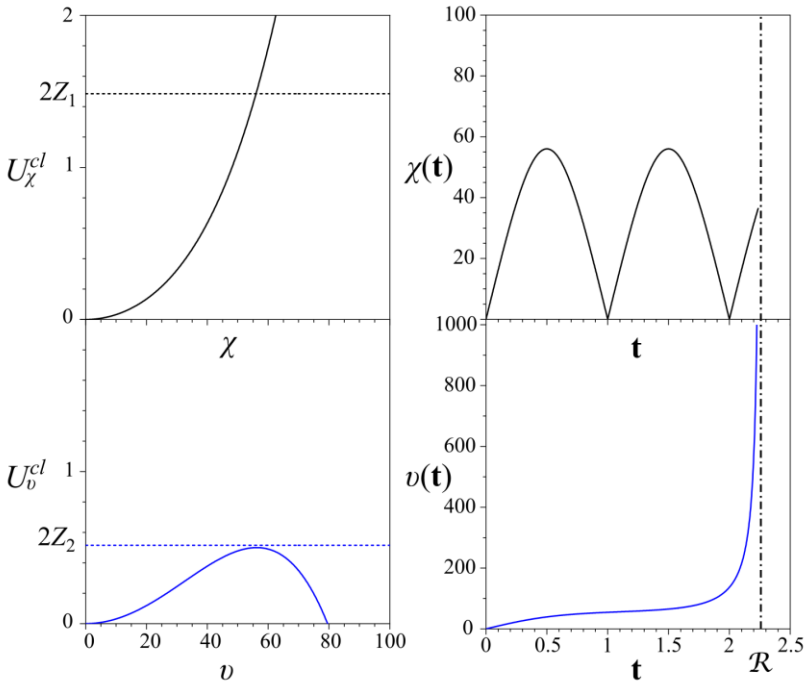

Figure 2. Calculated potentials, $2Z_1$, $2Z_2$ values and equations of motion for Z=1, ε=–0.5, F=10^{-7} a.u. and β=61 degrees (β_c=60 degrees). For these parameters $\mathcal{R}$≈2.259. Atomic units are used for all quantities. (a) Potentials in the, χ coordinate (black solid line) and υ coordinate (blue solid line) determine the bound and the unbound nature of the χ and υ motion respectively. $2Z_1$ (black short dashed line) and $2Z_2$ (blue short dashed line) are also shown. For $\beta<\beta_c$, $2Z_2$ lies below the potential maximum and the motion becomes bound in both directions. (b) Motion equations χ(**t**) (black solid line) and υ(**t**) (blue solid line). The χ(**t**) function performs $\mathcal{R}$ oscillations until υ(**t**) reaches infinity.

Since the semi-parabolic coordinate system is not particularly useful for visual inspection, Figure 3 presents a selection of trajectories for different ejection angles β but fixed ε and F. All presented trajectories are parallel to each other at large distances. In other words, for $\upsilon_{det} \to \infty$ they cross at the point $\rho=\chi_{det}\cdot\upsilon_{det}$ with χ_{det}=10.

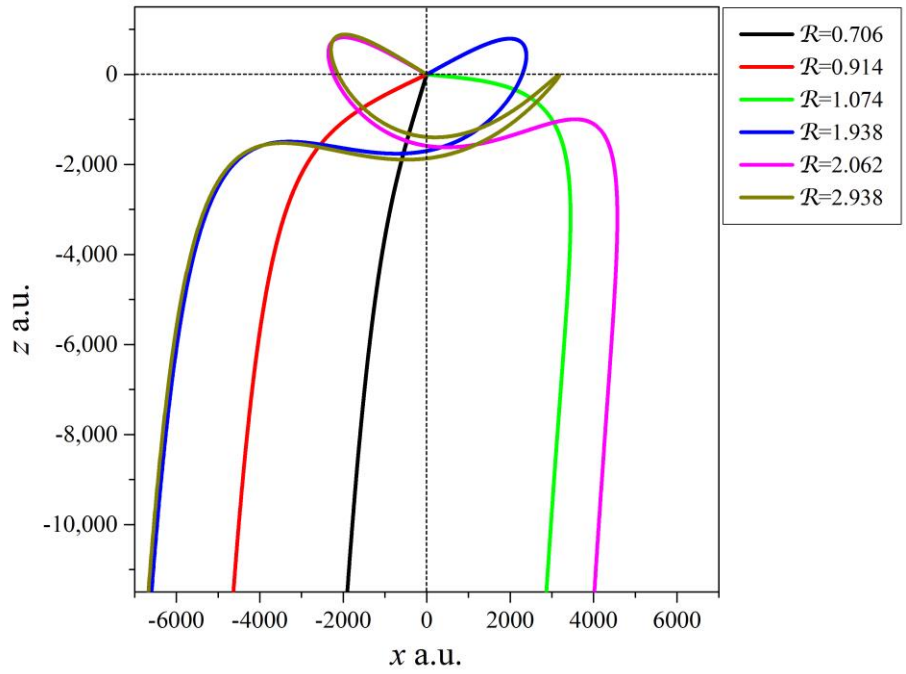

Figure 3. Calculated trajectories relevant to photoionization with ε=–0.5 and F=10^{-7}. The plane of motion is the *x*,*z* plane. The selected ejection angles are $\beta\approx$: 161.6 (black line), 113.7 (red line), 94.8 (green line), 62.8 (blue line), 61.9 (purple line), 61.1 (dark yellow line). In the particular example of the figure, the detector distance is set to infinity and asymptotically these trajectories approach the limit $\rho\rightarrow 10\cdot\upsilon_{\text{det}}$. Note that trajectories of $\mathcal{R}$<1 never cross the *z* axis while for $\mathcal{R}$>1 they cross one, two, three etc. with the *z* axis.

It is interesting to note that a value of the ratio $\mathcal{R}$ equal to 1,2,3 etc. implies that by the time the electron reaches infinity in the υ direction, it crosses the *z*-axis (i.e. returns to the axis origin in the χ direction) one, two, three etc. times. Even more, the ratio $\mathcal{R}$ may be employed for classifying the trajectories and we may, in fact, distinguish first between two major classes [11,16]:

(a) The *direct* trajectories ($\mathcal{R}$<1), (see black and red lines of Figure 3), which never intersect with the *z* axis and are almost parabolic. The existence of direct trajectories is possible only above a critical energy $\varepsilon_{\text{dir}}\approx$–0.755 [16,19,50] and

(b) Those trajectories that intersect at least once with the *z* axis ($\mathcal{R}$>1), hereafter called *indirect* trajectories (see green, blue, purple and dark yellow lines of Figure 3). The electron in this case is re-scattered by the attractive core once or multiple times before it finally escapes to infinity.

In general, many trajectories can reach a given point on the detector. They may be further classified in pairs, the first direct pair corresponds to $\mathcal{R}$ values within the range (0,1) (for energies above ε_{dir}), the second within the range (1,2), etc. Trajectories exhibit M_{tp} turning points in the χ coordinate, where,

$$M_{tp} = \frac{2N+1-(-1)^N}{4} \quad \text{with} \quad N \equiv \text{Integer Quotient}\,[\mathcal{R}/0.5] \tag{24}$$

The above classification is related to the one proposed in [11]. Note that $\mathcal{R}$ refers to electron paths reaching infinity, while for calculations performed for a detector placed at some finite distance, it should be redefined accordingly.

The motion of an electron in the Stark-plus-Coulomb potential is relevant to the case of photoionization while, in the absence of the Coulombic attraction the motion is relevant to photodetachment [17,52,56]. In the latter case a negative ion interacts with a light field in the presence of a homogenous static electric field. The outer electron is ejected with a kinetic energy equal to the photon energy minus the electron affinity and it moves under the influence of the static electric field. Then influence of the neutral atomic core can, to a first approximation, be neglected (this is simulated by setting Z=0 to the Hamiltonian of Eq. (5)). It follows that the electron trajectory is purely parabolic and is identical to the free fall of an object in a gravitational field [52]. Theoretical and experimental studies on photodetachment microscopy are closely related to the work of the present study, since for ε>>1 PM trajectories do not deviate significantly from their photodetachment counterparts [16,52]. On the other hand, for ε<1 the PM trajectories depend strongly on β and are found to be quite complex due to the influence of the Coulomb field.

1.1.2 Connection with the Classical Scattering Theory

The photoionization “experiment” described above can be considered as a half-collision process between a particle of mass m (electron) and a scattering center (residual ion) with no incident particle flux. The previously presented equations of motion can be used to calculate the classically predicted differential cross section of this scattering problem i.e. the spatially resolved electron impact distribution on a detector.

Here we deal with the two-dimensional motion case (p_φ=0) for electrons classically allowed to reach arbitrary large distances ($\beta>\beta_c$) and detectors placed at *finite distances* ~10^3 a.u. For practical convenience, the detector ($z=z_{det}<0$) can be replaced by a paraboloid surface of constant $\upsilon = \upsilon_{det} = \sqrt{-2z_{det}}$. The surface of the paraboloid and the plane detector differ in the z direction by $\Delta z=-\rho^2/(4z_{det})$, where $\rho=\chi\upsilon_{det}$ is the distance between the point of impact and the detector center. For the typically used field (~ 1000 V/cm), detector choice and energy values of the present study, to an excellent approximation it holds that $\Delta z\approx 0$ [27].

The classical differential scattering cross section – or in our case, equivalently, the radial distribution $R(\rho)$ – is defined as [50]:

$$R(\rho) \equiv \frac{d\sigma}{dA}(\rho) = \sum_i \frac{\sin\beta_i}{\rho}\left|\frac{d\rho}{d\beta_i}\right|^{-1} \tag{25}$$

where dA is the elementary surface on the detector $dA=2\pi\rho d\rho$ and the summation runs over all ejection angles that reach the same impact point on the detector. Note that, this relation closely resembles the classical scattering differential cross section relation of a particle scattered by a central potential [52], $\frac{d\sigma}{d\Omega}(\theta) = \sum_i \frac{b_i}{\sin\theta}\left|\frac{d\theta}{db}\right|^{-1}$, where now the summation runs over the impact parameters b_i, that lead to the same scattering angle θ. Within this context, the deflection function $\Theta(b)$ incorporates all the short-range interactions governing the scattering process but is not experimentally accessible. It is connected, however, with the scattering angle through the relation, $\Theta+2\pi\kappa=\pm\theta$, with integer κ.

The above-mentioned resemblance implies that the problem is apparently reduced to the calculation of the impact point radius ρ as a function of the ejection angle β i.e. the generalized deflection function $\rho(\beta)$. Unfortunately, for the case of PM no analytical expression can be derived. Instead, $R(\rho)$ needs to be computed numerically. On the other hand, the photodetachment dynamics provide an analytical expression, $R(\rho)\propto\sin(\beta)$ [52,56].

In Figure 4 we present the deflection functions for a typical field value and different reduced energies. For the lower energy that lies below ε_{dir} (Figure 4(a)) the series of lobes are formed solely by indirect trajectories while the existence of a critical angle β_c which separates the bound from the unbound motion is clearly visible (dashed red line). For higher energies an additional lobe is formed by the direct paths. For ε=0 there are an infinite series of lobes whose width decreases as β tends to zero. Each lobe is related to an energy and field dependent maximum

radius labeled as ρ_I, ρ_{II},ρ_{III} …,etc. For extremely high energies (e.g. ε=10) the indirect contribution becomes insignificant and the deflection function gradually approaches the corresponding photodetachment function [52]. In Figure 4(b,c,d) the angle of the first zero crossing is labeled as β_o, effectively separating the direct from the indirect contributions. This angle is found by setting Eq. (22) equal to unity ($\mathcal{R}$=1) and solving for β.

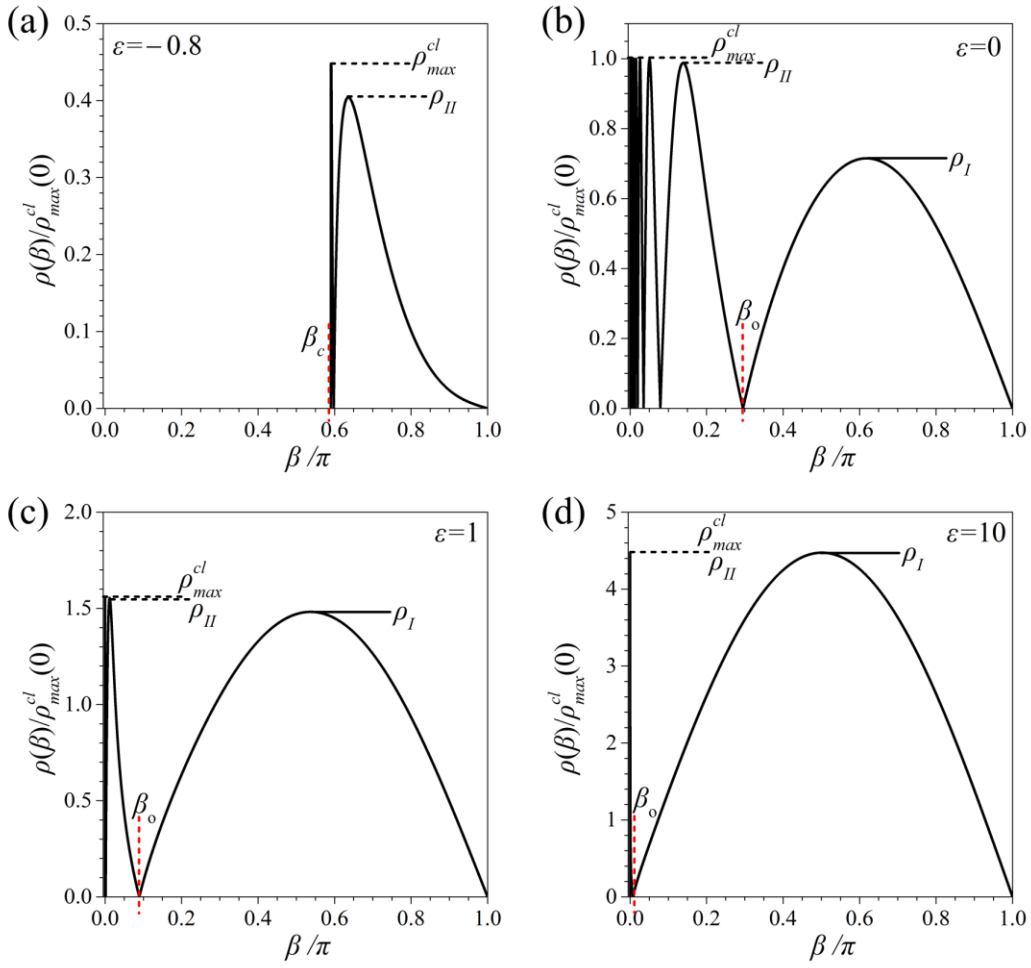

Figure 4. Photoionization deflection function in the case of photoionization for selected reduced energies ε. F=10^{-7} a.u. Vertical axis is scaled to the maximum classical radius for ε=0, $\rho_{max}^{cl}(0)$ (see Eq. (26)main text). (a) The direct contribution is absent for ε=–0.8 while no impact is recorded for β<β_c. (b,c) Direct trajectories form the lobe whose maximum radius is ρ_I (primary bow). Note that for positive energy β_c=0 and that ρ_{II}>ρ_I. Several zero radii crossings are also visible. (d) Strong resemblance to the photodetachment case where the indirect contribution is practically negligible.

As it is evident from Eq. (25) the classical cross section exhibits divergences when the generalized deflection function either becomes zero, $\rho(\beta)=0$, or it reaches an extremum. These types of divergences are named glory and rainbow scattering, respectively, after their light-scattering counterparts, encountered in atmospheric optics [57]. As is evident from Figure 4, the several zeros of $\rho(\beta)$ give rise to an intense peak at the center of the image i.e. the glory signal. It is important to realize that the glory signal is a feature that dominates the slow electron images (Figure 6) even at larger electron kinetic energies and may be misinterpreted as "zero" energy electrons in spectroscopy data recorded in velocity map imaging (VMI) setups [50]. As for the rainbows, the most intense is the one formed by the direct trajectories and appears at the ρ_I radius, hereafter called *direct bow*. Higher-order bows appear at ρ_{II} , ρ_{III}, … radii with progressively lower intensity. Practically, apart from the always visible primary bow, only ρ_{II} i.e. the *secondary bow*, can be resolved experimentally while higher order bows are extremely faint. All maximum radii are smaller or equal to the maximum radius of impact written as [11,16,52]:

$$\begin{aligned} \rho_{max}^{cl} &= 2\left[\frac{Z}{F}\right]^{1/4} |z_{det}|^{1/2}[\varepsilon+1]^{1/2},\ \varepsilon<0 \\ \rho_{max}^{cl} &= 2\left[\frac{Z}{F}\right]^{1/4} |z_{det}|^{1/2}\left[\varepsilon+[\varepsilon^2+1]^{1/2}\right]^{1/2},\ \varepsilon>0 \end{aligned} \tag{26}$$

The energy evolution of the bow scattering radii ρ_{max}^{cl}, ρ_I, and ρ_{II} as well as the detachment bow ρ_0 as a function of the reduced energy ε is shown in Figure 5. Note that for every ε it holds that $\rho_{max}^{cl} > \cdots > \rho_{II} > \rho_I > \rho_0$ and that practically all bows higher than the secondary bow (ρ_{II}) are indistinguishable from ρ_{max}^{cl}. Moreover, the direct bow manifests itself for $\varepsilon>\varepsilon_{\mathrm{dir}}$ and progressively approaches the maximum classical radius as ε increases. The photodetachment bow radius presents a similar behavior, having an energy onset at the zero-field ionization energy (ε=0).

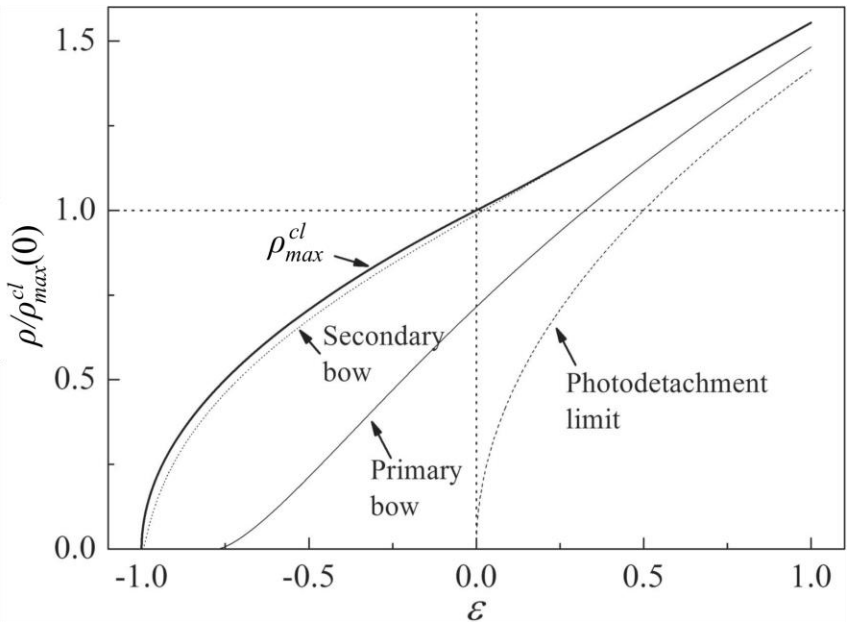

Figure 5. Classical bow maximum radii, in the cases of photoionization and photodetachment, as a function of the reduced energy ε. The classical maximum radius is also shown (bold solid line). Primary bow radius ρ_I start at the energy ε_{dir} and is denoted as a solid line. Secondary bow radius ρ_{II} is denoted as a dotted line. Photodetachment bow radius (short dashed line) starts at the zero-field ionization energy (ε=0). The radius axis is scaled to $\rho^{cl}_{max}(\varepsilon = 0)$. All radii progressively merge for increased energy.

As we already mentioned, the discussion is limited to p_φ=0, then the physical information observed in a photoelectron imaging experiment – or a PM experiment – is an angularly symmetric image with a radial distribution proportional to $R(\rho)$ (Eq. (25)) with respect to the detectors center.

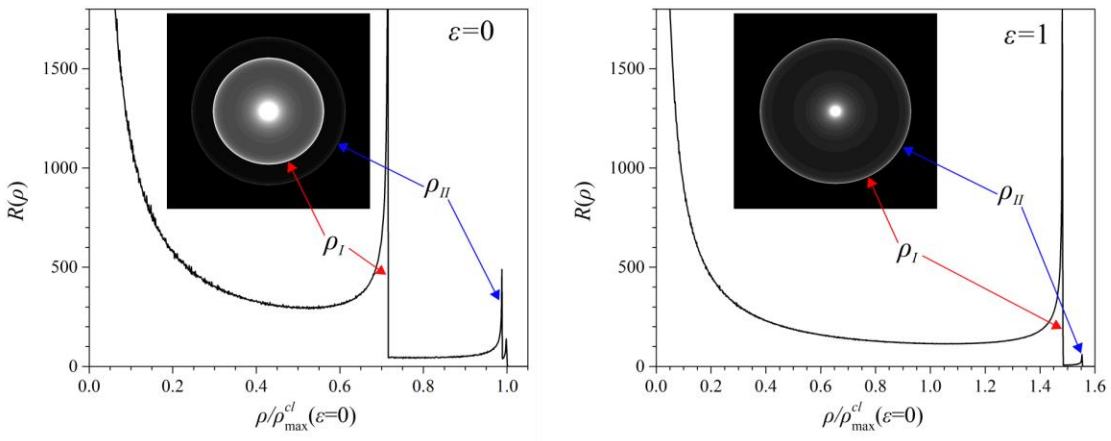

Figure 6. Radial distributions $R(\rho)$ and calculated images for ε=0 and ε=1. F=10^{-7} a.u. The calculations are performed by ejecting uniformly a large number of particles within the full β range $(0,\pi)$. Thus, the predicted divergences at the center of the image and at the classical bow radii, e.g. ρ_I, ρ_{II} are avoided.

Figure 6 presents two classically calculated slow photoelectron images for ε=0 and ε=1 along with their radial distributions. According to the classical model the indirect trajectories contribution spans the $0 \leq \rho \leq \rho_{II}$ range and form the secondary bow, visible as an outer bright ring. Furthermore, the radii of the direct trajectories extend over the $0 \leq \rho \leq \rho_I$ range and form the primary bow bright ring. We briefly remind that when the coulomb attraction can be safely ignored (extremely high energies), each ring of the VMI image (bow) of a given radius is associated with a photoelectron group of different energy, which is clearly not the case of PM. As for the glory signal, it is important to realize that it is a feature stemming from a critical scattering effect encountered in slow photoelectron imaging and it should not be confused with the simple maximum signal obtained with very high energy electrons in cases when the polarization vector is parallel to the field axis and perpendicular to the detector.

Let us finally make a brief discussion on the non-zero angular momentum case and present the form of the relevant trajectories and a number of predictions regarding the scattering observables. One of the major differences of the $p_\varphi \neq 0$ case is the manifestation of a different saddle point energy which, for Z=1, may be written as [58],

$$E^{\mathrm{cl}}_{\mathrm{sp},|p_\varphi|} \approx -2\sqrt{F}\left(1 - \frac{|p_\varphi|}{2}F^{\frac{1}{4}} - \frac{3}{32}p_\varphi^2\sqrt{F} + \cdots\right). \tag{27}$$

Moreover, the previous selection of initial conditions no longer applies because the axes origin lies now within the classically forbidden region due to the centripetal term of Eqs. (8,9). Thus, the electron is ejected near the coulomb center but not from the point χ=υ=0. The work of [59] tackles this problem by ejecting electrons radially from a sphere of some fixed radius. Despite the initial conditions selection, implications of major interest are extracted just by examining the form of the χ equation of motion. It turns out that for $p_\varphi \neq 0$, it holds that $\chi(\tau)>0$ for every β value, from which it is deduced that $\rho(\beta)>0$ and the electron never crosses the z axis. Indeed, due to the non-zero angular momentum the electron does not move in a fixed plane and always dodges the z axis. This fact has a major consequence, namely the disappearance of the glory scattering and its replacement by an additional bow (this time due to emerging minima in the deflection function). The latter bow,

could be termed as g-bow (glory-bow) and is a typical feature to images of non-zero p_φ motion. Calculations show that the g-bow radius approaches the center of the detector as the energy increases.

1.1.3 Semi-Classical Description

As seen in the previous discussion the classical description of an electron moving in the combined Coulomb plus a static homogenous electric field reproduces the gross features of a PM image (bow and glory scattering, radial distribution etc.). However, the particle dualism that leads to the formation of interference effect is completely ignored. This problem is tackled here, before the introduction of the fully quantum formulation. In the semi-classical picture, a moving particle along a trajectory accumulates a phase that is equal to the action integral along that trajectory [11,19,51]. Here, we account for the most important paths, that is, the classical trajectories. Then the manifestation of quantum effects in a PM image is interpreted as interferences among various classical trajectories that reach the same point on the detector. In semi-parabolic coordinates, the action is defined as [19]:

$$S_N = \int_0^{\upsilon_{det}} p_\upsilon d\upsilon + N \int_0^{\chi_{max}} p_\chi d\chi + \int_{\chi(N/2)}^{\chi_{det}} p_\chi d\chi \tag{28}$$

where N is defined in Eq. (24), $\chi(N/2)=0$ or χ_{max} for even or odd N values respectively, χ_{det}, υ_{det} are the impact point coordinates and $p_{\chi,\upsilon}$ the reduced generalized momenta (see Eqs. (8,9)).

The deflection functions of Figure 4 show that a large number of trajectories corresponding to different ejection angles β can reach the same point on the detector. Subsequently, these phases provide the contribution of the corresponding trajectories to the final electron wave function [19,51],

$$\Psi^{sc}(\rho) = \sum_i \frac{\sin\beta_i}{\rho} \left|\frac{d\rho}{d\beta_i}\right|^{-1} c_i e^{iS_i(\rho)} \tag{29}$$

where, as in Eq. (25), the summation runs over all ejection angles leading to the same PSD radius and the radial distribution is proportional to $|\Psi^{sc}|^2$. The most frequent choice of equal weights c_i is employed for the semi-classical calculation of Figure 7. Apart from the gross energy dependence which is common with its classical counterpart, the semi-classical curve is additionally

characterized by undulations of appreciable amplitude and intense beating effects. Despite the fact that the phases of each trajectory can be calculated analytically [11,16,50], Eq. (29) has no trivial solution. Detailed calculations of semi-classical PM images were previously presented in [19] and in the subsequent refined work of [51] which introduced the open orbit theory formulation for the PM case. For the purposes of this thesis we limit ourselves to the presentation of numerical calculations to be compared to quantum calculations and experimental results and then formulate approximate models in order to extract an intuitive explanation of the quantum modulations manifested in the scattering observables.

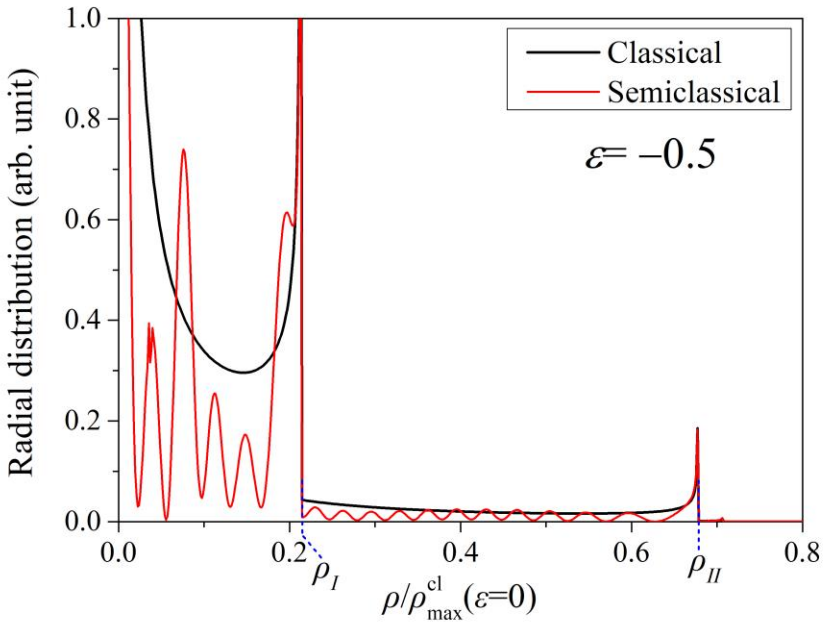

Figure 7. Classical (black line) and semi-classical radial distribution calculations. ε= –0.5 and F=1000 V/cm. Divergences are not treated for the purposes of this general presentation. The high "frequency" fringe system is called indirect fringe system and is visible in the $\rho_I < \rho < \rho_{II}$ radius range. The direct fringe system is located in the $0 < \rho < \rho_I$ radius range together with the beating effect. The later, can be viewed as the beating effect between the two fringe systems, arising from the simultaneous direct and indirect contribution.

Figure 7 presents the classical and semi-classical radial distribution calculations for the selected energy ε= –0.5>ε_{dir} and F=1000 V/cm. The divergences on the bow radii can be treated by the introduction of the Airy approximation [51]. The $\rho_I < \rho < \rho_{II}$ radius range can only be reached

by indirect trajectories and the radial distribution is dominated by a fringe system that reflects interferences solely amongst this type of trajectories. On the contrary, the $0 < \rho < \rho_I$ radius range is characterized by the contribution of both direct and indirect trajectories. Indeed, the strong modulation corresponds to the direct fringe system but the existence of indirect trajectories modulates the interferogram giving rise to a noticeable beating effect. This pattern is manifested in radial distribution maps $R(\varepsilon,\rho)$ as a checkerboard-like structure [27,34].

Let us now turn our attention to the positive energy range which is characterized by the so-called Static Field Induced States (SFIS), having no counterpart in the absence of the static electric field. These states may be modeled by a classical picture where the electron becomes "trapped" between the upfield direction (towards the positive *z* axis), which is dominated by the static field potential, and the coulombic center that acts as a hard wall [64]. Indeed, as classical calculations show, when the electron approaches the Coulomb center it is re-scattered in a highly elliptical orbit i.e. it is effectively reflected back to the upfield direction [64,60]. In other words, the Coulomb attractive center and the static field potential form a cavity in which the electron may be partially trapped [61].

The energy locations of SFIS were quantum-mechanically predicted for the hydrogen atom by [53,62,63]. They, however, can be accurately reproduced using a one-dimensional semi-classical model [64,65,66]. Specifically, one-dimensional motion is imposed by setting β=0 which implies Z_1=1 (see Eq. (11)). Then, in semi-parabolic coordinates the χ-coordinate motion is limited between χ=0 and $\chi=\chi_{\max}$ and the SFIS energy positions are predicted by the Bohr-Sommerfeld quantization condition,

$$2S'_{\chi}(\varepsilon) = 2k\pi + \pi \tag{30}$$

where k=0,1,2,…, and the action integral S'_{χ} is given by:

$$S'_{\chi}(\varepsilon) = \int_0^{\chi_{max}} p_{\chi}(\varepsilon; Z_1 = 1) d\chi \tag{31}$$

The above predictions of Eqs. (30) and (31) were verified by experimental atomic photoionization Stark spectra that, under certain conditions (polarization vector parallel to the electric field), revealed a series of positive energy broad resonances [42,64,67,68]. Note that the effect appears to be analogous to the quasi Landau levels observed in the presence of magnetic fields [14].

Interestingly, SFIS-like effects are also present for -1<ε<0 and are manifested in the Stark spectrum as broad intensity envelopes [68,69,70,71].

The semi-classical treatment is capable of formulating intuitive approximate models for the scattering observables e.g. the glory signal. The glory critical effect is a complex effect that originates from trajectories of finite weight ($\beta=\beta_o\{\mathcal{R}=1\}$, $\beta=\beta_1\{\mathcal{R}=2\}$, …) that contribute to an infinitesimally small volume ($\rho=0$). However, our calculations show that for $\varepsilon\geq1$ two trajectories contribute dominantly to the signal on the center of the detector, namely the trajectories with $\beta=\pi$ and $\beta=\beta_o$ (see the discussion of Figure 4). This allows for the formulation of a simple model of the glory signal that is presented here. In section 3.2.2, this model is compared to the experimental glory signal (for the magnesium atom) and shows a good agreement. The quasi-analytic relation giving the corresponding phase difference between the two paths (namely $\beta=\pi$ and $\beta=\beta_o$) is written as,

$$S_G=\begin{Bmatrix}\int_0^{\upsilon_{det}} p_\upsilon\big(Z_2=Z-Z_1(\beta_o)\big)d\upsilon+2\int_0^{\chi_{max}} p_\chi\big(Z_1=Z_1(\beta_o)\big)d\chi\\ +\frac{\pi}{4}-\int_0^{\upsilon_{det}} p_\upsilon(Z_2=Z)d\upsilon\end{Bmatrix} \tag{32}$$

and predicts the interference maxima of the glory signal ($S_G=2\pi k$, k=0,1,2,). This result, however, hides many more consequences. For example, phase and time of flight differences of the involved electrons trajectories are connected by following the results of [34] through the Eisenbud–Wigner definition of time delay [72]:

$$\Delta t=\frac{\partial S}{\partial E} \tag{33}$$

Then Eq. (32) allows for the calculation (in a continuous manner) of the time of flight difference between the two direct electron paths that impact the center of the detector. As a verification method, one can actually compute the classical paths and times of flight and subsequently calculate the time difference of these time of flights. Note that for ε~0 the time of flight differences between the other glory trajectories pairs $\beta=\beta_0$ and β_1, are almost equal to the aforementioned ones. Hence the above calculations call for a more complete study within the classical and the semi-classical framework in this ε~0 low energy range, where three or more trajectories may dominantly contribute to the glory signal.

1.2 Quantum Mechanical Treatment of the Hydrogenic Stark Effect

Here we summarize the Quantum mechanical theoretical framework of the Stark effect and subsequently the Photoionization Microscopy technique. Our development is based on the computationally more convenient semi-parabolic coordinate system. The properly normalized parabolic wave functions are introduced as solutions to the Coulomb-Stark Hamiltonian. Then, hydrogenic matrix elements are explicitly derived for the special cases of π or σ single photon excitation. However, the reader is not introduced to the general expression of the linear polarization transition operator (a subject of the forthcoming subchapter) for the sake of clarity. Electron current probability density is defined in the case of Photoionization Microscopy after the introduction of the used approximations. Finally, the non-hydrogenic case is briefly discussed by introducing the core strategies towards the multielectron PM description.

1.2.1 Hydrogenic Coulomb-Stark Wave Functions & Density of States

Let us now follow the work of [27] and formulate the quantum mechanical treatment of the Coulomb-Stark problem, which is the basis of the Photoionization Microscopy framework. As a first step our purpose is to examine the relevant hydrogenic wave functions and the so-called Density of States (DoS). Extending the earlier [13,14,63,73,74,75,76] as well as more recent studies [61,77,78] we present a purely numerical treatment which appears to be more efficient, practical and suitable for extending the formulation to non-hydrogenic systems. On the other hand, the analytical results of theoretical works [10,11,78] are truly insightful. By employing the Hamiltonian separability in semi-parabolic coordinates, we introduce the solution to the Coulomb-Stark problem similarly to [73,79] rather than the works that employed parabolic [10,11,13,53,62, 63,61,75,77,78,80] or mixed parabolic coordinates [25,26,74,76]. Moreover, the numerical techniques used are based on an array of robust variable-step integration methods that are both efficient and simple in their implementation. The description is kept brief for the quantities that were introduced in the previous subchapter.

The time independent Schrödinger equation describing the hydrogen atom in the presence of a homogenous and static electric field of strength $F>0$ and pointing towards the z direction is written as:

$$\left[-\frac{1}{2}\nabla^2 - \frac{Z}{r} + Fz - E\right]\psi(\boldsymbol{r}) = 0 \tag{34}$$

where r is the radial spherical coordinate, Z the nuclear charge and E the energy of the system. Atomic units are used throughout unless stated otherwise and spin orbit effects are not considered. The need to compute $\psi(\boldsymbol{r})$ at large (practically macroscopic) distances justifies the use of semi-parabolic coordinates, e.g. for a distance of $|z| \sim 10$ μm from the origin one needs to compute ψ up to $\upsilon \sim 6\times10^2$ a.u. Thus, time consuming calculations up to the parabolic coordinate $\eta = \upsilon^2 \sim 4\times10^5$ a.u. are avoided and, additionally, the numerical computational errors that are most frequently accompanying such extensive ranges are minimized.

The Laplacian is separable in semi-parabolic coordinates

$$\nabla^2 = \frac{1}{\chi^2+\upsilon^2}\left[\frac{1}{\chi}\frac{\partial}{\partial\chi}\left(\chi\frac{\partial}{\partial\chi}\right) + \frac{1}{\upsilon}\frac{\partial}{\partial\upsilon}\left(\upsilon\frac{\partial}{\partial\upsilon}\right)\right] + \frac{1}{\chi^2\upsilon^2}\frac{\partial^2}{\partial\varphi^2} \tag{35}$$

and the wave function writes

$$\psi(\boldsymbol{r}) = (2\pi\chi\upsilon)^{-1/2}\, X(\chi)Y(\upsilon)e^{im\varphi} \tag{36}$$

where m=0, ±1, ±2, …is the azimuthal quantum number analogous to p_φ introduced in the classical discussion. Notice that the states of different m are orthogonal, i.e. $\langle\psi; m|\psi'; m'\rangle \propto \delta_{m,m'}$.

By plugging Eq. (36) in the Schrödinger equation, Eq. (34), and after some manipulations, the following set of decoupled differential equations is obtained:

$$\left[-\frac{1}{2}\frac{d^2}{d\chi^2} + U_X^{eff}\right]X(\chi) = 2Z_1X(\chi) \quad , \quad U_X^{eff}(\chi) = +\frac{F}{2}\chi^4 - E\chi^2 + \frac{4m^2-1}{8\chi^2} \tag{37}$$

$$\left[-\frac{1}{2}\frac{d^2}{d\upsilon^2} + U_Y^{eff}\right]Y(\upsilon) = 2Z_2Y(\upsilon) \quad , \quad U_Y^{eff}(\upsilon) = -\frac{F}{2}\upsilon^4 - E\upsilon^2 + \frac{4m^2-1}{8\upsilon^2} \tag{38}$$

where the separation constants are related through Eq. (11), Z_1+Z_2=Z. The effective potentials U_X^{eff}, U_Y^{eff} differ only in the field strength sign. The separations constants (Z_1,Z_2) act as eigenvalues to the corresponding equations. The field strength, the azimuthal momentum value and the energy are predetermined and the equations are solved for fixed F, m and E values i.e. the problem is a scattering one.

For small χ values the $X(\chi)$ function writes [27]:

$$X_{\chi\to 0} \to A_X\, \chi^{|m|+\frac{1}{2}}\left(1+O(\chi^2)\right) \tag{39}$$

where A_X is an energy dependent normalization constant which is by definition positive. On the other, $\chi\to\infty$, extreme the form of U_X^{eff} enforces the bound electron motion along χ. The large-χ asymptotic form of $X(\chi)$ is written as [73],

$$X_{\chi\to\infty} \to \frac{1}{\chi}\exp\left[-\frac{F^{1/2}}{3}\chi^3+\frac{E}{F^{1/2}}\chi\right] \tag{40}$$

This asymptotic behavior ensures the quantization of the eigenvalue Z_1. Quantization provides a set of values of $Z_1^{n_1,|m|}$, with n_1=0,1,2,… being the number of nodes of $X_{n_1,|m|}(\chi)$. These wave functions are orthogonal to each other and normalized to unity according to:

$$\int_0^\infty X_{n_1,|m|}X_{n_1',|m|}d\chi = \delta_{n_1,n_1'} \tag{41}$$

Each given eigenvalue $Z_1^{n_1,|m|}$ also fixes the corresponding $Z_2^{n_1,|m|}=Z-Z_1^{n_1,|m|}$ one through Eq. (11).

The small-υ behavior of the $Y(\upsilon)$ is written similarly to the χ coordinate as:

$$Y_{\upsilon\to 0} \to A_Y\, \upsilon^{|m|+\frac{1}{2}}\left(1+O(\upsilon^2)\right) \tag{42}$$

where A_Y>0 is an energy dependent normalization constant. On the other hand, the $\upsilon\to\infty$ asymptotic form of $Y(\upsilon)$ may be written as,

$$Y_{\upsilon\to\infty} \to C_Y M(\upsilon)\sin[\theta(\upsilon)+\phi] \tag{43}$$

where M>0 is the so-called Milne function [81], ϕ a constant phase that depends on the lower integration limit υ_m [27] and θ_υ is a monotonically increasing phase:

$$\theta(\upsilon)=\int_{\upsilon_m}^{\upsilon}\frac{1}{M^2(\upsilon')}d\upsilon' \tag{44}$$

The constant $C_Y=\left[\frac{2}{\pi}\right]^{1/2}$ is obtained by energy normalizing the Y-wave function [13,14,25,63]. The description through the Milne function is suitable for highly oscillating wave functions. The problem is separated in the calculation of a varying phase introduced in the sine

argument and a smooth envelop which describes the wave function's maximum-minimum amplitude [81]. As a drawback one has to solve a nonlinear Milne equation:

$$M'' + k^2 M - \frac{1}{M^3} = 0 \tag{45}$$

where the squared wavenumber is obtained with the use of the effective potential and the eigenvalues of Eq. (38):

$$k^2 = 2\left[2Z_2 - \left\{-F\upsilon^4 - E\upsilon^2 + \frac{4m^2-1}{8\upsilon^2}\right\}\right] \tag{46}$$

Asymptotically the Milne function is practically equal to the WKB form,

$$M_{\upsilon\to\infty}(\upsilon) \approx \frac{1}{k^{1/2}(\upsilon)}\,. \tag{47}$$

and then

$$Y_{\upsilon\to\infty} \to \frac{C_Y}{k^{1/2}(\upsilon)} \sin\left[\int_{\upsilon_m}^{\upsilon} k(\upsilon')\,d\upsilon' + \phi\right]. \tag{48}$$

For these large-υ distances $k^2 \approx 2F\upsilon^4$ which is independent of the quantum number n_1. This reveals that, in our formulations the form of $Y_{\upsilon\to\infty}$ is fixed and acts as a starting point.

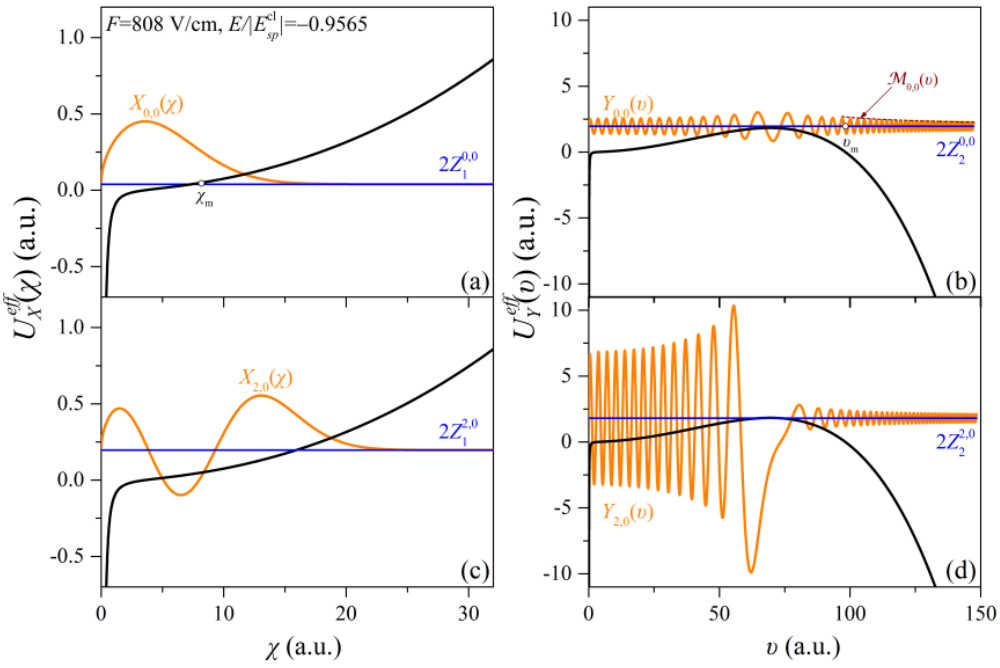

Figure 8. Semi-parabolic "effective potentials" $U_X^{eff}(\chi)$, $U_Y^{eff}(\upsilon)$ (black line) along the χ and υ coordinates respectively, together with $X_{n_1,|m|}$, $Y_{n_1,|m|}$ wave functions normalized as described in the text (orange lines). Also shown the $Z_1^{n_1,|m|}$, $Z_2^{n_1,|m|}$ eigenvalues (blue lines). F= 808 V/cm, ε= –0.9565 and m=0. For n_1=0 ((a),(b)), $Z_2^{0,0}$ is located above the potential barrier thus $Y_{0,0}$ is a continuum wave function. However, for n_1=2 ((c),(d)), $Z_2^{2,0}$ is located slightly below the potential barrier and $Y_{2,0}$ is a quasi-bound state with n_2=27. Note that the amplitude of $Y_{2,0}$ within the inner well is large, signifying a resonant state. A typical selection of matching points χ_m and υ_m is noted in (a) and (b) respectively, while the smooth Milne function is also drawn (brown dashed line).

Figure 8 shows the "effective potentials" in the χ, υ coordinates and the corresponding wave functions for two selected n_1 values. The reduced energy value, the field strength and the azimuthal quantum number values are fixed, i.e. ε=–0.9565, F=808 V/cm and m=0. The "eigenvalues" $2Z_1^{n_1,|m|}$, $2Z_2^{n_1,|m|}$are also shown. Note that the Y-wave function is a continuum function (see Figure 8 (b)) or a quasi-bound function (see Figure 8 (d)) according to the n_1 quantum number that characterizes this specific channel. In the latter case a third quantum number, namely n_2, can be defined as the number of Y-wave function nodes in the inner side of the potential barrier. In the case where the $Z_2^{n_1,|m|}$ value lies lower than the potential barrier (tunneling state) the electron is trapped and can only escape via the tunneling mechanism but the wave function amplitude may be almost zero or exhibit a large amplitude (resonance (n_1, n_2, m)). It is useful to remember that $2Z_1^{n_1,|m|} < 2Z_1^{n_1+1,|m|}$ and that $Z_2^{n_1,|m|}$ eigenvalues follow the reverse order $2Z_2^{n_1,|m|} > 2Z_2^{n_1+1,|m|}$. That leads to the conclusion that despite the fact that the $Z_1^{n_1,|m|}$ set is infinite, some of the $2Z_2^{n_1,|m|}$ become arbitrarily negative thus the Y-wave function is located well below the effective potential maximum (see Figure 8 (b, d)). These states are practically bound and irrelevant to photoionization.

The Density of States (DoS) is defined by the probability of finding the electron near the nucleus (axes origin). This probability is written with the help of the asymptotic forms of Eqs. (39,42) [63,76],

$$\mathrm{DoS}_{n_1,|m|}(F,E) = \frac{\left[X_{\chi\to 0}\right]^2 \left[Y_{\upsilon\to 0}\right]^2}{\chi^{2|m|+1}\,\upsilon^{2|m|+1}} = A_X^2 A_Y^2 \tag{49}$$

Note that the normalization constants are functions of Z_1, F and E. The total density of states is defined as the incoherent sum of $A_X^2 A_Y^2$ over all n_1 channels, $\mathrm{DoS}(F,E) = \sum_{n_1,m} \mathrm{DoS}_{n_1,|m|}$.

In order to show the importance of this quantity let us consider the energy evolution of a single channel $\mathrm{DoS}_{n_1,|m|}$. The energy evolution of $2Z_1^{n_1,|m|}$ for F=1000 V/cm, n_1=38 and m=0 is shown in Figure 9(a) as a monotonous decreasing function. A_X^2 (shown in Figure 9(b)) is also a slowly-varying decreasing function of energy and becomes negligible for $Z_1^{n_1,|m|}(E) < 0$. This phenomenon is referred as channel closing and is a common feature of all channels at some n_1-dependent energy. The physical picture of this effect is shown in Figure 9(e). The potential $U_X^{eff}(\chi)$ for ε=+0.99 presents a negative minimum and as a result a number of $2Z_1$ eigenvalues will be negative. Then the X-wave function is "pushed" to large distances and A_X^2 becomes negligible therefore, the $\mathrm{DoS}_{n_1,|m|}$ will also be negligible (see Figure 9(c)). As the energy evolution of $\mathrm{DoS}_{38,0}$ implies, A_Y^2 is negligible for $Z_2^{n_1,|m|}(\varepsilon) < 0$ that is, for $Z_1^{n_1,|m|}(\varepsilon) > Z$ (Figure 9(d)). Indeed, for ε=+0.01, the Y-wave function can only approach υ=0 region via tunneling and the channel not considered open yet, Figure 9(d). Note that the $U_Y^{eff}(\upsilon)$ potential for ε>0 does not exhibit any local minima, thus it does not support resonant states. In conclusion, for this particular n_1 channel, the channel opens at some positive energy and is a continuum channel (characterized by two quantum numbers (n_1, m)) until the channel closing occurs at even higher energies. This, is consistent with the classical limits $0<Z_1<Z$, due to the interpretation of Z_1 for positive energies i.e. in the absence of a critical angle β_c.

As a more complicated example we present the $\mathrm{DoS}_{n_1,|m|}$ for F=1000 V/cm, n_1=20 and m=0 in Figure 10. The behavior of $Z_1^{n_1,|m|}(\varepsilon)$ and A_X^2 Figure 10(a,b) is similar to the previous example. On the other hand, $2Z_2^{n_2,|m|}(F,\varepsilon)$ may lie above or below the υ-potential barrier. This introduces a channel threshold written as:

$$E_{thr}^{n_1,|m|} = -2\left[Z_2^{n_1,|m|}\left(F, E_{thr}^{n_1,|m|}\right)F\right]^{1/2} \tag{50}$$

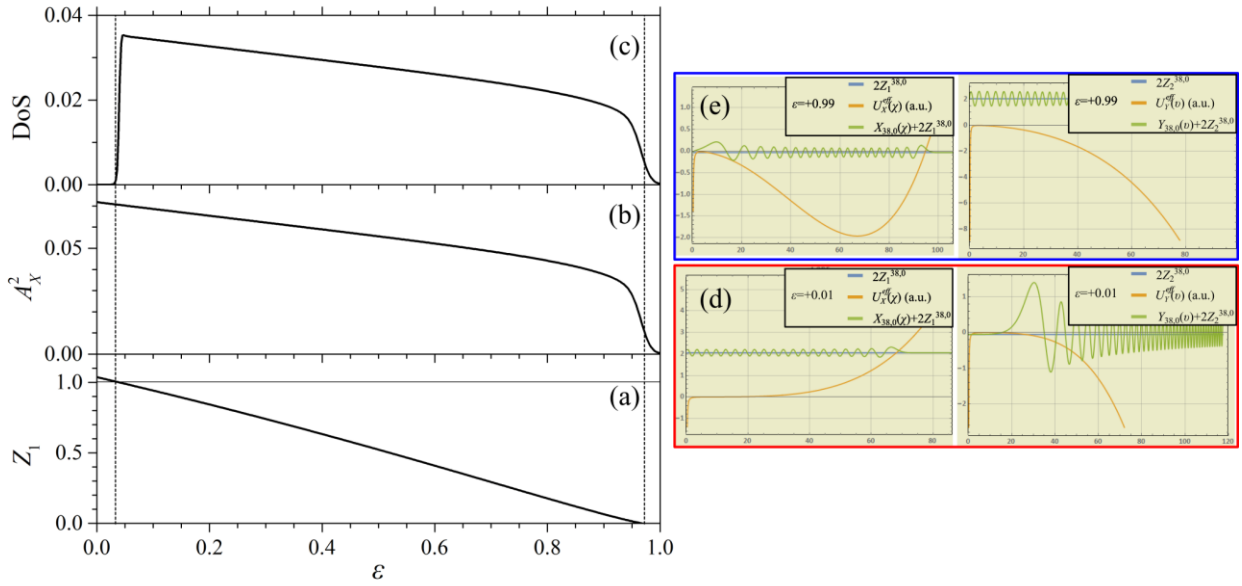

Figure 9. (a) Energy evolution of $Z_1^{38,0}(\varepsilon)$ for the energy range $0\leq \varepsilon \leq +1$ and a field value F=1000 V/cm. (b) Energy evolution of the normalization factor $A_X^2(\varepsilon)$ for the n_1=38 channel. (c) Energy evolution of $DoS_{38,0}$ as defined in the main text. (d) Effective potentials $U_X^{eff}(\chi)$, $U_Y^{eff}(\upsilon)$, effective eigenvalues $Z_1^{38,0}$, $Z_2^{38,0}$ and wavefunctions $X_{38,0}$, $Y_{38,0}$ for ε=+0.01 slightly before the channel opening. Note that the inner well in the υ coordinate is absent for positive energies. (e) Same as (d) but for ε=+0.99, slightly above the channel closing. The X-wave function is pushed to large χ values and obtains negligible values near the origin.

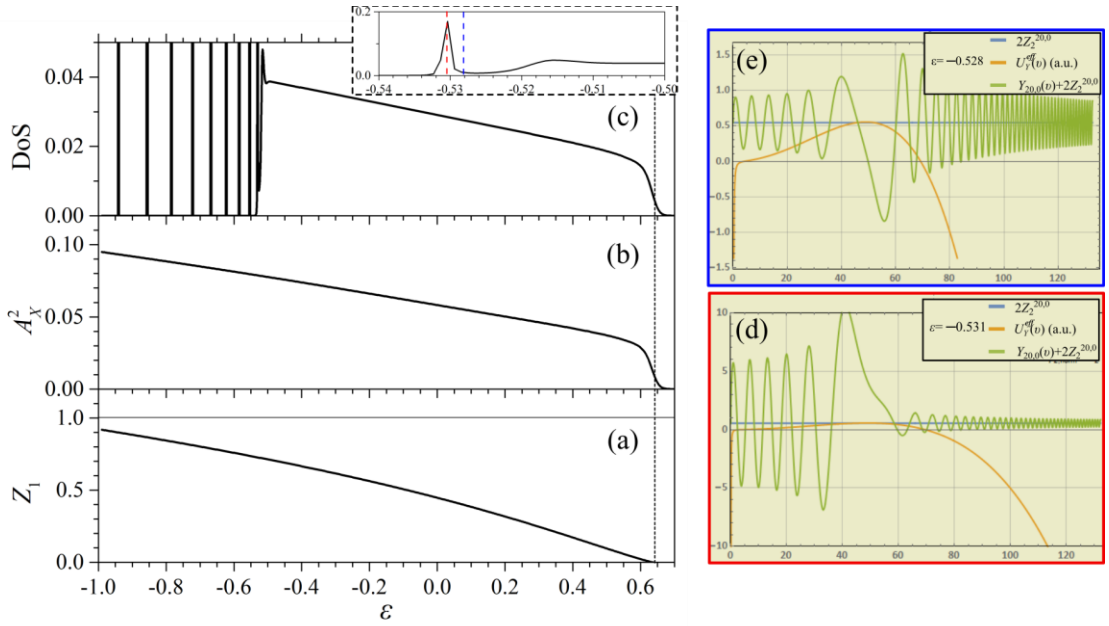

Figure 10. (a) Energy evolution of $Z_1^{20,0}(\varepsilon)$ for the energy range $-1 \leq \varepsilon \leq +0.7$ and a field value F=1000 V/cm. (b) Energy evolution of the normalization factor $A_X^2(\varepsilon)$ for the n_1=20 channel. (c) Energy evolution of $DoS_{20,0}$. The DoS form exhibits a resonant behavior and then a smooth evolution in contrast to the DoS shown in Figure 9(c). The inset shows the DoS in the energy range of the last sharp resonance and marks the energy position of Figures 10(d,e). (d) $U_Y^{eff}(\upsilon)$ and $Y_{20,0}$ for ε= –0.531 that corresponds to a resonance with n_2=10. (e) $U_Y^{eff}(\upsilon)$ and $Y_{20,0}$ for ε= –0.528, slightly above the resonant energy, that exhibits a small amplitude inside the well.

For $E > E_{thr}^{n_1,|m|}$ the electron escapes over the barrier in the υ-coordinate and the total electronic state is a continuum state (only two quantum numbers (n_1, m) are required for its characterization and labeling). For $E < E_{thr}^{n_1,|m|}$ the electron can escape solely via tunneling. For certain energies $Z_2^{n_1,|m|}(F,\varepsilon)$ coincides with the inner well eigenvalues and A_Y^2 acquires large values, implying that the electron is trapped within the barrier and the state exhibits an appreciable lifetime (see Figure 10(d)). These quasi-bound resonant states are characterized by the enlarged set of three quantum numbers (n_1, n_2, m). This is not the case for energies slightly above or below a resonance as it is shown in Figure 10(e) where the Y-wave function has almost zero amplitude inside the inner well. In conclusion, the channel opens at some negative energy ($Z_1 \approx 1$), then the single-channel DoS exhibits a resonant structure and then the channel is transformed to a continuum one (near the root of Eq. (50)) with a slowly varying DoS amplitude (see Figure 10(c)) until it finally closes ($Z_1 \approx 0$). Note that for positive energies there is no energy threshold imposed by Eq. (50) and all channels correspond to continuum states. Moreover, due to the fact that channel openings and closings are not abrupt, the quantum calculations should include channels corresponding to classically forbidden Z_1 values, i.e. values that slightly violate $0 \leq Z_1 \leq Z$ range.

1.2.2 Photo-Excitation Dipole Transition Matrix Elements

Having described the characteristics of the $X_{n_1,|m|}(\chi)$ and $Y_{n_1,|m|}(\upsilon)$ components of a given excited Stark state,

$$\psi_{n_1,m}^F(\mathbf{r}) = (2\pi\chi\upsilon)^{-1/2} X_{n_1,|m|}(\chi) Y_{n_1,|m|}(\upsilon) e^{im\varphi} \tag{51}$$

we now turn to its radiative excitation out of an initial state ψ_i (of energy E_i and azimuthal quantum number m_i). The single-photon dipole operator responsible for the transition writes,

$$\hat{\mathrm{T}} = \boldsymbol{\varepsilon} \cdot \mathbf{r} \tag{52}$$

and the matrix element connecting initial and final states is written as,

$$d_{n_1,|m|} = \langle \psi^F_{n_1,|m|} | \boldsymbol{\varepsilon} \cdot \mathbf{r} | \psi_i \rangle \tag{53}$$

The small field strengths employed throughout this work allows for neglecting the static electric field in the cases of the low-lying atomic states such as the ground or the first, low lying, excited states. Recalling that field-free hydrogenic Hamiltonian in separable in semi-parabolic coordinates, the initial state wave functions are also written in the form of Eq. (36), $\psi_i(\mathbf{r}) = (2\pi\chi\upsilon)^{-1/2} X_i(\chi) Y_i(\upsilon) e^{im_i\varphi}$. The X_i and Y_i components turn out to be the well-known harmonic oscillator solutions [75]. Initial states will be labeled hereafter as $|n, n_1, n_2, m\rangle$ where the principal quantum number $n=n_1+n_2+|m|+1$ [13,14,75]. In the present work we employ solely $m_i=0$ initial state wave functions, given by [27],

$$\begin{aligned} X_i &= X_{n,n_1,0} = N_{X,n,n_1,0}\, \chi^{-1/2} \exp\left[-\frac{Z\chi^2}{2n}\right] \mathrm{L}_{n_1}\left[\frac{Z\chi^2}{n}\right] \\ Y_i &= Y_{n,n_2,0} = N_{Y,n,n_2,0}\, \upsilon^{-1/2} \exp\left[-\frac{Z\upsilon^2}{2n}\right] \mathrm{L}_{n_2}\left[\frac{Z\upsilon^2}{n}\right] \end{aligned} \tag{54}$$

where the functions L_n denote the n-th Laguerre polynomials and $N_{X,Y}$ are normalization factors. The factor $N_{X,n,n_1,0}$ is found by normalizing $X_{n,n_1,0}$ as in Eq. (41), while the factor $N_{Y,n,n_2,0}$ by normalizing the bound ψ_i state to unity. Finally, the energy of a given $|n, n_1, n_2, m\rangle$ state is given by the well-known hydrogen energy level formula,

$$E_n = -\frac{Z^2}{2n^2} \tag{55}$$

By employing the volume element

$$dV = \chi\upsilon(\chi^2 + \upsilon^2) d\chi d\upsilon d\varphi \tag{56}$$

and when the linear polarization vector is parallel to $\boldsymbol{F} = F\hat{\boldsymbol{z}}$, that is $\boldsymbol{\varepsilon}\cdot\mathbf{r} = z = (\chi^2 - \upsilon^2)/2$ (π-polarization), the resulting matrix element is written as,

$$d_{n_1,m} = \delta_{m,m_i} D^{\pi}_{n_1,|m|} \tag{57}$$

where,

$$D^{\pi}_{n_1,|m|} = \frac{1}{2}\iint_0^{\infty} X_i X_{n_1} Y_i Y_{n_1} (\chi^4 - \upsilon^4) d\chi d\upsilon \tag{58}$$

is a (real) "radial" matrix element, while the δ_{m,m_i} factor emerges from the angular φ-integration and leads to the selection rule $\Delta m = m - m_i = 0$. The integrals converge to a finite value due to the bound character if the initial state, despite the oscillatory large-υ behavior of $Y_{n_1,|m|}$.

Next, consider the quite common experimental arrangement of a laser beam propagating perpendicularly to the field along the *x*-axis and the linear polarization is perpendicular to the field along the *y* axis (σ-polarization). Then, $\boldsymbol{\varepsilon}\cdot\mathbf{r} = y = \chi\upsilon \sin\varphi$ and the resulting matrix element writes,

$$d_{n_1,m} = \frac{\delta_{m,m_i+1} - \delta_{m,m_i-1}}{2i} D^{\sigma}_{n_1,|m|} \tag{59}$$

where

$$D^{\sigma}_{n_1,|m|} = \iint_0^{\infty} X_i X_{n_1} Y_i Y_{n_1} \chi\upsilon (\chi^2 + \upsilon^2) d\chi d\upsilon \tag{60}$$

Here again the factor $\frac{\delta_{m,m_i+1} - \delta_{m,m_i-1}}{2i}$ stems from the angular integration and leads to the selection rule $\Delta m = \pm 1$.

In the present thesis we also consider a two-identical-photon excitation out of the ground state $\psi_i = \psi_g = |1,0,0,0\rangle$. Assuming there is no one-photon resonant intermediate state, the two-photon transition is described by a single-photon one out of a virtual state ψ_{v}. The latter is calculated within the perturbative Dalgarno-Lewis method [82,83] i.e. by solving the inhomogeneous equation:

$$\left[-\frac{1}{2}\nabla^2 - \frac{Z}{r} - E_{\mathrm{v}}\right]\psi_{\mathrm{v}} = -\boldsymbol{\varepsilon}\cdot\mathbf{r}\,\psi_i \tag{61}$$

where the virtual state energy $E_{\mathrm{v}} = (E + E_g)/2$. The solution is written as:

$$\psi_{\mathrm{v}}(\mathbf{r}) = (2\pi\chi\upsilon)^{-1/2} \sum_{N_1,M}\left[X_{N_1,|M|}(\chi) Y_{N_1,M}(\upsilon) e^{iM\varphi}\right] \tag{62}$$

and where the *M* summation runs over positive and negative values of *M* and its values are determined by selection rules applied to the $\psi_g \rightarrow \psi_{\mathrm{v}}$ transition. Hence, the problem is reduced to the calculation of the bound-like *X*,*Y*-wave functions of the virtual state and more details about the numerical solution of Eq. (61) are given in [27]. The general two-photon matrix element is given by,

$$d^{(2)}_{n_1,m} = \sum_{N_1,M} \left[\begin{array}{c} \iint_0^\infty X_{N_1,|M|} X_{n_1,|m|} Y_{N_1,M} Y_{n_1} (\chi^2 + \upsilon^2) d\chi d\upsilon \\ \times \int_0^{2\pi} \boldsymbol{\varepsilon} \cdot \mathbf{r} \frac{e^{i(M-m)\varphi}}{2\pi} \end{array} \right] \tag{63}$$

and incorporates additional selection rules applied to the $\psi_v \rightarrow \psi^F_{n_1,m}$ transition. Finally, the imposed condition $0 \leq Z_1^{N_1,|M|} \leq Z$, leads to an energy dependent maximum value for N_1, while $N_{1,max}=0$ for the energy range of our interest.

1.2.3 Electron Current Probability Density

In scattering experiments, the total information is projected in the electron current density $\mathbf{J} \propto i[\psi \boldsymbol{\nabla} \psi^* - \psi^* \boldsymbol{\nabla} \psi]$. Since the electron can escape (reach arbitrary large distances) solely through the υ coordinate, the probability current density is defined on paraboloid of constant $\upsilon=\upsilon_{det}$. The projection of the electron current probability density vector on the υ-unit vector $\mathbf{e}_\upsilon$ has the general form of [12,27]:

$$\mathrm{J}_\upsilon = \mathbf{J} \cdot \mathbf{e}_{\boldsymbol{\upsilon}} = \frac{i\,\pi\alpha\omega}{[\chi^2+\upsilon^2]^{1/2}} \left[\psi^+_{out} \frac{\partial}{\partial \upsilon} (\psi^+_{out})^* - (\psi^+_{out})^* \frac{\partial}{\partial \upsilon} \psi^+_{out} \right] \tag{64}$$

where α denotes the fine structure constant and ω is the frequency corresponding to the energy difference between the initial and the final states of the considered transition. The outgoing wave function ψ^+_{out} is the solution to the Time Dependent Schrodinger Equation (TDSE). Within the first-order perturbation theory that is for a weak laser field of constant amplitude and for long laser-atom interaction times the TDSE is reduced to the following Dalgarno-Lewis-like equation, typically referred as the Schrödinger equation with a source [25,84,85],

$$\left[-\frac{1}{2}\nabla^2 - \frac{Z}{r} - E \right] \psi^+_{out} = -\hat{\mathrm{T}}\, \psi_i \tag{65}$$

where ψ_i is the (physical or virtual) initial state wave function. The solutions of the above equation are put to the form,

$$\psi^+_{out}(\boldsymbol{r}) = (2\pi\chi\upsilon)^{-1/2} \sum_{n_1,m} X_{n_1,|m|}(\chi)\, y^+_{n_1,m}(\upsilon) e^{im\varphi} \tag{66}$$

where $X_{n_1,|m|}$ are the previously calculated solutions of the homogenous problem of Eq. (37) and the $y^{+}_{n_1,m}$ wave function are to be determined. Plugging the above ansatz into Eq. (65) and following the derivation of Ref. [25,27] it turns out that asymptotically (large υ values),

$$y^{+}_{n_1,m}(\upsilon) = -\frac{2}{C_Y} d_{n_1,m} M_{n_1,|m|}(\upsilon) e^{i[\theta_{n_1,|m|}(\upsilon)+\phi_{n_1,|m|}]} \tag{67}$$

while the calculation of all components has been already discussed i.e. the Milne functions $M_{n_1,|m|}$, the *Y*-wave function phases $\theta_{n_1,|m|}(\upsilon) + \phi_{n_1,|m|}$ and the relevant matrix elements $d_{n_1,m}$. Then the asymptotic form of the electron current probability density of Eq. (64) is written as,

$$\mathrm{J}_\upsilon(\varphi,\chi) = \frac{4\,C_Y^{-2}}{2\pi\,\chi\upsilon[\chi^2+\upsilon^2]^{1/2}} \left| \sum_{n_1,m} \left\{ d_{n_1,m} X_{n_1,|m|}(\chi) e^{im\varphi} e^{i[\theta_{n_1,|m|}(\upsilon)+\phi_{n_1,|m|}]} \right\} \right|^2 \tag{68}$$

and incorporates the angular distribution of the outgoing electron flux. In fact, the angular distribution is incorporated exclusively in the $d_{n_1,m}$ and $e^{im\varphi}$ terms. The detector plane differs from the paraboloid surface by $\Delta z \approx 0$ (see section 1.1.2).

Integration over the whole paraboloid surface ($0<\chi<\infty$) and ($0<\varphi<2\pi$) provides the total cross section σ_{tot} i.e. the total electron signal,

$$\sigma_{\mathrm{tot}} = \int \mathrm{J}_\upsilon(\varphi,\chi) dS = 4\pi^2 \alpha\omega \sum_{n_1,m} \left| d_{n_1,m} \right|^2 \tag{69}$$

where $dS=\chi\upsilon[\chi^2 + \upsilon^2]^{1/2} d\chi d\phi$ is the surface element on the detector. For deriving Eq. (69) we used the orthogonality properties of the *X*-wave functions (Eq. (41)) and states of different *m*. Obviously, σ_{tot} is proportional to the incoherent sum of the squared matrix elements.

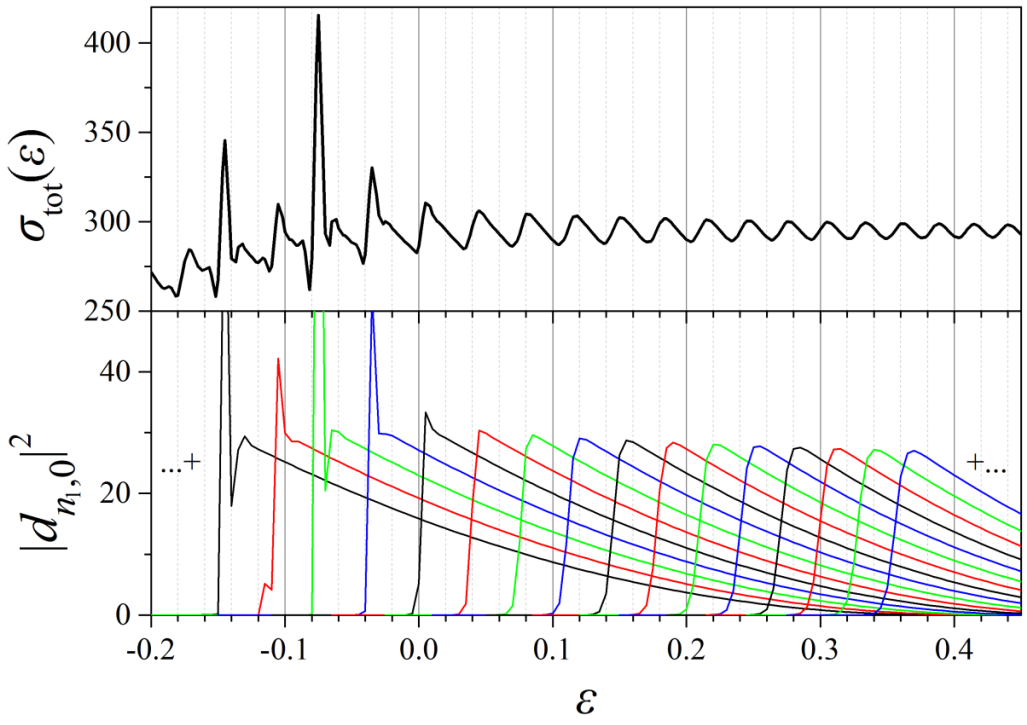

Figure 11. (a) Total cross section σ_{tot} for positive energies and F=1000 V/cm. The final states are excited out of the ground state via one photon π polarization. Note that the total electron signal is characterized by oscillations which are attributed to SFIS. The contrast of these oscillations depends on the initial state and excitation scheme. (b) Single channel matrix elements $|d_{n_1,m}|^2$ for m=0 and for various n_1 values (n_1=33 – 48). The channel openings are associated to the oscillations observed in σ_{tot}.

The polar coordinate on the detector is $\rho=\chi v_{det}\propto\chi$ while, for $v_{\rm det}\to\infty$, $\left[\chi^2+v_{\rm det}^2\right]^{1/2}\approx v_{\rm det}$ and Eq. (68) is simplified,

$$\mathrm{J}_{v_{det}}(\varphi,\rho)\propto\frac{1}{\chi}\left|\sum_{n_1,m}\left\{d_{n_1,m}X_{n_1,|m|}(\chi)e^{im\varphi}e^{i\left[\theta_{n_1,|m|}(v_{det})+\phi_{n_1,|m|}\right]}\right\}\right|^2. \tag{70}$$

A quantity of primary interest in this thesis is the radial distribution obtained after angularly integrating J,

$$R(\rho)\equiv\int_0^{2\pi}\mathrm{J}_{v_{det}}(\varphi,\chi)d\varphi \tag{71}$$

and can be regarded as the electron's transverse (to the field) momentum distribution [27,53]. In the case where solely m=0 states contribute to the current density the radial distribution incorporates all the available information of the image in a one-dimensional curve. For avoiding

misinterpretations, note that the term "radial distribution" is more frequently employed for $P(\rho)=\rho R(\rho)$, which is proportional to the number of electrons hitting the detector within the $[\rho, \rho + d\rho]$ interval.

Figure 12 shows the electron current probability density of m=0 final states out of the hydrogen ground state for a single photon transition. Also shown is the corresponding radial distribution that reproduces the interference pattern of the image, arising from the coherent summation of the X-wave functions.

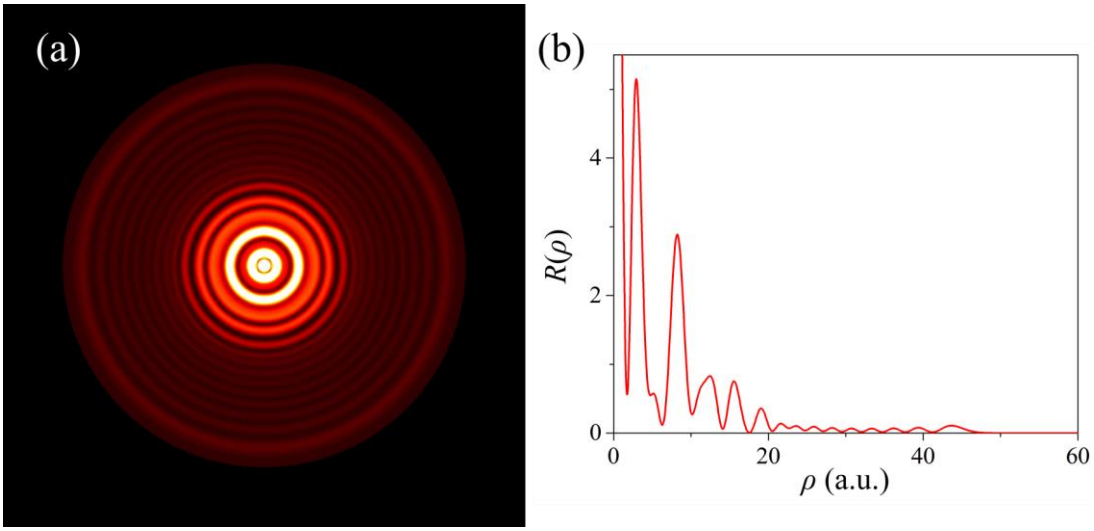

Figure 12. (a) Electron current probability density for ε= –0.5>ε_{dir} and F=1000 V/vm. The color scale is linear while white color denotes intensity cuts. The horizontal and vertical axes refer to the x and y coordinates of the detector, respectively. The detector is placed at z_{det}=2000 (a.u.). The final states are single photon excited out of the ground state with π polarization. Notice that the image shows no angular distribution (m=0). (b) Radial distribution $R(\rho)$ of the image of (a).

The image features all the relevant structures of classical and semi-classical origin such as the Bow and Glory scattering. Due to the small χ asymptotic form of the X-wave functions Eq. (39), the glory signal is formed solely by the m=0 terms of Eq. (70),

$$\mathrm{J}_{\upsilon_{\mathrm{det}},\mathrm{Glory}} \propto \left|\sum_{n_1}\left\{d_{n_1,0}A_{X,n_1,0}e^{i[\theta_{n_1,0}(\upsilon_{\mathrm{det}})+\phi_{n_1,0}]}\right\}\right|^2 \tag{72}$$

The phase factors and the normalization constants $A_{X,n_1,0}$, characterize the final Stark states. On the other hand, the excitation matrix elements depend strongly on the initial state and

excitation scheme. Finally, note that the current density as well as all the other observables presented above exhibit a pronounced dependence on the electron excitation energy *E*.

1.2.4 Extensions to the non-hydrogenic case

The Hamiltonian of a (static-field free) multi-electron atom may be written as the sum of kinetic energy operators for each electron, plus a potential energy term composed mainly by all electron-nucleus attractions and all electron-electron repulsions. In addition, the potential energy also contains other fine structure interactions, such as the spin-orbit one, that may, to a first approximation, be ignored when highly excited atomic states of a valence electron are of interest. Assuming further that we deal with a single highly excited electron outside of a closed subshell ionic core of charge Z_{eff} (or at least outside of a partially open but spherically symmetric core, as for example the Mg^+ [Ne]3s one), all electrostatic attractions and repulsions concerning all electrons but the outer valence one may be replaced by a spherically symmetric parametric potential $U(\mathbf{a};r)$ [86,87,88,89], with $\mathbf{a}=\{a_1,a_2,\ldots,a_N\}$ a parameter vector. In fact, experience shows that for obtaining energy level positions and wave-functions of highly excited states with good accuracy, all the parameters should depend on the angular momentum quantum number *l* of the outer electron [88]. Further, we can put $U(\mathbf{a};r)$ in the form,

$$U(\mathbf{a};r) = -\frac{Z_{\text{eff}}+\Delta Z(\mathbf{a};r)}{r} \tag{73}$$

where for $r\to 0$, $\Delta Z(\mathbf{a};r)\to Z-Z_{\text{eff}}$ and the electron "sees" the full nuclear charge. On the other hand, for $r\to\infty$, $\Delta Z(\mathbf{a};r)\to 0$ and the electron moves in the hydrogenic potential. The presence of the non-coulombic short-range part $\Delta Z(\mathbf{a};r)$ emerging from the existence of the core, results to highly excited (Rydberg) energy levels given by the Rydberg formula [13,14],

$$E_{n,l} = -\frac{Z_{\text{eff}}^2}{2(n-\mu_l)^2}\,, \tag{74}$$

with μ_l being the so-called quantum defects [13,14,86]. The latter are a measure of the penetration of the excited electron's wave function to the ionic core and they are nearly constant with energy [86] but decrease rapidly with *l*. In fact, the quantum defects reflect the dephasing of the electron's

wave function with respect to its hydrogenic $|n,l\rangle$ counterpart and this phase shift is given by [86,90]

$$\delta_l = \pi \cdot \mu_l \,. \tag{75}$$

Adopting the above description where the outer-valence-electron is subjected to the action of the parametric potential $U(\mathbf{a};r)$, the additional presence of a static field leads to the following Schrödinger equation,

$$\left[-\tfrac{1}{2}\nabla^2 + U(\mathbf{a};r) + Fz - E\right]\psi(\boldsymbol{r}) = 0 \tag{76}$$

In a first attempt to solve Eq. (76) we follow Refs. [29,86] and we introduce the single-m ansatz (m is still a good quantum number in the absence of the electron spin and spin-orbit coupling [29]),

$$\psi(\boldsymbol{r}) = (2\pi\chi\upsilon)^{-1/2} \sum_{n_1'} X_{n_1',|m|}(\chi)\, \mathcal{Y}_{n_1',|m|}(\upsilon) e^{im\varphi} \tag{77}$$

where the wave functions $X_{n_1',|m|}$ are the hydrogenic ones, i.e. they are solutions of Eq. (37) and they are associated with the eigenvalues $Z_1^{n_1',|m|}$. As for the functions $\mathcal{Y}_{n_1',|m|}$, they need to be determined. After appropriate manipulations and by making use of the orthonormality of the wave functions $X_{n_1',|m|}$ (see Eq. (41)) we arrive at the coupled system of equations,

$$\left[-\tfrac{1}{2}\frac{d^2}{d\upsilon^2} + U_Y^{eff}(\upsilon) - 2\left(Z_2^{n_1,|m|} + V_{n_1,n_1}^{|m|}(\upsilon)\right)\right]\mathcal{Y}_{n_1,|m|}(\upsilon) - 2\sum_{n_1'\neq n_1} V_{n_1,n_1'}^{|m|}(\upsilon)\mathcal{Y}_{n_1',|m|}(\upsilon) = 0 \tag{78}$$

where the hydrogenic potential $U_Y^{eff}(\upsilon)$ is defined in Eq. (38),

$$Z_2^{n_1,|m|} = Z_{\text{eff}} - Z_1^{n_1,|m|} \tag{79}$$

and

$$V_{n_1,n_1'}^{|m|}(\upsilon) = \int_0^\infty X_{n_1,|m|}(\chi)\Delta Z\left(\mathbf{a}; r = \tfrac{\chi^2+\upsilon^2}{2}\right) X_{n_1',|m|}(\chi)d\chi \tag{80}$$

It is evident from Eq. (80) that the coupling between channels is due to the short range non-coulombic part ΔZ of $U(\mathbf{a};r)$ and disappears if ΔZ=0. The involved coupled hydrogenic channels may refer to solely closed channels, open channels, or open and closed ones. The latter is of particular importance in PM since it implies that any initially prepared resonant population will be

eventually spread out over many continua and the resonant features of the image may be obscured. Also, of importance is the case of the coupling between at least two closed channels (in addition perhaps to the coupling with other degenerate open ones). In fact, even in the absence of continua, this coupling has been proved to produce interesting effects such as the so called "avoided crossings" between pairs of resonances [28], where one of them is effectively decoupled from the continua in the vicinity of the crossing [23].

Despite the appealing form of the coupled system Eq. (78), in practice its solution is difficult and suffers from several limitations. For example, the function $\Delta Z(\mathbf{a};r)$ can be complicated and consequently the functions $V^{|m|}_{n_1,n_1'}(\upsilon)$, can be difficult to compute. Moreover, the form of the coupled system does not allow for the beneficial employment of an *l*-dependent parameter vector $\mathbf{a}_l$. For the above reasons, we introduce the reader to the so-called Frame Transformation Theory (FTT) developed by Fano [91] and Harmin [62,92] and recently reformulated and adapted to PM by Giannakeas et all [32]. We shall not introduce the theory in detail here but we shall restrict ourselves to a recapitulation of its results. Let us first mention that, in FTT the core presence and the mixing it induces are introduced solely via the non-zero quantum defects (see Eq. (75) above). This emerges from a semi-parabolic to spherical coordinate transformation at short distances where the interaction between the ionic core and the excited valence electron dominates over the interaction between the electron and the static field. Due to this dominance, the electric field term may be neglected in the core region and the fairly simple form of the zero-field transformation can be used, implicating, however, static field-dependent normalization factors [32,91]. Additionally, the application of this transformation has yet another virtue, namely it allows for the calculation of excitation matrix elements at zero-field. This, in turn, allows for the employment of the far more accurate *l*-dependent parametric potentials. With the above discussion in mind we note that the form of the current probability density of Eq. (68) remains formally unchanged (along with the form of all other related observables) and involves hydrogenic, $X_{n_1,|m|}(\chi)$ functions and $\theta_{n_1,|m|}(\upsilon)+\phi_{n_1,|m|}$ phases. The differences concern exclusively the matrix elements which acquire different absolute values and phases reflecting the n_1–channel mixing. Namely, they are now given by

$$d_{n_1,m}=\sum_l\sum_{n_1'}\left\{d_l^m W^m_{l,n_1'}B^m_{n_1',n_1}\right\} \tag{81}$$

where d_l^m are *zero-field* excitation matrix elements for all l values permitted by the relevant selection rules. The matrices **W**, **B** are given by,

$$\mathbf{B}^{|m|} = \left[\mathbf{I} - i\mathbf{R}^{|m|}\right]^{-1} \tag{82}$$

and

$$\mathbf{W}^{m} = \cos\boldsymbol{\delta}^{-1}\mathbf{U}^{\mathrm{T},m}\left[\mathbf{I} - \cot\gamma^{|m|}\mathbf{K}^{|m|}\right]^{-1} \quad , \quad \mathbf{W}^{-m} = (-1)^{|m|}\mathbf{W}^{|m|} \, , \tag{83}$$

where **I** is the identity matrix,

$$\mathbf{R}^{|m|} = \mathbf{K}^{|m|}\left[\mathbf{I} - \cot\gamma^{|m|}\mathbf{K}^{|m|}\right]^{-1} \tag{84}$$

is the reactance matrix and

$$\mathbf{K}^{|m|} = \mathbf{U}^{m}\tan\boldsymbol{\delta}\,[\mathbf{U}^{m}]^{\mathrm{T}} \, . \tag{85}$$

is the so-called **K** matrix. Note that the reactance matrix **R** is not to be confused with the Wigner-Eisenbud *R*-matrix [32]. The frame transformation matrix **U** (with $\mathbf{U}^{-m} = (-1)^{|m|}\mathbf{U}^{|m|}$) essentially maps the Stark parabolic channels into their spherical zero-field counterparts [32,62,91,92]. The diagonal matrices cos**δ** and tan**δ** are constructed by means of the phases given by Eq. (75) that can be determined by the quantum defects extracted from spectroscopic data. Finally, the cot**γ** matrix is of hydrogenic origin. Specifically, it is defined as the n_1-specific relative phase between the regular and irregular hydrogenic *Y*-wave functions. In other words, by imposing γ=π/2 for $\upsilon\to0$ one gets $\gamma = \gamma_{n_1}$ for $\upsilon\to\infty$. This definition differs from the typical one employed in scattering theory, were the regular and irregular functions are phase-lagged by π/2 at large distances. Eq. (81) shows clearly the n_1–channel mixing while it is evident that by setting all quantum defects equal to zero (hydrogen atom) this mixing disappears (**R**=**K**=0). Furthermore, the form of Eq. (82) shows that the matrix elements $d_{n_1,m}$ become necessarily complex. Thus, apart from the atom specific magnitude differences with respect to the hydrogenic matrix elements of the same n_1, atom-specific phase-shifts are also added to the hydrogenic phases $\theta_{n_1,|m|}(\upsilon) + \phi_{n_1,|m|}$.

In the present thesis we shall make a limited use of FTT relations, in order to compare with our experimental results for the magnesium atom. Note that for the excitation energies employed

here, the zero-field matrix elements d_l^m connect the Mg ground state to Rydberg states with a principal quantum number of $n\sim30$. Finally, since the current density along with the form of all other related observables remain formally unchanged, non-resonant effects in Mg afford a qualitative comparison with the hydrogenic theory [27].

1.3 Polarization Effects in Photoionization Microscopy

1.3.1 Linear Polarization Rotation Effects in Photoionization Microscopy Images

Let us now examine a two-photon excitation scheme out of the hydrogenic ground state that will be useful in the analysis of the experimental results. According to this scheme the linear polarization vector of the exciting radiation forms an angle Θ with respect to **F**. More specifically, as shown in Figure 13, the polarization vector **ε** lies in the *y*–*z* plane and the laser beam propagates in the *x* direction. This scheme addresses all the important physical excitation mechanisms and corresponds to the majority of experiments conducted in the present thesis. More complex geometries, considering possible experimental misalignments, as shown in Figure 15, are considerably more difficult to handle while they do not introduce any additional excitation pathways. Therefore, they are discussed later on, in order to propose a self-consistent alignment procedure in section 3.3.1.

In the geometry presented in Figure 13, the relevant single-photon transition operator $\hat{\mathrm{T}}$ of Eq. (52) writes,

$$\hat{\mathrm{T}} = \cos\Theta z + \sin\Theta y = \cos\Theta \frac{\chi^2 - v^2}{2} + \sin\Theta\, \chi v \frac{e^{i\varphi} - e^{-i\varphi}}{2i} \tag{86}$$

in Cartesian and semi-parabolic coordinates respectively.

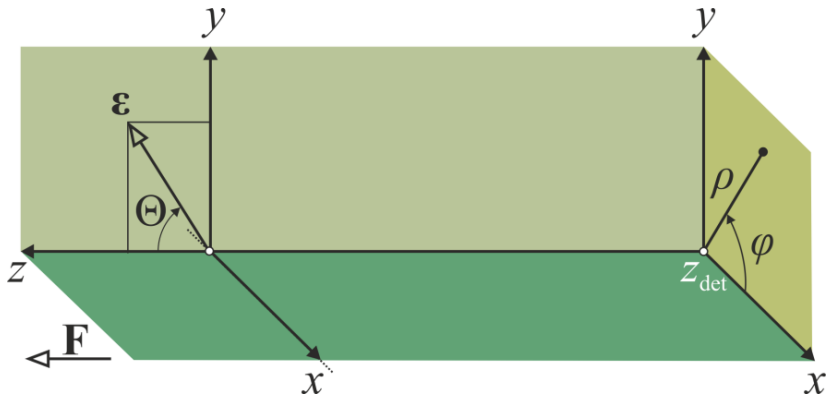

Figure 13. Schematic representation of the laser-spectrometer configuration. The laser beam propagates towards the *x* axis. The radiation polarization lies in the *y*-*z* plane while the static electric field point toward the *z* direction. The polarization vector and the static electric field form an angle Θ. The detector's coordinates (*x*, *y*) or (*ρ*, *φ*) are also shown.

Plugging the transition operator in Eq. (61) provides the virtual state ψ_{v} in the form,

$$\psi_{\mathrm{v}}(\mathbf{r}) = (2\pi\chi\upsilon)^{-1/2} \sum_{N_1} \left[\cos\Theta X_{N_1,0} y_{N_1,0} + \sin\Theta X_{N_1,1} y_{N_1,1} \left(\frac{e^{i\varphi}-e^{-i\varphi}}{2i}\right)\right] \tag{87}$$

and the $y_{N_1,|M|}(\upsilon)$ wave functions are connected to the $Y_{N_1,M}(\upsilon)$ wave functions of Eq. (62) by the relations $Y_{N_1,0} = \cos\Theta y_{N_1,|0|}$, $Y_{N_1,1} = \frac{\sin\Theta}{2i} y_{N_1,|1|}$ and $Y_{N_1,-1} = -\frac{\sin\Theta}{2i} y_{N_1,|1|}$. By using Eqs. (51,86,87), the general two-photon matrix element of Eq. (63) writes:

$$d^{(2)}_{n_1,m} = \sum_{N_1} \begin{bmatrix} \int_0^\infty d\upsilon Y_{n_1,|m|} \int_0^\infty d\chi X_{n_1,|m|} (\chi^2+\upsilon^2) \int_0^{2\pi} d\varphi \frac{e^{-im\varphi}}{2\pi} \\ \times \left[\cos\Theta \frac{\chi^2-\upsilon^2}{2} + \sin\Theta\, \chi\upsilon \frac{e^{i\varphi}-e^{-i\varphi}}{2i}\right] \\ \times \left[\cos\Theta X_{N_1,0} y_{N_1,0} + \sin\Theta X_{N_1,1} y_{N_1,1} \left(\frac{e^{i\varphi}-e^{-i\varphi}}{2i}\right)\right] \end{bmatrix} \tag{88}$$

After some manipulations, the insertion of the matrix elements to Eq. (68) and the collection of terms of equal $|m|$, the electron current density $\mathrm{J}_{\upsilon_{\mathrm{det}}}$ is written as,

$$\mathrm{J}_{\upsilon_{\mathrm{det}}}(\varphi,\chi) \propto \frac{1}{\chi} \left| \sum_{n_1} \begin{Bmatrix} \left(\cos^2\Theta\, D^{\pi(2)}_{n_1,0} + \frac{\sin^2\Theta}{2} D^{\sigma(2)}_{n_1,0}\right) e^{i\theta^*_{n_1,0}} X_{n_1,0}(\chi) \\ +\cos\Theta \sin\Theta \sin\varphi \left(D^{\pi(2)}_{n_1,1} + D^{\sigma(2)}_{n_1,1}\right) e^{i\theta^*_{n_1,1}} X_{n_1,1}(\chi) \\ -\frac{\sin^2\Theta}{2}\cos(2\varphi) D^{\sigma(2)}_{n_1,2} e^{i\theta^*_{n_1,2}} X_{n_1,2}(\chi) \end{Bmatrix} \right|^2 \tag{89}$$

where the notation $e^{i\theta^*_{n_1,|m|}} = e^{i[\theta_{n_1,|m|}(\upsilon_{\mathrm{det}}) + \phi_{n_1,|m|}]}$ is introduced for simplicity. Despite being lengthy, the above formula clearly demonstrates the simultaneous excitation of all $|m|$=0,1,2 final states. Each m-term is comprised by the corresponding, angular weights depending on the angle Θ, the $X_{n_1,|m|}(\chi)$ wave functions, the υ_{det}-dependent phase factors, the involved matrix element integrals and, last but not least, the angular distributions through the angle φ.

The notation of the matrix element integrals $D^{\pi/\sigma(2)}_{n_1,|m|}$, characterizes the two-photon pathway. The superscripts π or σ denote the polarization of the second absorbed photon, responsible for the transition to the final m-state out of the virtual one of given $|M|$ (=0 or 1). The possible excitation pathways may be visualized in Figure 14.

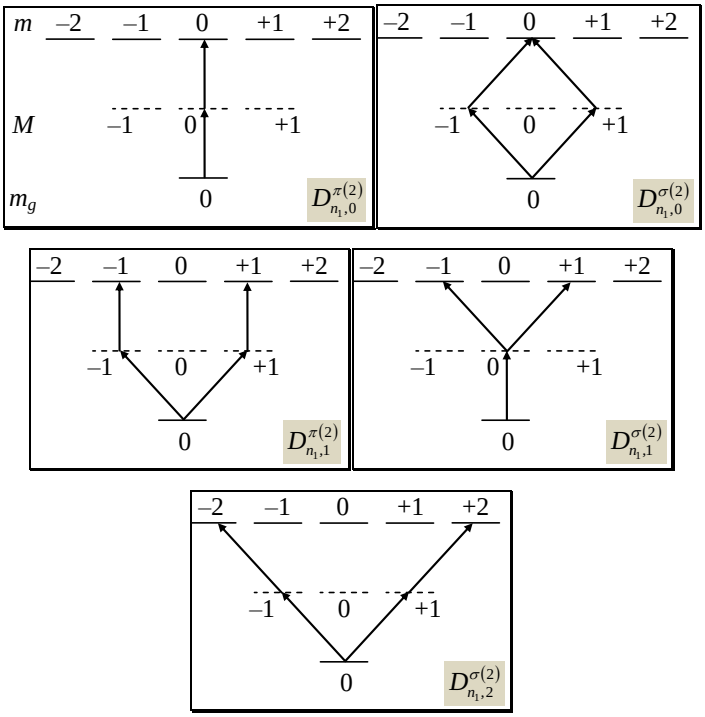

Figure 14. The two-photon pathways schematically. According to the radiation polarization (π or σ) the final m-state is excited out of the virtual state of an azimuthal quantum number M. We solely consider the m_g=0 ground state as our initial state.

Photoionization microscopy images $\propto \mathrm{J}_{v_{\mathrm{det}}}(\chi,\varphi)$, present a complicated distribution because a different radial fringe system is formed for each angle φ (e.g. $\mathrm{J}_{v_{\mathrm{det}}}(\chi,\varphi=0)$ may present a different behavior than $\mathrm{J}_{v_{\mathrm{det}}}(\chi,\varphi=\pi/2)$). Moreover, the coherent superposition of different $|m|$-states in Eq. (89) gives rise to the so-called m-beating effect [30]. The latter is manifested in the form of intensity modulations along the φ coordinate. Interestingly, the expression providing the glory signal, which is defined in Eq. (72) and in which only m=0 states contribute, is quite simple,

$$\mathrm{J}_{v_{\mathrm{det}},\mathrm{Glory}} \propto \left|\sum_{n_1}\left(\cos^2\Theta\, D^{\pi(2)}_{n_1,0}+\frac{\sin^2\Theta}{2}D^{\sigma(2)}_{n_1,0}\right)A_{X,n_1,0}\, e^{i\theta^{*}_{n_1,0}}\right|^2 \tag{90}$$

and yet incorporates quite rich information.

Let us now extend the above modeling and consider a more general geometry, shown in Figure 15. The static field vector **F** points towards the positive z direction and the detection plane is set at z_{det}. This case corresponds to the propagation of a misaligned laser beam which no longer

propagates perpendicularly to the field. This misalignment is introduced by the additional angle Φ, which is defined as the angle between the laser beam propagation vector and the *x* axis. The angle Θ is now formed between the polarization vector and the horizontal *z*-*x* plane. In other words, as compared to Figure 13 (Φ=0), the *z* and *x* axes of the misaligned geometry have been rotated by an angle Φ with respect to the fixed *y* axis.

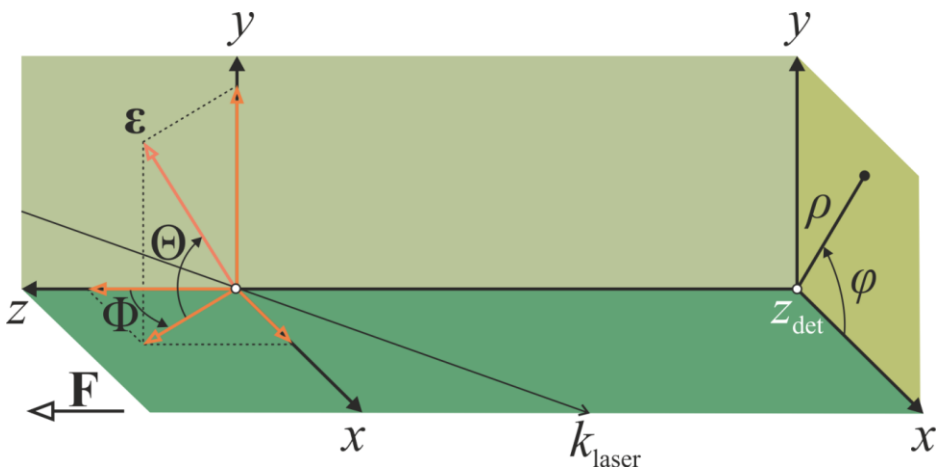

Figure 15. Same as Figure 13 but now the laser propagates in the $\hat{k}(\neq \hat{x})$ direction that lies within the *x*–*z* plane. The laser propagation vector and the *x* axis form the Φ angle. It is advantageous to separate the polarization vector into two components, one parallel and one perpendicular to the *z* axis. The polarization vector **ε** has a *z* component of ε·cosΘ·cosΦ. The *y* and *x* components are combined to form a new *y*′ axis which is normal to the *z* axis. The angle *ϑ* between *y* and *y*′ axes depends on Θ and Φ (see main text).

The transition operator now writes, $\hat{\mathrm{T}} = \cos\Theta\cos\Phi z + \sin\Theta y + \cos\Theta\sin\Phi x$. Following the steps that were described before, the electron current density $\mathrm{J}_{v_{\mathrm{det}}}$ is written in the form of Eq. (89) with the substitutions Θ→Θ′ and $\varphi \rightarrow \varphi' = \varphi - \vartheta$ where the angle Θ′ is defined through the expression,

$$\cos\Theta' = \cos\Theta \cdot \cos\Phi \tag{91}$$

and the angle *ϑ* is defined as,

$$\tan\vartheta = \frac{\sin\Phi}{\tan\Theta}\,. \tag{92}$$

This implies that the detection reference frame has been rotated for an angle *ϑ* which varies with Θ. However, apart from these substitutions, all expressions (such as Eq. (89) and Eq. (90)) keep

their prior form. The above relations and angular variable substitutions are justified because the selection rules are sensitive solely to whether the polarization vector is parallel or perpendicular to the static field axis. For the alternative simpler geometry where the polarization vector lies in the y'–z plane where the y and x axes have been rotated by an angle θ with respect to the fixed z axis, it holds that the detection reference frame has been rotated by a constant angle θ. The single-photon transition operator may again be kept in the form Eq. (86) after the sole substitution is $\varphi \rightarrow \varphi' = \varphi - \theta$.

Let us also introduce the first moment of the electron current density distribution i.e. the barycenter of the image intensity which is defined as,

$$\mathbf{C}_{\mathrm{B}} = \frac{1}{\sigma_{\mathrm{tot}}} \iint \mathrm{J}_{v_{\mathrm{det}}} \boldsymbol{\rho} dS = C_{\mathrm{B}}^{x} \mathbf{x} + C_{\mathrm{B}}^{y} \mathbf{y} \,. \tag{93}$$

where, as it turns out,

$$C_{\mathrm{B}}^{x} = c_{\mathrm{o}} \cos^2\Theta \cos\Phi \sin\Phi (\cos^2\Theta \cos^2\Phi + c_1) \tag{94}$$

and

$$C_{\mathrm{B}}^{y} = c_{\mathrm{o}} \cos\Theta \sin\Theta \cos\Phi (\cos^2\Theta \cos^2\Phi + c_1) \,. \tag{95}$$

The constants c_{o}, c_1 are integrals that depend on the matrix elements, the wave functions $X_{n_1,|m|}$ and the phases $e^{i\theta^{*}_{n_1,|m|}}$. Note that for a given Φ, C_{B}^{x} and C_{B}^{y} are symmetric and antisymmetric with respect to $\Theta = \pi/2$, respectively. Interestingly, the ratio of the two barycenter coordinates reproduces Eq.(92),

$$\frac{C_{\mathrm{B}}^{x}}{C_{\mathrm{B}}^{y}} = \frac{\sin\Phi}{\tan\Theta} = \tan\vartheta \,. \tag{96}$$

As shown above the barycenter of a PM image monitors the linear polarization vector orientation in all possible misalignments and system rotation geometries. This seems to be expected also for different excitation schemes (single-photon excitation etc.). Here, the barycenter position of two-photon PM images is presented in a compact form and allows for correcting misalignments with respect to the static electric field. In addition, this is an experimentally easy to extract quantity that doesn't require any particular spatial resolution and is insensitive to small defects in the detector's efficiency.

1.3.2 *m*-Decomposition of Total Cross Section

The electron current density of Eq. (89) refers to the two-photon ionization of hydrogenic final Stark states out of an m=0 initial state. Plugging this equation to see Eq. (69) leads to the two-photon total excitation hydrogenic cross section which then writes,

$$\sigma_{\mathrm{tot}}^{(2)} \propto \sum_{n_1} \left\{ \begin{array}{c} \left(\cos^2\Theta\, D_{n_1,0}^{\pi(2)} + \frac{\sin^2\Theta}{2} D_{n_1,0}^{\sigma(2)} \right)^2 \\ + \frac{\cos^2\Theta \sin^2\Theta}{2} \left(D_{n_1,1}^{\pi(2)} + D_{n_1,1}^{\sigma(2)} \right)^2 \\ + \frac{\sin^4\Theta}{8} \left(D_{n_1,2}^{\sigma(2)} \right)^2 \end{array} \right\}. \tag{97}$$

This incoherent sum of the different-$|m|$ cross sections presents an interesting dependence on Θ, in contrast to the field-free case. In the latter case, the quantization axis is always parallel to the rotating linear polarization and that polarization rotation has zero effect to the total cross section [43,48,89]. As an example, Figure 16 shows the hypothetical case of equal matrix elements i.e. $D_{n_1,|m|}^{(2)} \equiv 1$ and single n_1 excitation. The $|m|$=1 character is obviously present for $\Theta \neq 0, \pi$, while the $|m|$=2 character is present for $\Theta \neq 0$ and exhibits a maximum for $\Theta = \pi$. Note, that in the presence of misalignments discussed in the previous subsection, the total cross section formula of Eq. (97) still holds, but with the substitution $\Theta \rightarrow \Theta'$ according to Eq. (91).

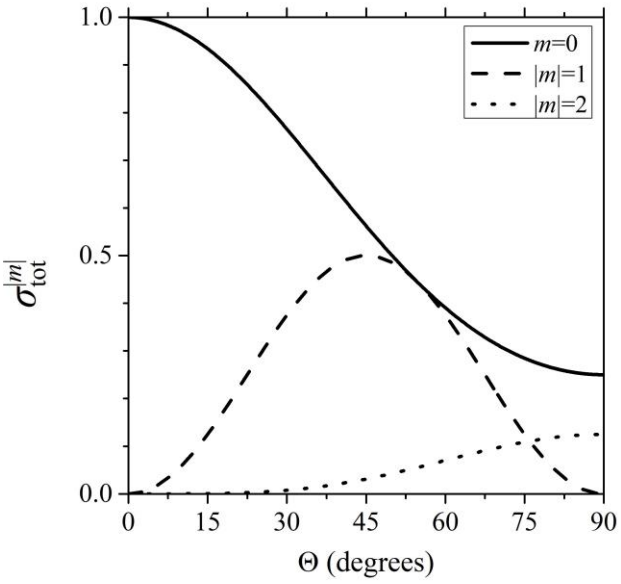

Figure 16. The three different *m*-components of the two-photon total cross section ($\sigma_{tot}^{(2)}$) as functions of Θ. Here we have made the substitutions $D_{n_1,|m|}^{(2)} \equiv 1$ and we have ignored the summation over multiple n_1. The |*m*|=1and 2 excitations exhibit maxima for Θ=45° and 90° respectively. On the other hand, the behavior of *m*=0 depends strongly on the value of $D_{n_1,0}^{(2)}$'s.

Let us now treat the same two-photon excitation scenario out of the ground state of a multielectron atom, by making use of the LFT theory [32]. The zero-field final and initial states are $\psi_f = r^{-1}P_{l_f}Y_{l_f}^{m_f}$ and $\psi_g = r^{-1}P_g Y_0^0$ respectively. The two-photon spherical matrix elements write

$$d_l^{m(2)} = \langle \psi_f | \hat{\mathrm{T}}^{(2)} | \psi_i \rangle = \langle \psi_f | \hat{\mathrm{T}} | \psi_{\mathrm{v}} \rangle \tag{98}$$

where the single-photon transition operator is defined as in Eq. (86) and the virtual state obeys the following Dalgarno-Lewis equation [82,83],

$$\left[-\frac{1}{2}\nabla^2 + U(\mathbf{a}; r) - E_{\mathrm{v}} \right] \psi_{\mathrm{v}} = -\hat{\mathrm{T}}\, \psi_g \,, \tag{99}$$

with $E_{\mathrm{v}}=(E+E_g)/2$ (strictly speaking, for *E* lower than the ionization potential the energy should correspond to a bound atomic *p*-state). The solution of the above equation is written as,

$$\psi_{\mathrm{v}} = r^{-1}\tilde{P}_{1_{\mathrm{v}}} \left[\frac{1}{\sqrt{3}} \cos\Theta\, Y_1^0 + \frac{i}{\sqrt{6}} \sin\Theta\, (Y_1^1 + Y_1^{-1}) \right] \tag{100}$$

where $\tilde{P}_{1_v}$ is the radial part of the virtual state, which depends on the atom-specific $U(\mathbf{a};r)$ but it does not depend on the angular factors. Plugging the virtual state of Eq. (100) into the spherical matrix elements of Eq. (98) and using the Stark multi-electron matrix elements of Eq. (81) we finally arrive at,

$$\sigma_{\mathrm{tot}}^{(2)}(\Theta) \propto \Lambda^2 \Delta_{00}^0 + \Lambda \frac{2}{\sqrt{5}}(3\cos^2\Theta - 1)\Delta_{02}^0 + \frac{1}{5}(3\cos^2\Theta - 1)^2 \Delta_{22}^0 + \frac{12}{5}\cos^2\Theta \sin^2\Theta\, \Delta_{22}^1 + \frac{3}{5}\sin^4\Theta\, \Delta_{22}^2 \,. \quad (101)$$

where the dimensionless parameter,

$$\Lambda = \frac{\int_0^\infty P_{0_f}\, r\, \tilde{P}_{1_v} dr}{\int_0^\infty P_{2_f}\, r\, \tilde{P}_{1_v} dr} \,. \quad (102)$$

measures the relative strength of the radial matrix elements corresponding to the transitions $p \rightarrow s$ and $p \rightarrow d$, respectively. As for the quantities $\Delta_{l,l'}^{|m|}$, they are given by,

$$\Delta_{l,l'}^{|m|} = \sum_{n_1} \mathrm{Re}\left[\alpha_{n_1}^{l,|m|} \left(\alpha_{n_1}^{l',|m|}\right)^*\right] . \quad (103)$$

with the factors $\alpha_{n_1}^{l,|m|}$ defined as,

$$\alpha_{n_1}^{l,|m|} = \sum_{n_1} \left\{ W_{l,n_1'}^{|m|} B_{n_1',n_1}^{|m|} \right\} . \quad (104)$$

The quantities $\Delta_{l,l'}^{|m|}$ carry much of the information about the Stark structure and were named after Harmin as the non-hydrogenic "density of states" in the presence of a static field [92]. Further, it is interesting to note in Eq. (101), that there are terms depending on the angular factor $(3\cos^2\Theta - 1)$. These terms are eliminated when $\cos^2\Theta_{\mathrm{magic}} = 1/3$, i.e. at the so-called "magic angle" Θ_{magic}=54.7°. Furthermore, as a rule of thumb the $p \rightarrow s$ radial matrix elements are much weaker than the $p \rightarrow d$ ones [87]. In fact, experimental results for Mg [93] showed that this is indeed the case and provided an estimate for Λ<0.1. Then, the term in Eq. (101) which is proportional to Λ^2 can be safely neglected and, to a first approximation, the same holds also for the term proportional to Λ. Under these approximations, the total cross section simplifies to,

$$\sigma_{\mathrm{tot}}^{(2)}(\Theta, E) \propto \frac{1}{5}(3\cos^2\Theta - 1)^2 \Delta_{22}^0(E) + \frac{12}{5}\cos^2\Theta \sin^2\Theta\, \Delta_{22}^1(E) + \frac{3}{5}\sin^4\Theta\, \Delta_{22}^2(E) \quad (105)$$

and the three |m|-spectra $\Delta_{22}^{0}(E)$, $\Delta_{22}^{1}(E)$ and $\Delta_{22}^{2}(E)$ can be determined by measuring $\sigma_{\mathrm{tot}}^{(2)}(\Theta, E)$ for three values of Θ (that can conveniently be Θ=0°, Θ_{magic} and 90°). Finally, the validity of the approximation made on Λ can be examined by employing the determined functions $\Delta_{22}^{0}(E)$, $\Delta_{22}^{1}(E)$ and $\Delta_{22}^{2}(E)$ in order to compute "synthetic spectra" at different angles Θ and compare with their experimental counterparts. This procedure is applied to our analysis presented in the third Chapter.

Chapter 2: Experimental Setup & Procedure

2.1 Experimental Setup

2.1.1 General Description of the Experimental Setup

A full schematic view of the experimental set-up is given in Figure 17. We provide here a general overview while each individual subsystem will be subsequently presented in more detail. The excitation and ionization of magnesium atoms is accomplished by a commercial dye laser system (Lambda Physik ScanMate 2EC-400). The dye laser is pumped by the frequency doubled (532 nm) radiation of a neodymium-doped yttrium aluminum garnet – $Y_3Al_5O_{12}$ – (Nd:YAG)

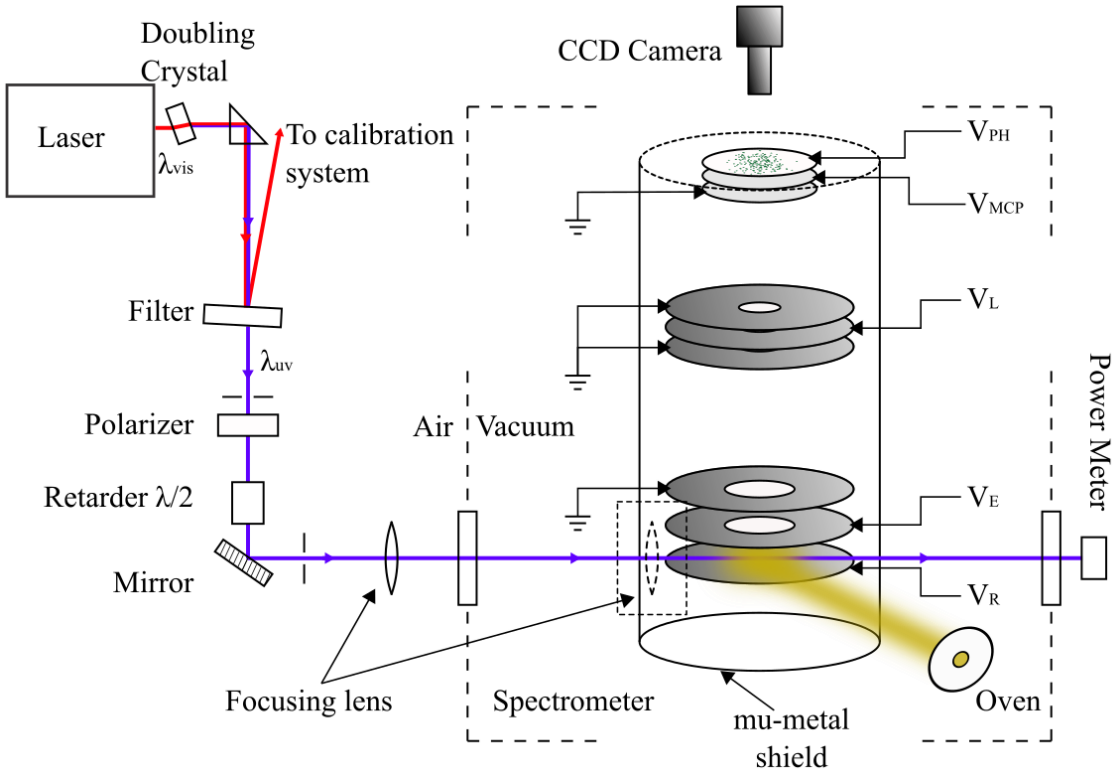

Figure 17. Schematic representation of the experimental setup (not to scale). The fundamental and the ultraviolet beams are denoted with red and purple color respectively. The optics for guiding the beams and manipulating the polarization are shown, namely the right-angle prisms, filter (UG5), polarizer, λ/2 retarder, mirror and lens. The pulse energy is monitored after the exit window. The focusing lens is positioned either in front of the spectrometer's entrance window or in-vacuum, in between the mu-metal shield and the

electrodes (enclosed within the dashed rectangle). Mg vapor atoms interact with the uv beam in the interaction region. The spectrometer exhibits a typical three-electrode VMI geometry, with the addition of an Einzel lens and a detector placed at the end of the field free tube. A CCD camera captures the bright spots on the phosphor screen.

pulsed laser operating at 10 Hz and delivers fundamental-radiation pulses in the 610–670 nm spectral range. This visible dye laser output is frequency-doubled by a potassium dihydrogen phosphate (KDP) crystal and the resulting ultraviolet (UV) radiation pulses (305–335 nm) are linearly polarized, they have ∼5 ns duration, ∼1 mJ maximum pulse energy and an estimated spectral width of ∼0.4 cm^{-1}.

The two beams (fundamental and frequency-doubled) are separated by a bandpass filter (UG5) placed almost perpendicularly to the propagating beams. The reflected visible radiation is guided towards a wavelength calibration system consisting of a Fabry-Perot interferometer of well-known free spectral range (FSR) that provides relative energy calibration and a discharge lamp offering absolute calibration via the optogalvanic effect. The transmitted UV beam is guided towards the experiment. It first passes through an alpha barium-borate (alpha-BBO) Rochon prism linear polarizer and a double-Fresnel rhomb (acting as an achromatic λ/2 retarder) for purifying and rotating its linear polarization, respectively. Subsequently, it is focused to a vacuum chamber either via an f∼20 cm focal length lens or an in-vacuum f∼5 cm lens. The laser beam enters and exits from the chamber through UV-grade fused silica flat windows of 2 mm width.

Magnesium vapor is produced in a water-cooled and electrically heated stainless-steel oven reaching a maximum temperature of ∼1100 K. The oven is mounted at the top of the vacuum chamber which is separated from the interaction chamber by a 1 mm hole. The achieved background pressure with the oven turned off is $\sim 7\times10^{-7}$ mbar. On the other hand, when the oven is turned on the pressure in the laser-atom interaction region (LAIR) is found to be $\sim 10^{-6}$ mbar. The thermal beam consists of ground-state Mg atoms, which interact with the focused laser beam inside an electron spectrometer and in the presence of a static electric field. The laser propagation, atomic beam and spectrometer (electric field) axes are perpendicular to each other. The final $3sEk$ Stark states of Mg atom (with Ek denoting the $|k\rangle$ Rydberg electron Stark state excited at energy E), are two-photon excited out of the $3s^2\ {}^1S_0$ ground state with no near-resonant single-photon intermediate levels. The UV two-photon excitation scheme leads to an expected overall spectral width of about ∼0.8 cm^{-1}. For π-polarization, i.e. linear laser polarization along the direction of

the static electric field, solely $m = 0$ final states are excited. For σ-polarization, i.e. for laser polarization normal to the field, the selection rule $|\Delta m|=1$ per photon applies and we excite final states of both $|m|=0, 2$ [27,70].

The electron spectrometer geometry is based on a standard three-electrode velocity-map imaging (VMI) spectrometer design [94]. The LAIR lies between the first two electrodes, i.e. a solid repeller plate and an extractor plate with a hole in its center. These electrodes are biased at voltages V_R and V_E, respectively. The following grounded third electrode is identical to the extractor plate. The holes of the last two electrodes create an inhomogeneous electric field necessary for the spectrometer to meet the VMI focusing conditions for a given V_E/V_R ratio [94,95]. Nevertheless, in the limited laser-atom interaction volume, the field may be considered as nearly constant within ±0.1% but its actual value is rather difficult to estimate accurately based on the applied voltage values. More accurate and self-consistent field estimations are obtained via the experimental measurements through procedures that will be exposed in detail in the discussion Chapter.

Photoelectrons are accelerated by the field towards the end of a field-free drift tube. An electrostatic magnifying Einzel lens is placed about midway the tube [95,96,97]. The lens consists of three identical and equally-spaced electrodes with holes at their centers. The two outer electrodes are grounded, while the middle one is biased to a voltage V_L (typically the lens operates in deceleration mode and, therefore, for electrons $V_L <0$).

At the end of the tube, the electrons are detected by a two-dimensional position-sensitive detector (PSD) consisting of a tandem microchannel plate assembly followed by a phosphor screen/anode. A CCD camera records the two-dimensional (2D) distribution of light spots on the phosphor screen. Recorded images are transferred to a computer, where they are accumulated over several-thousand laser shots. The entire spectrometer is shielded by a double mu-metal (nickel–iron ferromagnetic alloy) layer, while special attention has been given to the shielding of the vicinity of LAIR. These precautions are estimated to result to a residual magnetic field <1 μT in its interior, which is considered as low enough for our purposes.

2.2 Instrumentation: Detailed Description

2.2.1 Dye Laser System

Coherent radiation pulses are delivered by the Lambda Physik ScanMate 2EC-400 dye laser pumped by a Q-switched Nd:YAG laser (Quantel-BrilliantB LPY-400). For the latter, pumping of the active medium (YAG rod) is accomplished by two intracavity flashlamps which are triggered by a high–voltage pulse. After a certain time delay from that pulse -and within the duration of the medium fluorescence- another electrical Q-switching pulse is applied to an intracavity Pockels cell [98,99] allowing for the production of a 1064 nm laser output pulse of 5-6 ns temporal width. The laser operates at 10 Hz while its pulse energy may be varied by adjusting the aforementioned flashlamp/Q-switch time delay ($\Delta t \sim 280$-370 μs). Moreover, a TTL (+5 V, 25 μs duration) replica of the Q-switch pulse (synchronous to the light pulses) is available via an output BNC connector located at its Power Supply and it is used for synchronization purposes, i.e. as the "clock" of our experiment.

The Nd:YAG laser infrared pulses are frequency-doubled by a highly deuterated Potassium Dihydrogen Phosphate DKDP crystal (Second Harmonic Generation module [98]). The resulting doubled 532 nm radiation is employed for pumping the dye laser, a schematic diagram of which is given in Figure 18. The wavelength band of operation of the dye laser is chosen by selecting the appropriate active medium (dye and solvent) [100]. In our experiment we were interested in producing pulses in the 610–670 nm spectral range and we used the dye DCM (4-Dicyanmethylene-2-methyl-6-(p-dimethylaminostyryl)-4H-pyran) diluted to methanol. The 532 radiation is distributed to two active medium cells (cuvettes) via appropriate beamsplitters and dichroic mirrors. The dye solution flows in these two cells, namely the oscillator and pre-Amplifier cell (PreAmp-cell) and the Amplifier cell (Amp-cell). Typical concentrations of the dye solution are: (i) 0.15 gr/L in 300 mL methanol for the PreAmp-cell and (ii) 0.05 gr/L in 900 mL methanol for the Amp-cell.

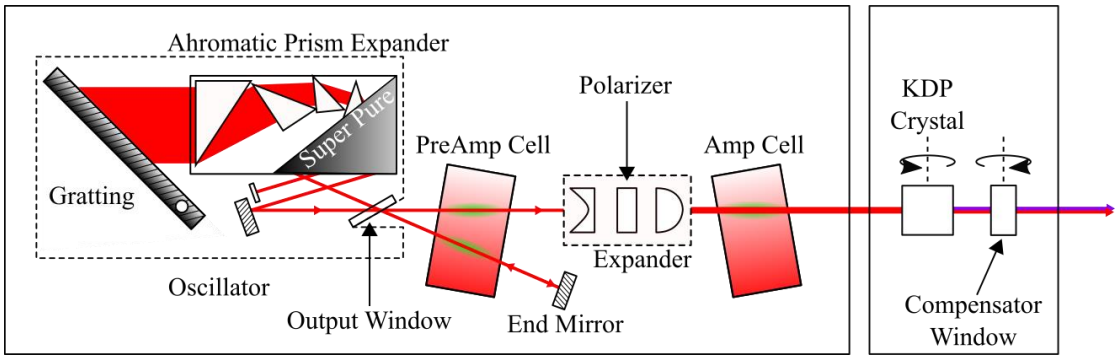

Figure 18. Schematic representation of the Lambda Physik dye laser. The SCANMATE oscillator components are: the end mirror, the PreAmp-cell (containing the active medium) and the encircled within the dashed box elements [98]. The prism expander system consists of several prisms that achieve the illumination of the whole grating and simultaneous outcoupling the output beam. The pumping radiation is focused by cylindrical lenses on the cells (green regions). The radiation is amplified in the PreAmp-cell, expanded and re-Amplified in the Amp-cell. Second harmonic generation is achieved by a KDP doubling crystal.

Apart from the PreAmp-cell, the SCANMATE *oscillator* consists mainly [98] of a grating for wavelength selection placed in the retroreflective, Littrow, position, an achromatic prism beam expander system necessary for increasing the number of illuminated lines on the grating and narrowing the laser line spectral width and an appropriately coated highly reflective end mirror. By coupling out the light after it has been filtered by the grating and before it passes through the active medium again, this particular outcoupling scheme (Lambda Super Pure®) eliminates a great part of the broadband amplified spontaneous emission (ASE) [98,101].

Under usual pumping conditions the out-coupled coherent oscillator radiation has pulse energy of about 100 μJ and is polarized perpendicularly to the grating groove orientation (i.e. it is vertically polarized with respect to the horizontal optical table plane).

The PreAmp-cell is used both as part of the oscillator and as a Pre-Amplifier simply by pumping the cell in a different region. This leads to pulses of ~1 mJ pulse energy. Subsequently, for further elimination of the un-polarized ASE (Amplified Spontaneous Emission) parasitic radiation, the beam passes through a linear polarizer and it is coupled in size to the Amp-cell via a two-lens beam expander before it is further amplified in the Amp cell. The final output pulse has ~5 ns duration, ~10 mJ energy and a diameter of ~3 mm (its repetition rate, is, of course, determined by the 10 Hz rate of the Nd:YAG laser). Finally, a 0.2 cm^{-1} spectral width has been estimated as explained in the next “Laser Frequency Calibration System” subsection.

The fundamental dye laser beam passes through a potassium dihydrogen phosphate (KDP) crystal and it is frequency doubled (305–335 nm). The crystal is mounted on a rotation stage that is controlled by the SCANMATE software. Pulse energy maximization (via phase matching [102]) is achieved by the proper rotation of the crystal for a number of selected wavelengths. Lateral beam displacement is eliminated by the simultaneous rotation of a compensator window in the opposite direction. The UV pulses have <5 ns duration, a maximum pulse energy of ~1 mJ and an estimated spectral width of ~0.4 cm^{-1}.

The overall laser performance is found to depend on the good condition of the cuvettes that should be frequently checked for damages which are almost invisible. Moreover, the Second Harmonic Generation (SHG) setup was also frequently checked because it is not thermally isolated and consequently the UV-output could vary with time due to non-constant thermal conditions affecting the phase matching optimization.

2.2.2 Laser Frequency Calibration System

After the beam (fundamental and frequency-doubled) separation by the filter (UG5) the reflected visible radiation is guided toward the wavelength calibration system, shown in Figure 19. A part of the visible radiation enters a discharge lamp (Ne buffer gas) and the remaining radiation passes through an Fabry-Perot interferometer, placed perpendicular to the incident beam. Finally, a photodiode records the transmitted light signal which is guided towards the boxcar together with the optogalvanic element (OGE) signal.

The optogalvanic effect refers to the voltage changes, typically observed in gaseous discharge lamps, followed after the irradiation of the buffer gas [103]. These changes correspond to electronic transitions for species in the discharge thus provide a one to one correspondence between the radiation wavelength and the energy levels difference. In our case, the discharge lamp voltage is either enhanced or decreased when our visible beam color matches an Ne electronic transition which is identified in the catalog of Ref. [104] and thus provides absolute energy calibration of the radiation wavelength. For example, a frequently used Ne line observed for $\lambda \approx 650.65$ nm corresponds to the transition $[He]2s^2 3p^5(^2P°_{3/2})3s\ ^2[3/2]°$, J=1 – $[He]2s^2 3p^5(^2P°_{3/2})3p\ ^2[5/2]°$, J=2 ($\lambda_v$=650.65281 nm).

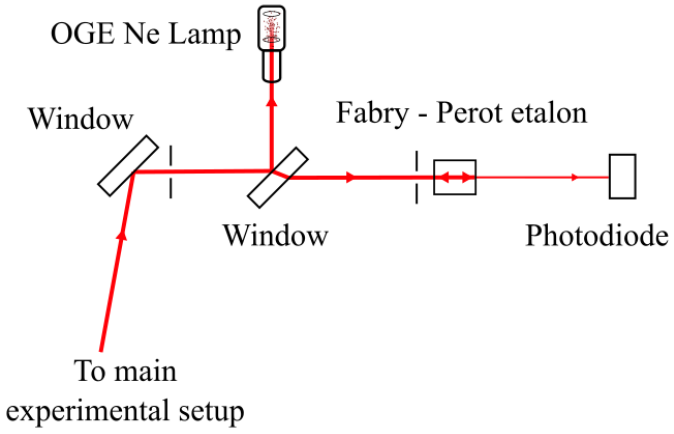

Figure 19. Schematic representation of the calibration experimental setup. The visible beam is guided towards the optogalvanic lamp and a Fabry-Perot interferometer. The Ne optogalvanic spectrum and the intensity modulation of the photodiode signal are recorded as the wavelength is scanned. Due to the high reflectivity of the interferometer surfaces only a small percentage of the beam is transmitted towards the photodiode.

Relative laser calibration is achieved with the use of a highly reflecting Fabry-Perot interferometer. The transmitted beam exhibits intensity maxima, as the radiation photon energy σ varies. Within the paraxial approximation, the photon energy σ values that correspond to maxima are predicted by,

$$\sigma = \frac{h_\sigma}{2L\, n_{\text{air}}(\sigma)\left[1-\frac{\theta_\pi^2}{2}\right]} \quad , \quad h_\sigma = 0.5,1.5,2.5,\ldots \tag{106}$$

where L is the distance between the interferometer windows in cm units, θ_π is the laser angle of incidence, σ is measured in cm^{-1} and h_σ a, typically large, half-integer that labels successive transmission intensity maxima. In practice, we ensure that the angle of incidence is almost zero (below 3 mrad) and employ the fact that the air wavelength n_{air} is slowly varying [105] for limited photon energy ranges. Then, the successive maxima are almost equidistant and equal to the free spectral range $\text{FSR} = \sigma(h_\sigma + 1) - \sigma(h_\sigma) \approx \frac{1}{2Ln_{\text{air}}(\sigma(h_\sigma))}$. Experimentally, we employ three neon OGE lines that lie near the energy range of interest (~15500 cm^{-1}) and have a maximum energy separation of ≈300 cm^{-1} (visible radiation). Then by scanning the laser wavelength and recording the OGE and the Fabry-Perot interferometer signal, the local FSR is calculated to be 0.4729(2)

cm^{-1}. Note that this value corresponds to an effective FSR of 1.8916(8) cm^{-1} for the final energy of the two-photon excitation of a system with the UV radiation. The intermediate energies are calculated by interpolation between maxima.

In conclusion, the calibration system provides the wavelength estimation within the accuracy of ~0.4 cm^{-1} in the final energy which is more accurate than the wavelength calibration offered by the laser system itself (accuracy of ~2 cm^{-1} in the final energy).

The interferometer transmitted intensity signal also provides an estimation of the laser spectral width. Indeed, the maxima profiles and width depend on the spectral width in addition to the intrinsic interferometer characteristics that define the finesse [99]. Assuming that our interferometer has infinite finesse and for a purely monochromatic radiation the intensity maxima should have a Dirac comb intensity distribution as the energy is scanned. In this case, the maxima spectral width is solely attributed to the laser beam spectral context. On the other hand, in the more realistic non-infinite finesse case, maxima spectral width provides an estimated upper limit for the laser spectral width, which for the used dye lase is found to be ≈0.2 cm^{-1} for the visible radiation.

2.2.3 Velocity Map Imaging Spectrometer (Photoionization Microscope)

The study of atomic/molecular systems has been revolutionized by the emergence of imaging techniques [106] that can provide a more complete set of observables than the previously used techniques. Imaging refers to the measurement of the position of a particular product created after the process under study. The apparatus which is typically used, namely the Velocity Map Imaging Spectrometer (VMIS) [94] presents several advantages to previous imaging setups [107,108]. The ejected species after the photoionization, photodissociation etc. process will impact a position sensitive detector (PSD) at the point (ρ,φ) while ρ is given by the simple formula,

$$\rho \propto \sqrt{\frac{T}{q\, V_R}} \tag{107}$$

where V_R the voltage of the first electrode T is the initial kinetic energy and q is the particle charge. In the case of photoionization, the electronic 3-dimensional velocity distribution is extracted by the 2-dimensional intensity distribution (transverse momentum) on the PSD by several techniques [48,109,110,111]. For the low electron kinetic energies employed in this study,

the observed quantity is proportional to the transverse momentum with respect to the spectrometer's axis [53] but the formula of Eq. (83) no longer applies due to the strong Coulomb effect on the electron trajectory. Thus, the use of the aforementioned techniques in the search of the initial 3D velocity distribution is limited.

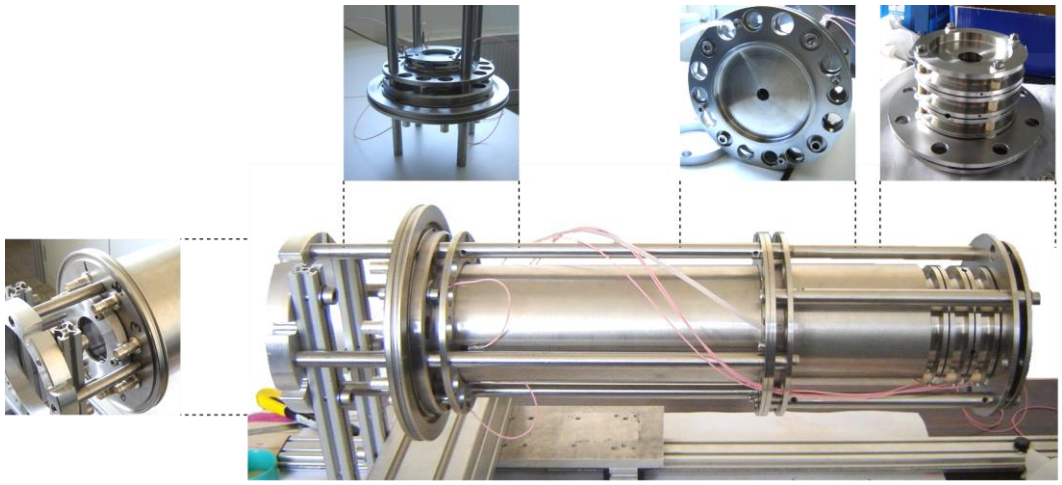

Figure 20. Velocity map imaging spectrometer capture. The inner mu-metal foils are shown but the outer shield is not yet plugged in. A vacuum flange holds the VMIS on stainless steel rods. Voltages are applied with cables that are connected to Safe High Voltage feedthroughs on the flange. Separate parts of the VMIS are also shown from left to right: (i) The flange with the window and the connectors as vied from the outer side. (ii) Same VMIS part captured from the interior side. The mounted detector and its connections are visible. (iii) Einzel lens electrodes. Inspecting the aperture reveals the other two electrodes (iv) Three electrodes setup, separated by ceramic cylinders. Small holes are formed between the first and second electrodes to facilitate the laser and/or atomic beam insertion into the center of the spectrometer.

In our study we employ a VMIS in its original variant [94] with the addition of an electrostatic Einzel lens for image magnification. This setup has been described in some detail in [22,27,95] and is shown in Figure 20.

Let us first deal with the three-electrode structure comprising the laser-atom interaction region without considering the peculiarities introduced by the Einzel lens. It is reminded that the LAIR is located between the first two electrodes and is defined by the laser beam and the atomic beam cross section. The solid Repeller and the annular (the hole diameter is ~20 mm) Extractor and Ground electrodes are placed 19 mm apart from each other. Each electrode is biased at the constant voltages V_R, V_E and $V_G \equiv 0$ respectively with the use of a series of power supplies (Stanford Research Systems, PS350).

Figure 21(a) shows the equipotential curves formed by the electrode geometry. Under these conditions, the inhomogeneous electric field that acts as an electrostatic lens for the charged particles [95]. The curvature of the equipotential lines is determined by the applied voltages and more specifically by the ratio V_E/V_R and for some specific ratio, all charged particles

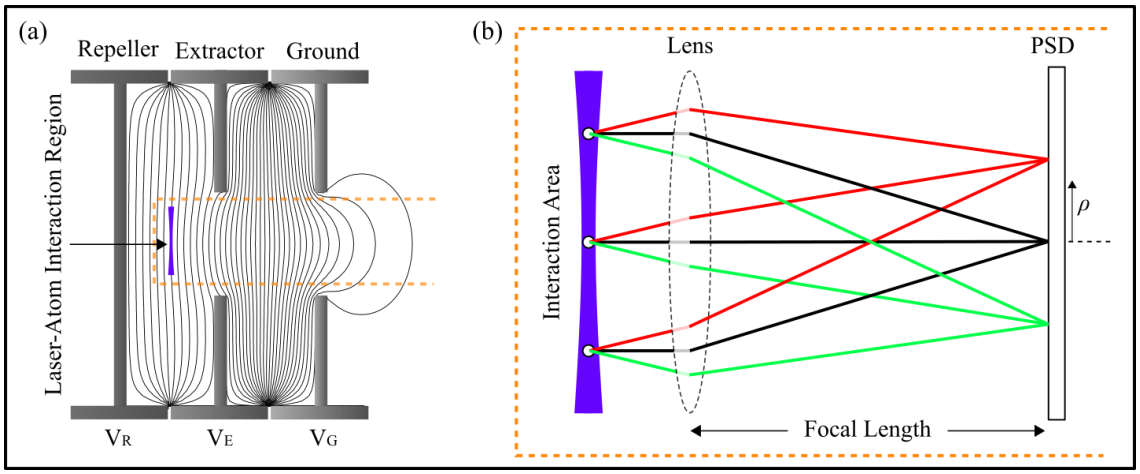

Figure 21. (a) Schematic three-electrode VMI setup similar to the used one. The equipotential curves form a lens and collimate particles of same velocity vector on the detector plane. (b) Optical analogue of the VMI operation. An ensemble of rays of three different inclinations with respect to the horizontal axis (spectrometer axis) and emitted from different initial points, is shown. The Fourier plane coincides with the detectors plane.

that have the same initial velocity vector will form a spot on the detector irrespective of their initial position. This ratio is defined by the electrodes geometrical characteristics and the length of the spectrometer and is referred as the VMI condition [95,112]. In addition, the VMI condition is altered by the LAIR displacement in the direction of the VMIS axis. In our setup $V_E/V_R \approx 0.68$. Using geometrical optics terminology, when the VMI condition is met, the focal length is exactly equal to the lens-detector distance. This operation is shown schematically in Figure 21(b) where, rays emitted from different locations of the LAIR zone but same orientation with respect to the VMIS optical axis, are collimated on the focal plane. Taking the optical analogy one step further, the detector plane intensity distribution (Image) is equal to the Fourier transform of the initial ejection position distribution [95].

We should note however that the above described VMI conditions derives from first order particle optics and it insufficient for compensating for extreme large LAIR extensions of very large

kinetic energy bandwidths. In any case the LAIR must be kept as small as possible (a task that will be addressed in the next subsection) and the VMI condition must be (experimentally) found in the energy range of interest. Note that the VMI conditions are independent of the particle mass and apply to both electrons or ions. Retaining the VMI condition but for increased field values (or equivalently for increased V_R values) the acquired image will be scaled down without any alteration of its characteristics. As we already mentioned the primary lens focal length depends on the applied voltage ratio V_E/V_R. When this ratio approaches unity the focal length becomes smaller than the interaction region distance from the center of the electrostatic lens. This operation mode is called spatial map imaging [106] and allows for the projection and magnification of the LAIR spatial profile on the detector [112].

Finally, the same spectrometer can be used for ToF measurements,

$$t \propto \sqrt{\frac{m}{q\,V_R}} \tag{108}$$

thus, allowing for atomic spectra acquisition or in related applications e.g. species distinction with gated detection [94].

One of PM's requirements is that the electron excitation energy is low enough so that the De Broglie wavelength, the moment of its liberation, is compatible with the spatial resolution of the spectrometer (or microscope). This is typically achieved for reduced energies lower than unity (ε<1), or for energies less than 25 meV (when typical field values ~1000 V/cm are used). These so called almost "zero" energy electrons cannot be resolved in typical VMI setups and form a bright spot on the center of the detector. Figure 22(a,b) shows the effect of the Einzel lens magnification on our images. These slow photoelectron images correspond to photoelectrons of about ~43 meV above the zero-field ionization energy, that is for an excitation energy well above the requirements of PM.

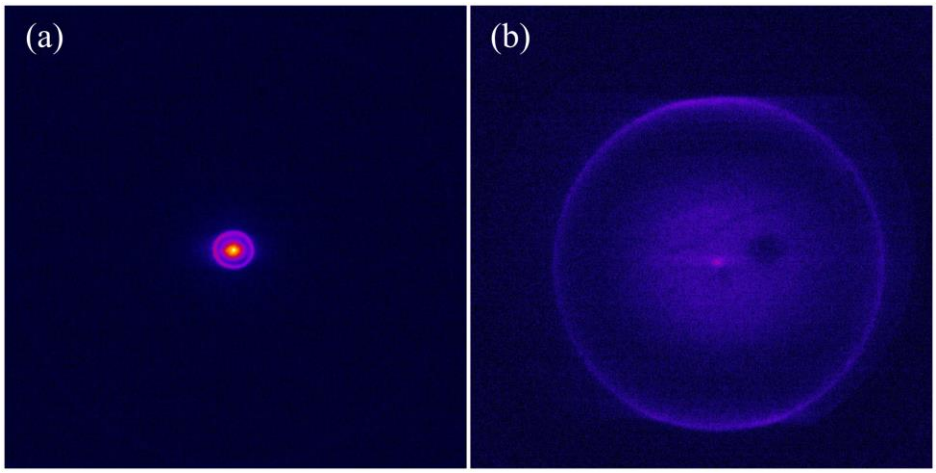

Figure 22. Slow photoelectron images after two-photon excitation out of the magnesium ground state. Images are presented in linear color-scale. For a fixed repeller voltage (V_R), we achieve VMI focusing conditions without (Figure 22(a)) and with the use of the Einzel lens (Figure 22(b)). The outer dimensions of our detector are visible on both images. The high excitation energy (~43 meV above the zero-field energy) does not allow for the observation of interference fringes.

The additional use of the Einzel lens, by applying appropriate voltages, can achieve up to a 20-fold magnification of the original image without introducing any severe errors [95].

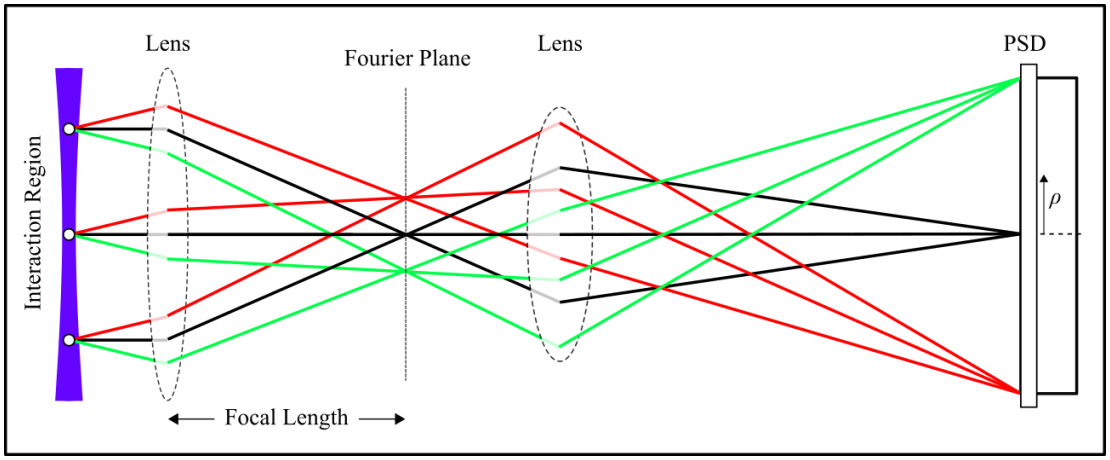

Figure 23. Optical analogue of the VMI spectrometer (as in Figure 21(b)) with the additional use of an Einzel lens. All rays of the same inclination with respect to the spectrometer axis are focused on the Fourier plane. This image is magnified by the "Einzel" lens and is projected on the detector plane. and imaged on the PSD detector.

This lens is located midway the field free space and consists of three identical annular electrodes (the hole diameter is 10 mm) that are placed 7.5 mm from each other and are biased to

voltages 0, V_L and 0 respectively. The preferable mode of operation is the decelerating mode meaning the polarity of V_L is the same as V_E and V_R thus, the electrons are first decelerated and then accelerated [95,96]. Then the VMI condition depends on both ratios V_E/V_R and V_L/V_R. In practice we first set V_L/V_R and then adjust V_E to ensure focusing on the detector plane. The typically employed ratio values are: $V_E/V_R \approx 0.73$ and $V_L/V_R \approx 1$. The optical analogue is shown in Figure 23. Note that, it is extremely important to properly align the first three electrodes and the Einzel lens electrodes because a small tilt leads to image formation away from the detectors center.

The entire VMIS is covered with two 1.5 mm mu-metal tubes in order to shield the interior from the Earth's or stray magnetic fields. An additional tube and a top hat of 3 layers (0.5 mm) of mu-metal foils were added to shield the upper part (near the LAIR) of the VMIS. All the mu-metal parts were treated in order to retain their magnetic properties by placing them near a radio frequency source and pulling them away while the source was operating.

2.2.4 Atomic beam & Pumping System

The oven system is located above the main experimental chamber. Magnesium chips (Aldrich 99.98%) are inserted inside the stainless-steel tube (see Figure 24) which is heated above the Mg melting point (580 – 600 ^oC). During the heating process, the Mg vapor exits the thin magnesium oxide (melting point of 2852 ^oC) coating that surrounds the chips which are collected at the bottom of the oven. Heating is achieved by induction via an external oven (0.3 kWatt, 7A max current) and the temperature is monitored externally by a thermocouple. The temperature indication is several degrees lower than the achieved maximum temperature inside the steel tube and is only used for reference purposes between experiments. An external closed water loop cools the system near the top and bottom flanges and the oven reaches thermal equilibrium without controlling the electric current through feedback loops. The cooling is efficient enough (<100 ^oC near the flanges), allowing for the use of fluoroelastomer (FPM/FKM) O-rings which are easier to install than copper ones. Generally, our oven produces a temporal stable thermal Mg atom flux for large timescales, while being simple in design as compared to other atomic sources [113].

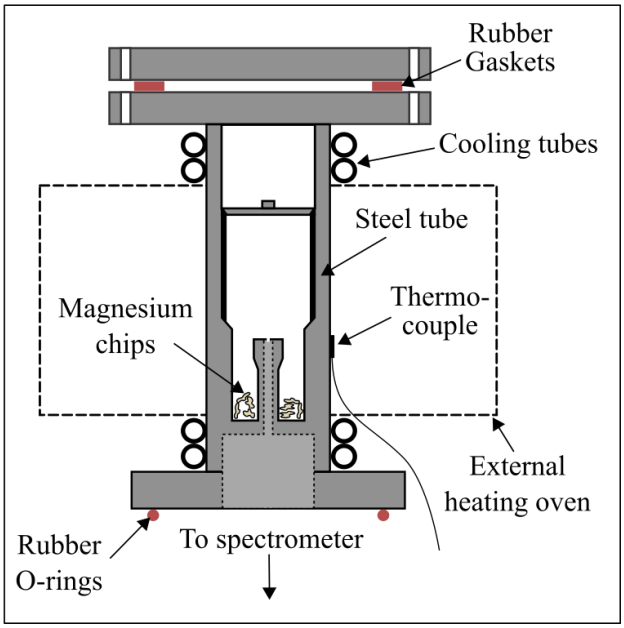

Figure 24. Schematic oven system. Magnesium chips are inserted at the bottom of a stainless-steel tube. The upper part of the tube is sealed with a flange, while the bottom part is connected to the spectrometer. High vacuum is achieved via rubber O-rings. The dimensions of the external oven are marked by the dashed line. A thermocouple measures the temperature at the outer side of the steed tube. The cooling tubes surround the tube near the flanges and are connected to an external water loop.

Magnesium vapor enters the main experiment chamber that hosts the electron spectrometer through an 1mm hole and forms a thermal beam that propagates downward. The atom velocity distribution follows the cosine law [113] and this leads to an enlarged cross section with the laser beam. This is apparent in Figure 25, where VMI images of the Mg^+ velocity distribution exhibits a class of homogenous velocity orientation overlaid to a downstream velocity class. The former is attributed to the formation of a local Mg vapor cloud inside the spectrometer that is responsible for defects in our images. Nevertheless, the low density of atoms in the LAIR does not produce any space charge effects. Different collimation techniques have been tried such as inserting plates with apertures just above the spectrometer or after the oven hole but were not used for our measurements due to the expense of extremely low flux in addition to the still poor collimation.

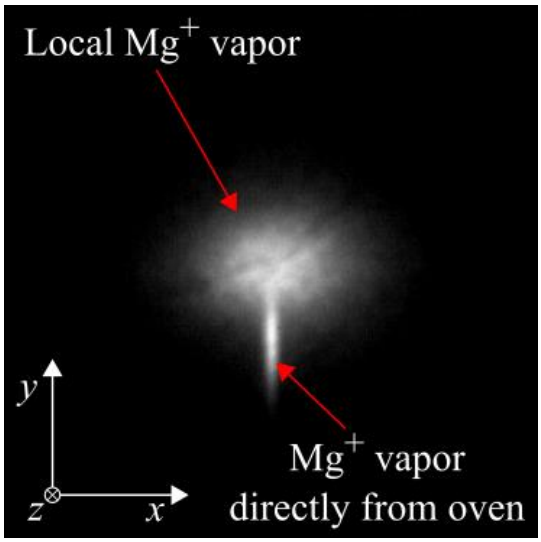

Figure 25. Experimental image of the velocity distribution of Mg^+ ions. The static field vector is parallel to the *z* axis. The oven system is located towards the positive *y* axis and provides the atomic beam. The laser beam propagates toward the positive *x* axis. The center of the detector coincides with the center of the presented image. Atoms that do not collide with any part of the spectrometer form a downstream velocity class. On the other hand, scattered atoms form a local atomic cloud that exhibits a uniform velocity orientation. Note that the velocity distribution is connected to the temperature via the Maxwell-Boltzmann relation [99], thus the atomic class that is not scattered exhibit a higher temperature that the scattered one.

The pumping system consists of a turbomolecular pump (Leybold Turbovac TW 250S) backed up by a rotary pump. Additional pumping is provided by a liquid-nitrogen cold trap placed on top of the turbo pump. We achieve high vacuum (O-rings seals) i.e. $\sim 5\times10^{-7}$ mbar when the oven is not operating and $\sim 2\times10^{-6}$ mbar when the oven is hot and Mg vapor is produced (experimental working conditions). The system is almost oil free (UV spectra with cold oven suggest the presence of oil species that are not detectable under working conditions) while a pneumatic valve (Leybold) has been placed in the turbo pump output to ensure good working conditions after sudden power breakdowns.

2.2.5 Detection & Data Acquisition Systems

The produced ions/electrons are detected with a 2-dimensional position sensitive detector placed at the end of the field free tube (electron spectrometer). The detector consists of an array of two Micro-Channel Plates (MCPs) followed by a phosphor screen/anode. The MCPs are made out of highly resistive material (~0.5 mm) with small apertures (channels) of ~10 μm in diameter, that

have some pitch angle (6–12 degrees). When an electron enters a channel, it strikes the wall thus multiple secondary electrons are produced. These electrons are accelerated by the applied voltage difference on the two faces of the plate and strike the opposite wall again producing further secondary electrons. The two 50 mm diameter, tandem (i.e. opposite pitch angle directions) MCPs plates (of either Hamamatsu, Tectra or Baspik suppliers) are placed in contact since they have the same resistance (resistance matched). The input side of the first plate is grounded and the output face of the second plate is set to some voltage (V_{MCP}, typically 1600 – 2000 V, Stanford Research Systems PS350), thus a uniform voltage gradient is applied to the MCP set and a gain of $\sim 10^6$ is finally achieved.

The screen/anode consists of a glass window coated with phosphor (the used phosphor type has moderately slow fluorescence lifetime e.g. P46 type) overlaid by a thin aluminum coating. Then the electrons produced by the MCPs are accelerated toward the screen. The anode coating is biased to a higher voltage, $V_{PH} - V_{MCP}$ ~400 V or ~2200 V, for ToF or imaging measurements respectively. The detector is shown in Figure 26.

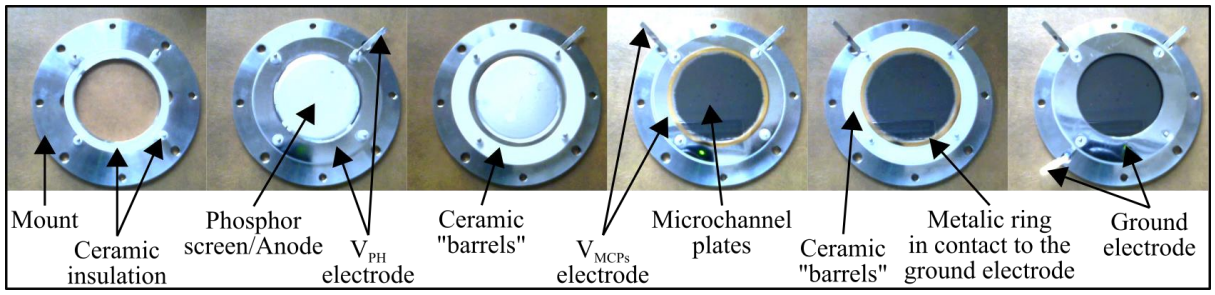

Figure 26. The figure shows the detector, captured at different stages of assembly, starting from left to right. The phosphor screen rests on the ceramic ring and is overlaid by its electrode. Note that the voltages are applied through the visible electrode pins. Four ceramic pillars and the ceramic "barrels" ensure that there is no electrical connection between the anode, the MCPs and the grounded electrodes. The last ground electrode is in contact to the front face of the MCPs. This detector has an effective area of ≈4.5 cm in diameter.

In the case of ToF measurements, a homemade decoupler module (E. Dimitriadis) is inserted on the anode supply line and is shown schematically in Figure 27. The capacitor decouples the electronic pulse signal from the high voltage dc offset and delivers the signal through a BNC connector cable towards an analog gated integrator (Stanford Research Systems SR250). Then the signal is integrated in the range of an adjustable time-window (gate) and exponentially averaged

over the selected number of shots. The output signal is a slow varying dc voltage that is fed to an oscilloscope and recorded by a homemade pc Labview program. The boxcar system is triggered by the YAG laser Q-switch TTL output pulse. Note that the cable internal resistances greatly affect the signal delivered by the decoupler. A visible ringing effect is observed in the ToF signal which is attributed to the poor cabling choice but this does not affect our spectra due to the proper gating on the signal maximum.

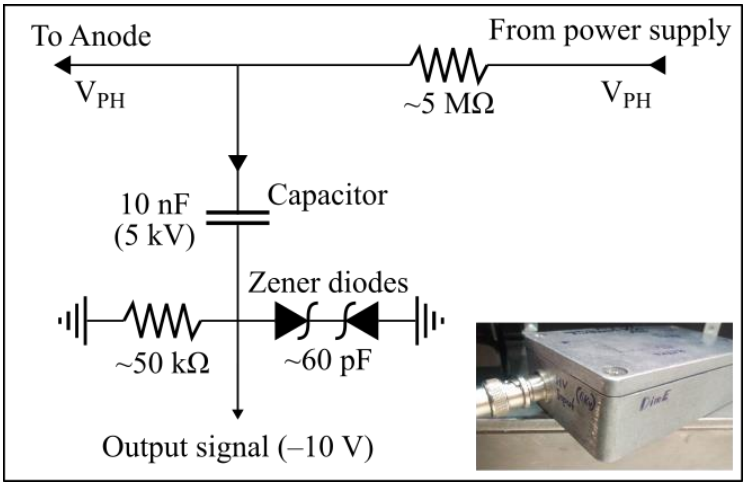

Figure 27. Here is shown decoupler module circuit that was used for ToF measurements. The anode is biased from the power supply through a large resistance for safety purposes. The connections are of safe-high-voltage type for the power supply input and the anode output and BNC type for the output signal. The capacitor separates the ~4 kV dc voltage from the electronic pulse signal which is guided towards an analog gated integrator. The Zener diodes ensure that the absolute value of the output signal is less than 15 V.

For imaging measurements, the aforementioned decoupler is removed and the anode voltage is inserted directly into the spectrometer (in principle the decoupler can be present even when high voltage ~5000 V is applied to the anode but is removed for safety purposes). The activated phosphor produces fluorescent bright spots that are recorded with a CCD camera and transferred to a pc via a firewire cable. We use a Black&White (Allied Vision Technologies, F-201B) camera equipped with a 1:2.8 zoom lens of maximum focal length of 50 mm (Tamron Japan, C200915). The camera is mounted on a x-y-z translation stage with rotation capabilities in the horizontal plane and is covered to minimize ambient light. Camera triggering is offered by a home-made delay module (E. Dimitriadis) that is triggered by the Q-switch pulse and produces a delayed pulse of adjustable width. This delayed pulse (delay~99.97 μs) opens the camera shutter and

controls the exposure time (exposure time~60 μs) thus recording the phosphor fluorescence of the subsequent laser pulse (10 Hz). The small pulse to pulse timing jitter is estimated to be of the order of a few ns, thus it is negligible for the typically used exposure time.

2.2.6 Data Acquisition & Analysis Software

SCANMATE: The dye laser is operated through the SCANMATE (Lambda Physik) program. The SHG crystal position must be calibrated before each experimental run by adjusting the crystal angle for four or five equidistant wavelength values within the selected wavelength range. By monitoring the SHG output intensity with a photodiode and controlling the crystal angle the UV pulse energy is optimized at each selected wavelength. Then the SHG module is calibrated and during a scan the computer interpolates the selected calibration points to rotate the crystal at the correct angle.

During the scan, the wavelength is tuned within the selected spectral range (Start, Stop) in selected increments (Step). After each wavelength increment the laser emits the selected number of pulses (Counts) and subsequently moves to the next wavelength. Lower step values (0.001 nm minimum) increase the resolution while higher count values (1000 maximum) improves the statistical confidence but both introduce a time toll (e.g. for a 2.5 nm scan with a 0.001 nm step and for 100 counts for each step a 7 hours scan is required).

Laser scan and data acquisition is asynchronous thus, it is important to be temporarily matched. The delay time between steps is almost negligible for small Step values (<0.1 s). However, this is not the case for the initial wavelength value (Start) where the grating and the crystal may need some time to move to the correct position. For this we employ the capabilities offered by the dye control system by selecting the initial grating position in order to correspond to the starting wavelength and then start the scan together with the data acquisition.

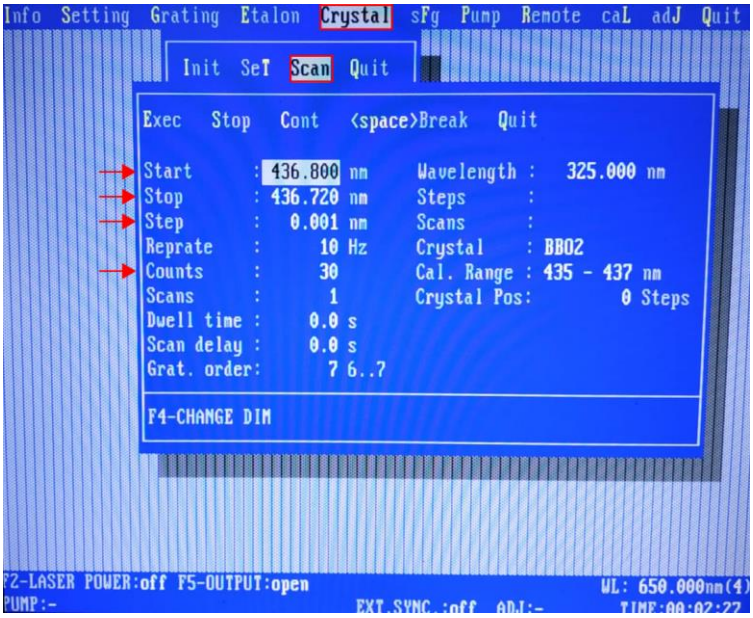

Figure 28. SCANMATE dialog window for scanning operation. The used doubling is of the KDP I type (Figure shows the BBO-2 type). The initial and the final wavelengths are scanned in the 610 – 670 nm range. Typical step and count values are shown. Note that the scanning mode is available after the calibration of the crystal, which is performed in the Init submenu.

VMI ACQUIRE (Camera Driving Software): The image acquisition program "VMI Acquire" (Per Johnsson 2009). Figure 29 shows the initialization window and the program environment. The Trigger is provided externally (see camera triggering in the previous discussion). Two acquisition modes are available namely the imaging and the counting mode. Imaging mode records the intensity distribution of the phosphor bright spots which is distributed in several pixels. On the other hand, in the counting mode and for each bright spot a single count is assigned to the pixel that corresponds to the maximum of the intensity distribution of the bright spot. The latter mode slightly increases resolution when a sufficiently large acquisition >10,000 is used. For our measurements imaging mode was used, providing a good enough resolution in conjunction to lower acquisition $\sim 1–5\times10^3$.

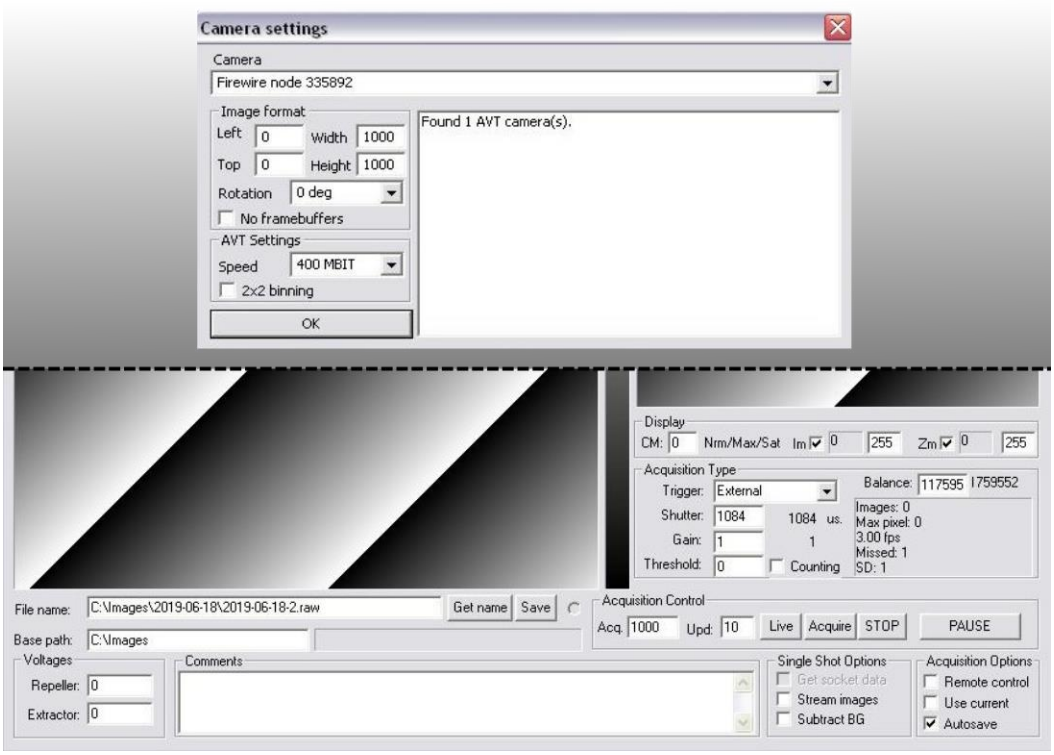

Figure 29. Camera driving software settings are shown in the upper dialog window. The lower window shows a part of the acquisition program front face. The two display windows of the front face, show the captured image (left large display window) and a selected part of it (right small display window). We use the external triggering provided by the custom-made delay module (E. Dimitriadis). The number of accumulated images is controlled by the Acquisition Control submenu.

Throughout our experiments we used two measurement types after selecting the number of shots to be acquired (typically ~1000 shots): (i) Single images are obtained by selecting Acquire and then pressing Save button. Images are saved in Raw format. (ii) Series of images are captured sequentially by checking the Autosave box and selecting the Live acquisition mode. This mode enables us to manually synchronize with the laser scanning and obtain an image on every laser step. For a laser scan of 1000 counts and a step of 0.004 nm we set 1001 image shots Acquisition and then monitor the synchronization (we may need to reduce the camera acquisition to 1000 shots for some images during the scan).

IMAGEJ: Image processing and analysis is performed with the open source program ImageJ developed in Java programing language. Importing the raw images uses the parameters shown in Figure 30. A major advantage of this program is the ability to perform the same operation to a

series of images (Stacks). Below, we present a few examples that have been used for the analysis of the magnesium experimental data.

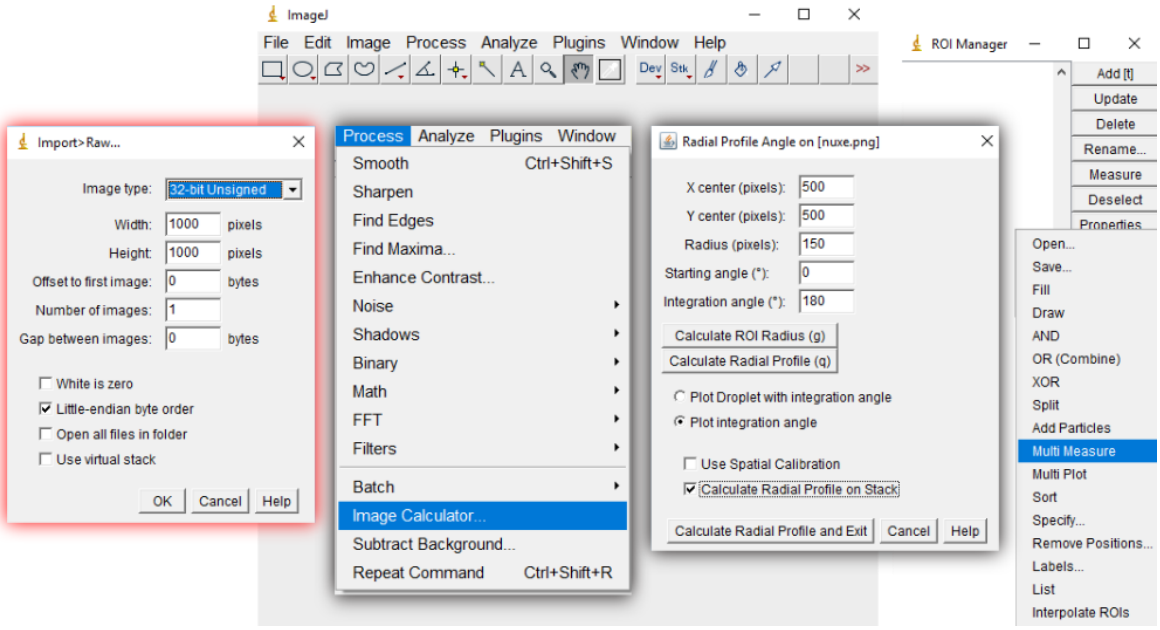

Figure 30. The figure shows some of the ImageJ software dialog windows and used plugins. Images in raw format are imported be selecting the options shown here. The Process submenu contains useful build-in commands such as the Image Calculator. This operation allows for subtracting (/adding/averaging/…e.t.c) images. The Radial Profile Angle plugin settings may vary according to the image center position and the desired radius of integration. Finally, the ROI Manager submenu is shown to highlight the Multi Measure option that allows for measuring quantities on a Stack of images.

Images exhibit a fixed pattern noise (background) that can be eliminated by subtracting an image obtained in the absence of signal. The background image is acquired at 2 – 5 times the normal acquisition shots and then divided by that factor. Total integrated signal, center of mass or maximum pixel value can be measured by the build-in analyze menu. The same quantities can be computed for limited regions of interest (ROIs) that are defined in the ROI manager submenu instead of the entire image.

The intensity profile as a function of the radius from a selected center namely the radial profile, of a PM image is calculated by the "Radial Profile Extended" by Philippe Carl plugin. The plugin produces a profile plot of normalized integrated intensities around concentric circles as a function of distance from the center, with the addition that the script lets you choose the starting

angle and the integration angle. This is also applicable to Stack images. A variety of ImageJ plugins are accessible in Ref. [114].

Symmetrization of images is performed for visual purposes (no quantity has been measured from a symmetrized image). First each image quadrature, with respect to the center, is duplicated to create 4 new images. We flip the quadrature images appropriately with respect to the image axis of symmetry and then average them. This final averaged quadrature is then used to reform a symmetrized image by employing the combine submenu.

LabView® ION SPECTRA ACQUISITION PROGRAM: The boxcar signal is inserted into an oscilloscope (LeCroy 9310C, 400MHz) and recorded via a LabView® homemade program [115]. The interface is presented in Figure 31. The program averages the two signals over the selected sweeps and appends them into two columns on the final name given. The signals should not exceed the maximum visible value on the oscilloscope screen. The acquisition starts and pauses after pressing the start/stop buttons.

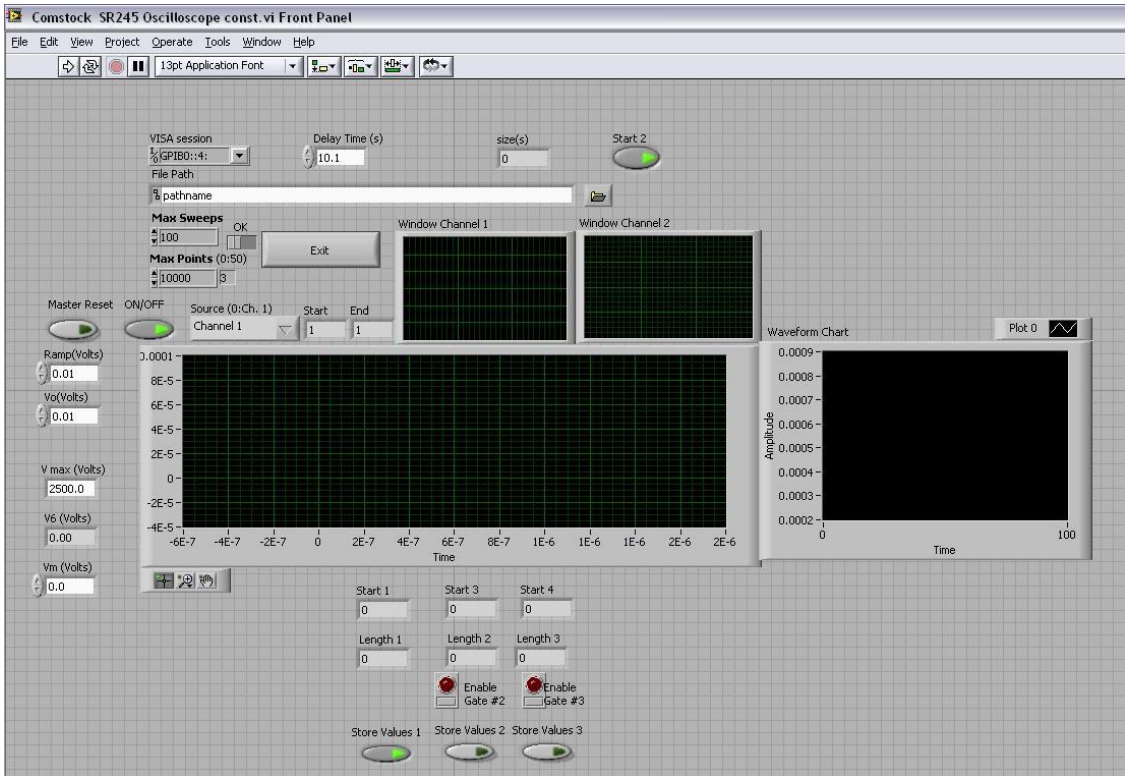

Figure 31. The interface of the custom-mage LabView program (A. Koulouklidis). The program integrates the signal over the gate shown in the bottom of the interface (our signal is slowly varying dc signal provided

by the analog integrator). Note that the button Store Values 1 is checked and only one gate is used (generally three gates are possible). The number of sweeps and the laser repetition rate (10 Hz) determines the delay time (an additional time delay of 0.1 s is required for the program to store the values to the data file).

2.3 Experimental procedure

Experimental measurements require the preliminary steps listed below and then we proceed to the actual measurements. The preliminary experimental steps consist of: Raising the oven voltage (>6 mA) gradually and wait about 1 hour for the temperature to be stabilized. Initiate the laser following a given protocol and wait for the ultraviolet output to stabilize (total 2 hours). A constant stream of Mg vapor and the laser radiation are ready to be used. In general, experimental runs were time consuming due to the waiting time towards thermal stabilization of the systems and the low acquisition rate determined by the laser repetition rate.

2.3.1 Mg^+ Ion Spectra

The total cross section of the laser atom interaction is obtained by collecting the positive ion signal (V_R, V_E >0) for the selected field value *F*. The voltage ratio is typically chosen near the VMI condition(s) 0.68 or 0.73 in order for the measurements to be compatible with acquired image sets. The ions travel in the field free tube and reach the detector at the time of flight. The typical detector voltage values are: V_{MCP}=1600-1800 V and V_{PH}=2000-2200 V. Both OGE (Ne lamp) and ions signal are inserted into a boxcar module (Stanford Research Systems, SR235) allowing for outputting either the latter or the former signal.

We simultaneously start the laser scan and the LabView acquisition program and record the OGE/Ions signal together with the Fabry-Perot intensity fringes. After a strong Ne reference line is recorded, we change the output to the ions and record the rest of the spectral range. The used calibration lines lie below the E_{sp} for the typically used static field values and the ions spectra is not affected. The laser beam is blocked at the end of each scan for the determination of the zero signal. Calibration is performed offline by using the recorded Ne line and the Fabry-Perot fringes.

2.3.2 Alignment Procedures: Imaging the Laser-Atom Interaction Region

The voltages applied to the Repeller/Extractor electrodes of the VMI spectrometer greatly affect the focusing conditions of the spectrometer. In the special case of almost identical voltages $V_E/V_R \sim 1$ the detector images the position of the interaction [106,112], instead of the initial particle velocity. In fact, the LAIR is magnified according to the applied voltages and the laser position

along the spectrometer axis (*z* axis). However, this technique of spatial map imaging is used for alignment purposes and the exact dimensions are not of importance in the present study.

Setting the ratio $V_E/V_R \approx 0.998$ for either positive or negative voltages, we observe a bright line on the detector that is moved in the vertical direction as the laser beam is vertically displaced. Figure 32 presents a series of overlaid images (electron imaging, negative voltages) as the beam is displaced vertically. Note that the bright lines form a round disc-shaped shadow, that is attributed to the projection of the geometrical shadow of the Einzel lens electrodes. This is visible for both electrons or ions imaging. The beam is considered aligned when the bright line is formed in the center of the Einzel lens shadow in the vertical direction.

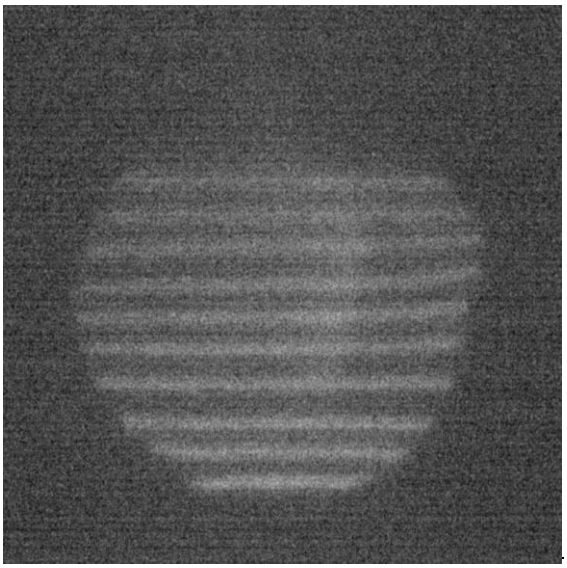

Figure 32. Laser-Atom interaction region electron imaging. Each horizontal line corresponds to a single LAIR imaging for a fixed laser position. The laser beam is then displaced vertically and the all images are overlaid together. Note the formation of disc-shaped shadow, that is attributed to the geometrical shadow of the Einzel lens electrodes.

2.3.3 Imaging – Photoionization Microscopy

In order for the electrons to form fluorescent spots on the phosphor screen, the detector voltages are set within the ranges: V_{MCP}=1600-1800 V and V_{PH}=4000-4200 V. Then for a predetermined $V_R<0$ value and $V_L=0$, we search for sharp images by adjusting the extractor voltage near the $V_E \backsim 0.68\ V_R$. The correct ratio is a function of the laser position along the spectrometer

axis, thus it must be adjusted after each beam alignment. A sharp image without magnification is shown in Figure 22(a). Then the Einzel lens voltage is gradually increased until the maximum predetermined value $V_L<0$ that determines the magnification of the original image. At each step the extractor voltage is adjusted (for low lens voltages images cannot be formed on the detector [95]) until we finally observe a sharp magnified image near the extractor voltage $V_E \simeq 0.73\ V_R$ (Figure 22(b)).

Images for different polarization orientations are obtained by fixing the laser radiation wavelength. Then an image is acquired for each λ/2 rotation angle (minimum step 2 degrees leading to 4 degrees of polarization vector rotation). These sets also provide an absolute calibration of the polarization angle e.g. by examining the glory signal or/and the barycenter of the images with respect to the image center (see polarization discussion).

Series of images were recorded as the laser wavelength was scanned, after "synchronizing" it with the camera (see the discussion on section 2.2.6). The polarization orientation is kept fixed during the image series acquisition. For extremely large energy ranges, the KDP crystal was recalibrated whenever the pulse energy dropped. The Fabry-Perot intensity fringes were recorded simultaneously and the absolute calibration is based on an OGE spectrum after the last scan of each experimental set.

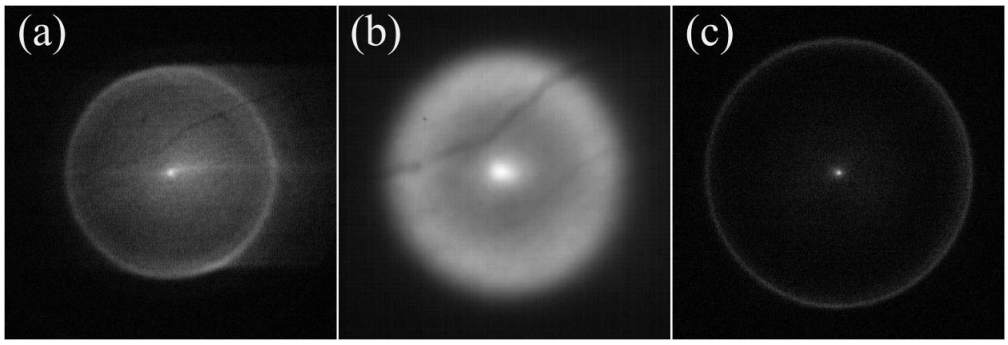

Figure 33. (a) Slow photoelectron image for the *two-photon excitation* out of the magnesium ground state. The laser field polarization is parallel to the static electric field. The focusing *lens is placed outside* of the spectrometer (f≈25 cm). (b) Slow photoelectron image for the *four-photon excitation* out of the magnesium ground state with π-polarization. Again, the focusing lens is placed outside of the spectrometer. (c) Slow photoelectron image for the two-photon excitation out of the magnesium ground state with π-polarization. The used *in-vacuum lens* has a focal length of f ≈5 cm. Both the four-photon excitation scheme and the stronger focusing by using an in-vacuum lens eliminate the coma-like defect of the images by effectively reducing the extension of the LAIR.

Let us finally address the defects observed in the experimental images of Figure 33(a). The first refers to the intensity deficiencies caused by scratches on the MCPs surfaces that were introduced during the detector's assembly by the users. It was found that this defect has little to no effect on the radial profile obtained from the images due to the fact that radial profiles are insensitive to small deficiencies extending to different radii with respect to the image center. In measurements concerning images for different polarization orientations (where the radial profile is less relevant) the surface of the detector used was in perfect condition.

The most striking error is a coma-like extension of the intensity [116]. This is attributed to the large spatial extension of the LAIR in the direction of the laser propagation, at least compared to the suitable one for the "first order" VMI condition to apply. The electrons produced far from the electrode aperture center cannot be focused efficiently and produce a blurred copy of the focused image [94]. Three approaches can treat this issue namely the reduction of the LAIR by: collimating the atomic beam, selecting higher order multiphoton process and finally strongly focus the laser radiation. The first approach is the most suitable because it provides the best determination of the LAIR but it is not used due to lack of appropriate equipment. The second approach is not suitable for the particular study which is devoted to the non-resonant two-photon excitation. For example, in Figure 33(b) a four-photon excitation is employed to demonstrate the achieved minimization of the error. Finally, the third approach i.e. the introduction of an in-vacuum lens of 5 cm focal length, is employed to reduce the error. The LAIR is assumed to be almost equal to beam waist that – for a nearly Gaussian beam profile – is proportional to the squared focal length of the lens. Figure 33(c) presents a two photon PM image using this setup. In general, the laser beam diameter reduction via pinholes (selecting the central part of the beam and subsequently reducing the pulse energy) produces better quality images. The radiation pulse energy was continuously monitored with a joulemeter and its value was within the range 0.2-0.1 mJ/pulse in the LAIR.

Chapter 3: Results & Analysis

3.1 Near-Saddle-Point Images of H and Mg Stark States

3.1.1 Magnesium Ion Spectra & Stark Maps

The discussion on the effects exhibited by PM images near the saddle point energy would be greatly facilitated by a preceding brief presentation of the two photon Mg Stark spectra recorded in the vicinity of E_{sp} and above for the static fields F~700 V/cm of interest (principal quantum number n~30 and well beyond the l-mixing range). In fact, our aim here is not a detailed spectroscopic study devoted on energy level positions and lineshapes but, instead, the identification of the gross near-saddle-point spectral features. Typical two-photon Mg+ spectra out of the Mg ground state for π- and σ-polarization are presented in Figure 34 (a,b,c). These schemes populate m=0 and $|m|$=0,2 states, respectively. The laser pulse energy was reduced in order to avoid saturation effects. Under such conditions, the Mg^+ signal (black solid line) is proportional to the total ionization cross section σ_{tot}. The latter typically exhibits a negligible signal below the saddle point energy, while above it we observe a series of almost equidistant spectral lines build upon a slowly varying background signal [68,71]. This background is attributed to the simultaneous presence of continuum states along with the resonances. The profile of the background is apparently different for the π- and σ- spectra. The smallest recorded Stark resonance linewidth is ~0.5 cm^{-1}, but in the spectra of Figure 34 the majority of observed spectral lines exhibit linewidths of ~1 cm^{-1} (or even higher). This fact, in conjunction with theoretical calculations of σ_{tot} [92] imply the presence of several unresolved resonances within each spectral line. Furthermore, the π- and σ- spectra exhibit resonant lines at almost the same locations, but with occasionally different line profiles. This quasi-degeneracy of $|m|$=0 and 2 resonances has been predicted by earlier semi-classical theoretical works and occurs for either hydrogenic or multielectron atom near-threshold Stark spectra [62,65,117]. The observed spectral lines are affected by the inhomogeneity of the electric field within the LAIR volume that introduces an additional spectral broadening.

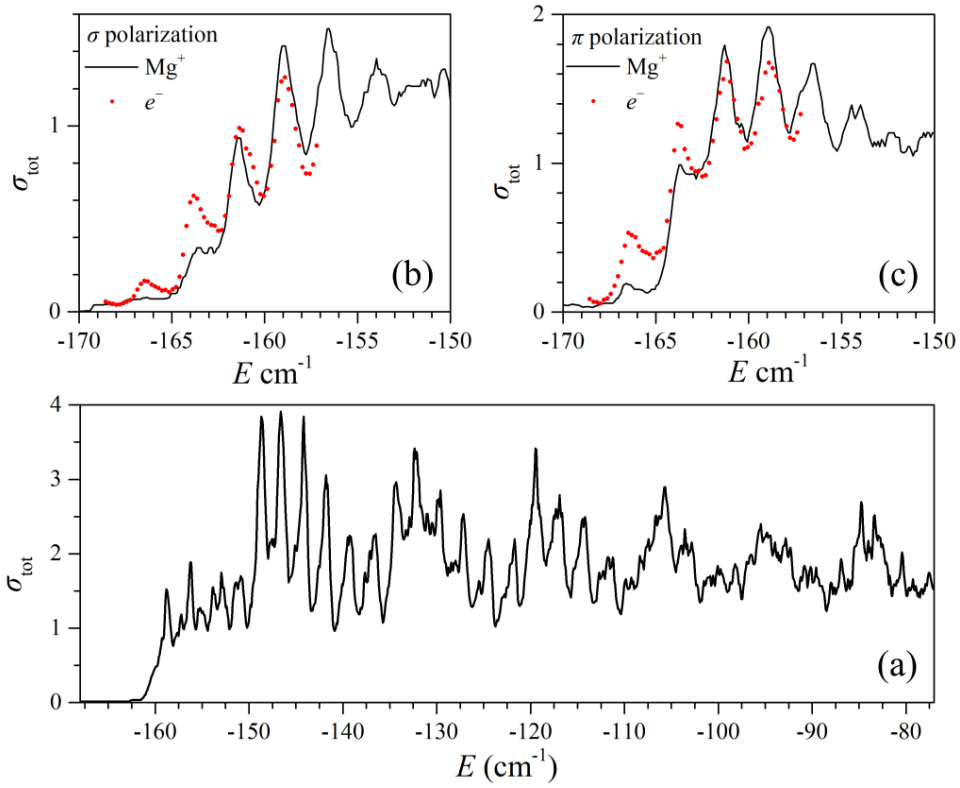

Figure 34. (a) Mg^+ signal (black line) for the π-polarization two-photon excitation scheme. This m=0 spectrum exhibits a series of narrow spectral lines overlaid on a slow varying but oscillating background. (b) Yet another two-photon ion spectrum near the E_{sp} energy range, obtained by employing the same excitation scheme as in (a). Also shown, the integrated electron signal (red points) of PM images recorded with identical conditions but reversed polarity of the spectrometer electrodes. (c) Mg^+ signal and integrated electron signal recorded by using a σ-polarization two-photon excitation scheme.

Reversing the polarity of the voltages applied to the spectrometer and retaining otherwise identical conditions allows for obtaining electron images. Then the (angularly and radially) integrated electron signal of the images (red points in Figure 34(b,c)) provides the total ionization cross section σ_{tot} i.e. the obtained information is equivalent and apparently identical to that obtained by the Mg^+ signal. In fact, differences occur solely for the weak resonances extremely near the E_{sp}, where the line intensities of electron signals are higher than their Mg^+ counterparts. This is probably attributed to the low sensitivity of our ions detection method when extremely low electric signals are involved.

More information can be obtained by studying the total cross section by means of the so-called Stark maps [14,28,92,118], consisting of E-F representations of σ_{tot} revealing the evolution of energy levels as a function of the static field strength. Stark maps occasionally uncover striking

effects which are otherwise hindered in single spectra. Building the Stark map requires the recording of the Mg^+ signal as a function of the excitation energy for different values of F. Although Stark maps were more frequently employed for the $E<E_{sp}$ range [28], in this work we have studied the $E>E_{sp}$ range which is, at least presently, the only relevant one for PM studies. The resulting map for two-photon excitation out of the magnesium ground state and with π-polarization is presented in Figure 35.

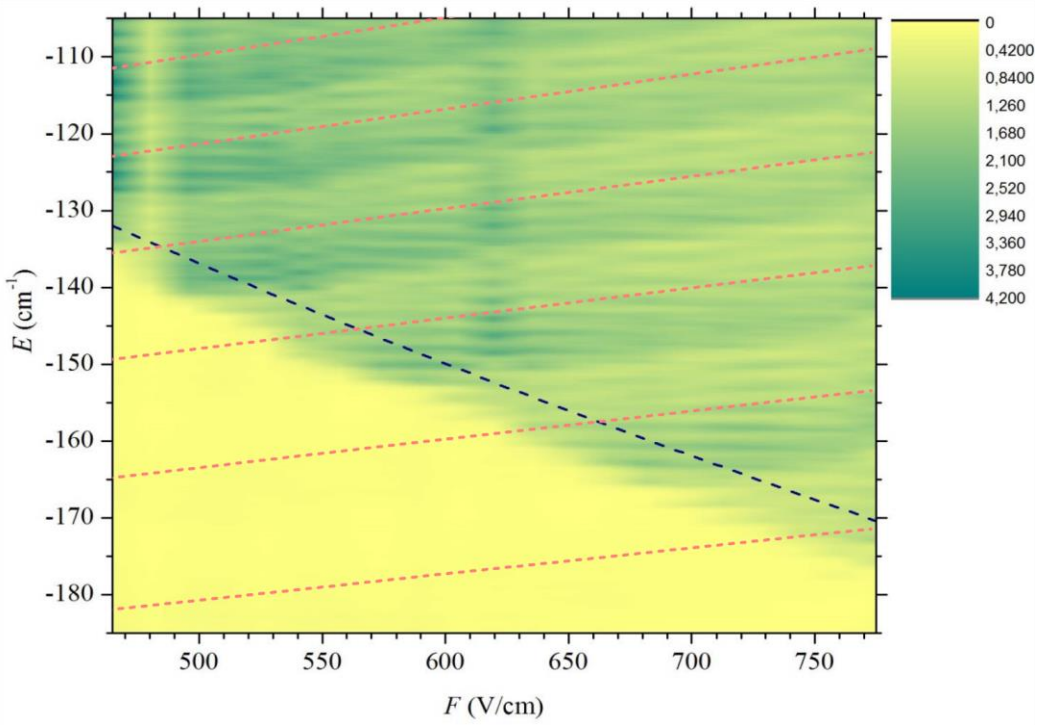

Figure 35. Stark map for the two-photon excitation out of the magnesium ground state and with π-polarization. The contour plot includes Mg^+ spectra for twenty field values in the shown field range. Also shown are the classical saddle point energy (black dashed line) and the positions of the SFIS (red dashed line).

The energy calibration of the spectra is performed as discussed in section 2.3.1. and the energy step for all scans is the lowest available by our laser system (~0.1 cm^{-1}). The field strength is varied by changing the electrode voltages. The voltage V_R is varied within the (3500 – 4500 V) range while the voltage ratio is retained constant V_E/V_R=0.72 (near to the VMI condition for magnified images). The absolute field calibration is based on the fitting of the $\rho_{max}^{cl}(E)$ function (Eq. (26)) to the outer radius of images acquired under the same conditions for selected V_R values.

The relative field calibration between adjacent spectra is based solely on the applied voltage differences [118].

The examination of Figure 35 reveals that, the transition from negligible to strong ion signal is fairly well described by the classical E_{sp} curve (dashed black line). It is interesting to note, however, that the resonances which are just below E_{sp} (i.e. in the absence of any continuum) ionize necessarily via tunneling, like the hydrogenic resonances.

Further, the energy positions of the observed sharp lines generally evolve in a complex manner. These maxima appear almost on the same energy for some field ranges while for others their behavior shows evidence of the existence of avoided crossings [28]. Additionally, the map clearly displays the formation of envelopes that modulate the intensities of these sharp spectral lines. This behavior was also observed in the Mg-Stark spectra of Ref. [68,71]. Interestingly, the envelopes are blue-shifted with increasing F and their centers are very well predicted by the quantization condition Eq. (30) that in turn is connected to the energy positions of the SFIS. This is a rather unexpected result because up to now SFIS were mainly studied within the positive energy range. Thus, the present results imply that the notion may still exist at negative energies where static field induced structure could coexist with TS. Alternatively, the aforementioned quantization condition could simply characterize the n_1-channel openings. This is not very probable however, because the envelope formation characterizes solely the m=0 spectra while it is difficult to observe in the $|m|$=2-dominated ones obtained with σ-polarization (as is the case for the positive energy SFIS [63,64]).

3.1.2 Near threshold Photoionization Microscopy Images

3.1.2.a Hydrogen Atom

Having presented the characteristics of Mg-Stark spectra near the saddle point energy, we now proceed to the discussion of the corresponding near-threshold PM images of Mg and particularly those showing resonant characteristics. For comparison purposes, however, it would be instructive to expose first the structure and energy evolution of the relevant hydrogenic near-threshold PM images. To this purpose, we begin here our discussion by a presentation of an ex-

ample concerning the resonant and non-resonant effects emerging in the vicinity of the hydrogenic quasi-bound $(n_1,n_2,m)=(2,27,0)$ Stark state. The latter state was studied fairly recently, both experimentally [24] and theoretically [26], while we have already presented the relevant wave-functions in Figure 8 of section 1.2.1.

Experimentally this state was reached via a single photon transition out of an n=2, m=0 excited state using π-polarized light. In our theoretical modeling, l-mixing in the initial state due to the presence of the static field [14,24] is simulated by the use of the semi-parabolic states namely, we employ either the state $(2,0,1,0) = 2^{-1/2}[|2s\rangle + |2p_{m=0}\rangle]$ or the $(2,0,1,0) = 2^{-1/2}[|2s\rangle - |2p_{m=0}\rangle]$ one. In fact, the latter state led to PM images that did hardly exhibit any resonant effects because the excitation strength of the resonance proved to be comparable with that of the continua [27]. This observation implies a strong dependence of the resonant manifestations on the initial state.

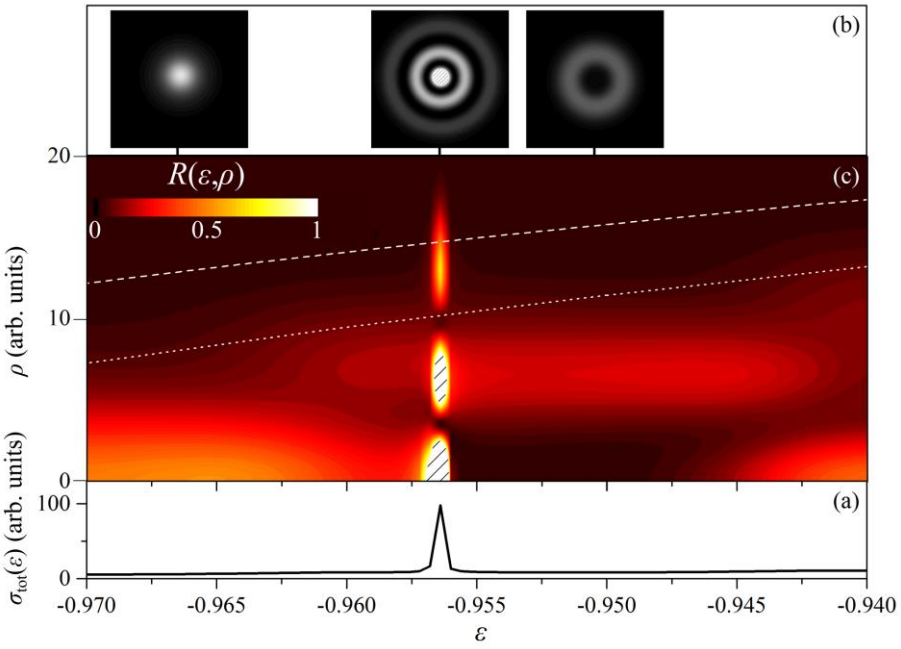

Figure 36. (a) Hydrogenic total cross section for one-photon excitation out of the $|2,0,1,0\rangle$ initial state to m=0 final states. F=808 V/cm. The spectral line located at ε=−0.9564 corresponds to the (2,27,0) Stark resonance. (b) $J_{\upsilon_{det}}$ images computed for υ_{det}=1000 au, below, on, and above the resonant energy. The resonant image shows an additional dark fringe and an enlarged image size as compared to the non-resonant images. (c) Linear scale contour map of the radial distribution $R(\varepsilon,\rho)$ in the vicinity of the resonance. Hatched areas denote intensity cuts. Also shown are the maximum classical radius ρ_{max}^{cl} (white dashed line) and the secondary bow radius ρ_{II} (white dotted line), calculated under the same conditions used for $R(\varepsilon,\rho)$.

Therefore, in accord to [26], we discuss below the results obtained using the (2,0,1,0) state for F=808 V/cm and υ_{det}=1000 a.u. ($z_{det}\approx$–25 μm). The total ionization cross section σ_{tot} is shown in Figure 36(a) and consists of a strong spectral line, corresponding to the (2,27,0) resonance, build upon a weak background. Figure 36(b) presents images for energies below, on and above the resonant energy. These images accurately reproduce the corresponding experimental data of Ref. [24] that are presented in Figure 37. The experimental images show no angular dependence as expected for the m=0 final states. The enlarged number of nodes and the increased size of the on-resonance image is striking.

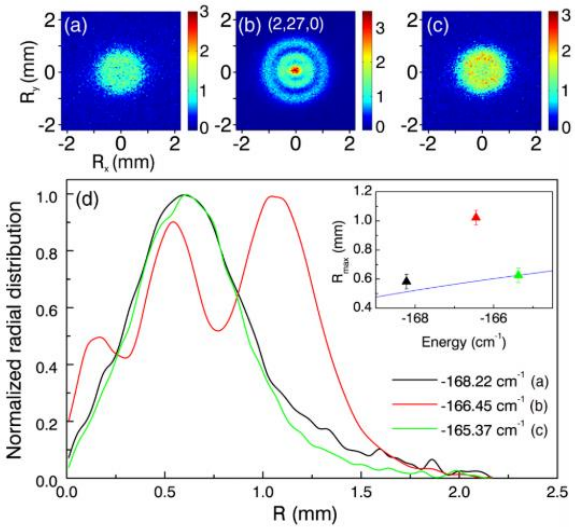

Figure 37. The authors of Ref. [24] kindly allowed for their figure to be presented in this thesis. "Evidence for on-resonance ionization by tunneling through the Coulomb + static field potential. A comparison is shown between a measurement carried out for the $(n_1, n_2, m) = (2,27,0)$ resonance (b) and two non-resonant measurements performed 1.8 cm^{-1} below (a) and 1.1 cm^{-1} above (c) this resonance.". "The normalized radial distribution of the on- resonance measurement containing three maxima extends significantly further outward than the two off-resonance measurements which show only a single maximum (d). The inset in (d) shows a comparison of the radial extension of the experimental images, defined as the position of the outer maximum (color triangles) and the theoretical radial extension (blue, solid line) according to the classical formula …" More details are given in FIG. 4 of [24].

Let us now examine the contour plot of Figure 36(c) that shows the radial distribution $R(\varepsilon,\rho)$ of Eq. (71) in the neighborhood of the resonance. The channel thresholds (see Eq. (50)) of interest are: $\varepsilon_{\rm thr}^{0,0} = \frac{E_{\rm thr}^{0,0}}{|E_{sp}^{cl}|} = -0.99$, $\varepsilon_{\rm thr}^{1,0} = -0.97$ and $\varepsilon_{\rm thr}^{2,0} = -0.95$. Let us first assume the absence of resonances and consider a given energy ε, for which there are solely continua with quantum

numbers $0 \leq n \leq n_1^o$. Then it holds that, $\varepsilon_{\text{thr}}^{n_1^o,m} < \varepsilon < \varepsilon_{\text{thr}}^{n_1^o+1,m}$ and the summation of the electron current probability density (Eq. (70)) runs only up to n_1^o and the corresponding $X_{n_1}(\chi)$ wave functions contribute to the image with comparable weights, $c_{n_1,m} = d_{n_1,m} e^{im\varphi} e^{i[\theta_{n_1,|m|}(\upsilon_{det}) + \phi_{n_1,|m|}]}$. Then the interferogram exhibits up to n_1^o dark fringes and for large ρ values is dominated by $X_{n_1^o}(\chi)$ [22]. For example, the first and the last image of Figure 36(b) and their corresponding radial distributions lies in the range $\varepsilon_{\text{thr}}^{1,0} < \varepsilon < \varepsilon_{\text{thr}}^{2,0}$ and exhibits 0 and 1 nodes ($\leq n_1^o$=1), respectively.

Consider now the presence of a quasi-bound state with quantum number n_1^{res}, as in our case where $n_1^{res} = 2$ for the (2,27,0) resonance. It turns out that for the chosen initial state the weight $\left|c_{n_1^{res},m^{res}}\right|$ of the quasi-bound state is about an order of magnitude larger than the weights of the continua and this is also evident in σ_{tot}. Thus, the on-resonance image and radial distribution of Figure 36 exhibit the resonant features, i.e. n_1^{res} dark fringes and an increased image size due to the dominance of $X_{n_1^{res}}(\chi)$ in $J_{\upsilon_{det}}$. Note that, by definition $n_1^{res} > n_1^o$ and this condition leads always to an increased number of dark fringes and outer image radii due to the dominance of $X_{n_1^{res}}(\chi)$ in Eq. (70). From another perspective, these effects are attributed to the electron escape via tunneling, which is the only ionization mechanism of the hydrogenic quasi-bound states [11,25,30].

Turning now our attention to the non-resonant radial distributions, it is interesting to note that the contour plot reveals that outer radii of non-resonant $R(\varepsilon,\rho)$ distributions increases monotonously but in a stepwise manner. Indeed, the distribution increases abruptly just above each channel threshold (at the energy $\varepsilon_{\text{thr}}^{n_1^o,m}+\Delta\varepsilon$, with $\Delta\varepsilon \approx 0.005$) and subsequently its extension remains almost constant.

This constant outer radius between channel transformations to continua and the stepwise non-resonant energy evolution of the outer radius are features typically characterizing the $\varepsilon \sim -1$ range. It is noted, however, that in some other calculations the constant radius effect still persists while the sudden jumps are not always observed. In any case the behavior of the outer image radius differs radically from the classical predictions. For example, Figure 36(c) also shows the classical secondary bow radius $\rho_{II}(\varepsilon)$ (white dotted line) and the classical maximum radius $\rho_{\text{max}}^{\text{cl}}(\varepsilon)$ (white dashed line), for the same F and υ_{det}. These classical curves don't exhibit the aforementioned

stepwise evolution. Moreover, $\rho_{\max}^{\mathrm{cl}}$ systematically overestimates the non-resonant outer radii while ρ_{II} matches the $R(\varepsilon,\rho)$ outer turning point at the beginning of each step, i.e. $\varepsilon=\varepsilon_{\mathrm{thr}}^{n_1^0,m}+\Delta\varepsilon$.

3.1.2.b Magnesium Atom

With the above discussion in mind, let us now turn our attention to our experimental data concerning the magnesium atom. Our measurements are summarized in Figure 38. Figure 38(a) shows a selection of non-resonant experimental images that display the well-known monotonous increase of the number of dark fringes with energy (intensity radial nodes (zero signal) are displayed with white color in the image color-scale). The σ-polarization, two-photon excitation scheme ($\Delta m=\pm1$ per photon) populates $|m|$=0,2 Mg states. Note the clear difference in the angular distribution between the lowest energy image and the images at higher energy. Indeed, the lowest-energy images are disc shaped and show no angular dependence, signaling the exclusive excitation of m=0 states. However, for energies higher than $E\approx-155.5$ cm^{-1}, all images exhibit a $\cos^2(2\varphi)$ (cross-like) angular distribution that is distinctive of the $|m|=2$ character [27,30]. In an attempt to quantify this transition phenomenologically, we employ the angular function,

$$s(\varphi)=\int_0^{\infty}\mathrm{J}_{v_{\mathrm{det}}}(\varphi,\rho)d\rho\ . \tag{109}$$

More specifically, in Figure 38(b) we present the ratio $s(45^o)/s(90^o)$ which is expected to be equal to unity for pure m=0 states and zero for pure $|m|$=2 states. The curve is equal to unity for energies lower than ≈−155.5 cm^{-1}, and subsequently exhibits a rapid decrease. This observation is consistent with Eq. (27) predicting $E_{\mathrm{sp}}\equiv E_{\mathrm{sp},m=0}^{\mathrm{cl}}<E_{\mathrm{sp},m=2}^{\mathrm{cl}}$ and a well-defined (but field dependent) energy difference. These criteria, together with a first estimate of E_{sp} based on the energy of the first image where a quantifiable signal could be obtained, lead to a field determination of F=680±10 V/cm. The corresponding saddle point energies $E_{\mathrm{sp},0}^{\mathrm{cl}}$, $E_{\mathrm{sp},2}^{\mathrm{cl}}$, for this field, are shown with dashed-dotted lines. Thus, Eq. (27) is validated on the basis of angular distributions. This compares well with the results of earlier methods based on m-dependent field ionization thresholds of individual Rydberg states [58,119]. Finally, the m-beating arising from multiple-m excitation (see section 1.3.1) is manifested as a difference in the fringe contrast along

the vertical and the horizontal orientation [27,30]. Apart from this weak beating effect, however, the recorded images show a dominance of the $|m|=2$ character over the $m=0$ one.

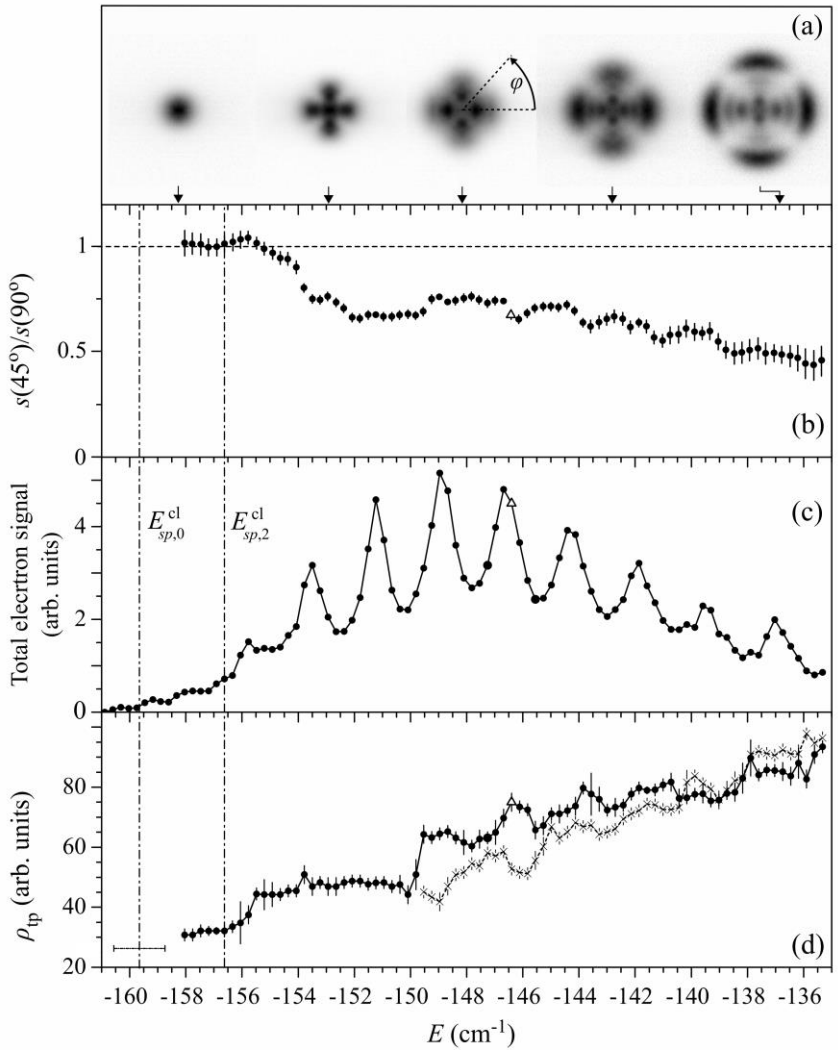

Figure 38. (a) Near-threshold symmetrized images recorded with σ-polarization (|m|= 0,2 final Stark states) at selected energies, marked with arrows. Symmetrization is applied for signal-to-noise ratio improvement and is described in section 2.2.6. The gray scale is stretched from zero (white) to 100% (black) for each image. (b) Ratio $s(\varphi=45^{\circ})/s(\varphi=90^{\circ})$ of the angular factor defined in Eq. (109). (c) Near-threshold total integrated electron signal (σ-polarization). Each point corresponds to a recorded image. (d) Outermost deflection point of $P^{1/2}(\rho)$ (defined in the main text) for σ-polarization (black circles, solid line) and π-polarization (crosses, dashed line). The open triangle denotes the energy location of a quasi-bound state whose image and radial distribution $R(\rho)$ are given in Figure 39. Vertical dash-dotted lines denote the estimated m-dependent saddle point energies.

Images are acquired with an energy step of ≈−0.3 cm^{-1} and the total integrated signal ($\propto\sigma_{\text{tot}}$) is plotted in Figure 38(c). The spectrum shows a series of broad spectral lines overlaid upon a slowly varying background (see section 3.1.1). The apparent resonant-to-background ratio is about ~ 2:1. The corresponding π-polarization spectrum obtained from disk shaped images (only m=0 final states), presents resonances at almost the same locations to those of Figure 38(c) but with a slightly lower resonant-to-background ratio. These degeneracies are also to be expected for the, $E_{\text{thr}}^{n_1,|m|=2}$and $E_{\text{thr}}^{n_1+1,m=0}$ channel thresholds [70]. Note that several minima of the ratio shown in Figure 38(b), characterize $|m|$=2 resonances and lie very close to the resonant maxima (more accurately, on the blue side of maxima) of the spectrum.

Having that in mind, let us quantify the extension of the images in fashion similar to that followed in Ref. [70]. Thus, in the present work the radial extension of each image is defined as the outermost deflection point of $P^{1/2}(\rho)$, that is, the outermost radius for which $\frac{d^2[P^{1/2}(\rho)]}{d\rho^2}=0$. This choice is based on the fact that for $\rho\to\infty$, and consequently $\chi\to\infty$, $P^{1/2}(\rho)\to\left|X_{n_1^{\max},|m|}\right|$, where $n_1^{\max}$ denotes the larger value of n_1 for which the corresponding wave function contributes to the interferogram with a significant weight $\left|c_{n_1,m}\right|$. Therefore, the outermost inflection point corresponds to the outer turning point ρ_{tp} of $X_{n_1^{\max},|m|}$. It is noted that in [22] a different definition was employed that was based on the outermost deflection point of $P(\rho)$ instead of $P^{1/2}(\rho)$. Irrespective of the exact definition, however, the inflection points are independent of the magnitude of $P(\rho)$ and consequently of σ_{tot}. Following the earlier discussion of this section on hydrogenic near-threshold images, in the absence of resonances $n_1^{\max}(E)=n_1^{\text{o}}(E)$ and the ρ_{tp} curve may probe n_1-channel openings. However, in the case of the presence of a fairly strong resonance, $n_1^{\max}=n_1^{\text{res}}(>n_1^{\text{o}})$ and consequently ρ_{tp} should correspond to the extension of $X_{n_1^{\text{res}},|m|}$ wave function, expected to be larger than the extension of the continuum states.

The ρ_{tp} is plotted in Figure 38(d) for the σ-polarization case (black solid points), which, as already mentioned, is dominated by the $|m|$=2 states. The n_1-channel mixing of the latter states, is expected to be weaker than in the m=0 ones, due to the weaker penetration of the excited electron to the ionic core (see section 1.2.4). In other words, the conditions are rather favorable for the magnitude $\left|c_{n_1^{\text{res}},m^{\text{res}}}\right|$ of some resonant weight, to be higher than the magnitude of the non-resonant weights, in order for the resonant signatures to be observed even in the presence of the "parasitic" m=0 electron signal. The ρ_{tp} energy evolution is generally monotonous (within error

bars) but occasionally discontinuous (see the evident steps at ≈−155 and ≈−149cm^{-1}). This steplike behavior is resolved due to the small energy step employed in our study and seems to persist with increasing energy. However, the reduced contrast at higher energies makes it difficult to analyze and comment each separate step. As mentioned above in the hydrogenic example, the occasional occurrence of ρ_{tp} may probe n_1-channel openings which occur in the neighborhood of each $E_{thr}^{n_1,m}$ threshold. For example, the abrupt increase of ρ_{tp} located at ≈−155 cm^{-1} corresponds to the opening of the $|m|= 2$, $n_1 = 0$ channel (and also of the quasi-degenerate $|m|= 0$, $n_1 = 1$ one). On the other hand, the $|m|= 2$, $n_1 = 1$ channel opening that, according to the hydrogenic trends, would be expected at ≈−153cm^{-1} is not observed. Apparently, the particular initial state and excitation scheme determines which of the jumps will be resolved, a statement that is also true to the hydrogen atom [27].

More interesting are the few cases where the turning point radius evolves non-monotonously and peaks near the maxima of the spectral lines of σ_{tot}. Experimental [21,22,23,70] as well as theoretical studies [11,25,30,33] in addition to the hydrogenic example presented above links this behavior to the presence of quasibound states ionizing mostly by tunneling (resonances). For clarity we do not deal with the cases of Figure 38(d) where the turning point modulation amplitude is rather small as compared with the estimated error bars. Instead, we comment on the clearly manifested peak of ρ_{tp} located at ≈−146.4 cm^{-1} lying between the estimated locations of the $n_1 = 2$ and $n_1 = 3$, ($|m|= 2$) channel openings. This maximum occurs slightly on the blue side of the corresponding resonance of σ_{to} and it is absent in the ρ_{tp} curve recorded with π-polarization (× points in Figure 38(d)). This curve exhibits a weak local maximum around −147 cm^{-1} and a dip around the energy of interest. This structure could stem from the n_1-channel openings and/or the presence of an $m = 0$ resonance located at ≈−147 cm^{-1}, but the inspection of the corresponding $m = 0$ images is inconclusive. In any case, we confidently conclude that the non-monotonous behavior of the σ-polarization $\rho_{tp}(E)$ curve at ≈−146.4 cm^{-1} probes an $|m|= 2$ resonance based on the absence of a strong ρ_{tp} peak and the clear minimum observed in Figure 38(b) at this energy in the π-polarization spectrum.

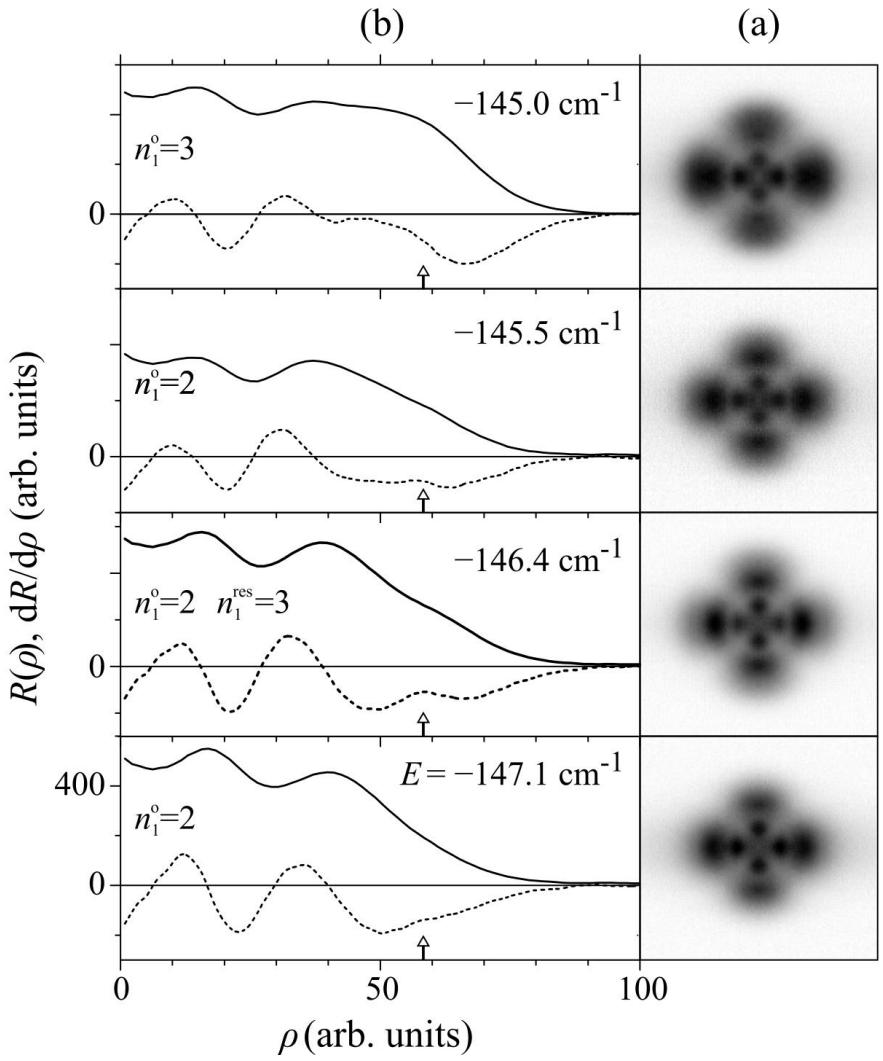

Figure 39. (a) Symmetrized images and (b), their corresponding radial distributions recorded with σ-polarization in the vicinity of the quasi-bound state at −146.4 cm^{-1} (see main text and Figure 38). For each image in (a), the gray scale is stretched from zero (white) to 100% (black). On the other hand, the *y*-axes of (b) are meaningful and denote the relative magnitudes of $R(\rho)$. Also shown in (b), the derivatives $dR/d\rho$ (dashed line) and the relevant n_1^{res} and n_1^{o} numbers. The derivative of the resonant energy exhibits an outer turning point at $\rho\sim57$ arbitrary length (white-head arrow). This signifies the presence of a weak outer "bump" in the radial distribution and an outer halo in the corresponding image. Note that the $n_1 = 3$ channel opening (E =−145.0 cm^{-1}) is characterized by the onset of appearance of an additional fringe at $\rho< 50$ arbitrary length units.

Figure 39 shows images (Figure 39(a)) and their corresponding radial distributions (Figure 39(b)) in the vicinity of the resonance. Starting from bottom to top we present the images below (−147.1 cm^{-1}), on (−146.4 cm^{-1}) and above (−145.5 cm^{-1}, −145 cm^{-1}) the resonant energy. Note that the resonant image exhibits an outer halo that is translated into an outer bump in $R(\rho)$. This

feature effectively "pushes" the outer turning point to higher distances and is responsible for the ρ_{tp} peak in Figure 38(d) near the resonant energy. Nevertheless, the expected appearance of additional bright fringes, (typically one, implying $n_1^{max} = n_1^{res} = n_1^o + 1$) is not apparent by visually examining the radial distributions. For that purpose, in Figure 39(b) we also plot the derivatives $\frac{d[R(\rho)]}{d\rho}$, denoted with black dashed line. Note that these curves exhibit roots corresponding to extrema of $R(\rho)$. Interestingly, the derivatives also exhibit an extremum at $\rho \sim 57$ arbitrary length units (alu). This is marked with an arrow and is attributed to the partial formation of an additional node of $R(\rho)$. This extremum is present in the whole $-147 \leq E \leq -145.5$ cm^{-1} range, but it is clearly visible for $E = -146.4$ cm^{-1} while it is hardly visible in non-resonant derivatives. Apparently, the resonant character, as quantified by the weight $\left|c_{n_1^{res},m^{res}}\right|$, is spread across the spectral line and peaks at the resonant energy. This result is in accord with earlier studies where a similar resonant spread was reported [22]. For $E \geq -145$ cm^{-1}, the aforementioned derivative extremum disappears and instead we evidence the appearance of an additional fringe located at $\rho < 50$ alu (more apparent in subsequent images at higher energies) together with the accompanying increased radial extension which signals the next n_1-channel opening. Apparently, the observed resonance corresponds to $n_1^{res} = 3$ and it is the last quasi-bound state before the n_1=3 channel is transformed to a continuum channel.

The above, rather faint, resonance manifestation was also traced as a function of the field strength. Specifically, we recorded similar image sets for field values up to ±5 V/cm apart from the field employed in Figures 38 and 39. These measurements showed a greatly reduced outer halo and this observation implies a strong dependence of the resonant-continuum coupling on F, as already predicted by the earlier theoretical work of Ref. [33].

3.2 Radial distribution Maps of Magnesium & Related Observables

3.2.1 Radial Distribution Maps

Here we study the energy evolution of the radial distributions $R(\varepsilon,\rho)$ as defined in Eq. (71), for the experimental magnesium images and subsequently compare them to hydrogenic calculations. The linear laser polarization is parallel to the direction of the static electric field and we excite m = 0, magnesium final Stark states via a two-photon scheme, out of the ground state. The used VMI conditions achieve a ~20-fold magnification of the images that have the size of few mm (~20 mm for ε=0). Figure 40 shows a series of typical high acquisition non-resonant PM images within the whole energy range of interest. The observed energy evolution is in accord with the earlier studies [18,22,24]. This single image presentation, however, is not truly demonstrative of the rapid variations exhibited by its different image parts as a function of energy. Moreover, the full set of experimental data consists of about 1000 images and it is meaningless to be presented in this form. For these reasons, the radial distribution of each image is plotted as function of energy in a common contour plot, which is referred to as the radial distribution map.

The m=0 experimental total cross-section and radial distribution map recorded in magnesium atom in almost the full $-1 \le \varepsilon \le 1$ range is shown in Figure 41(a) and 41(b), respectively. Parts of the same map are given in greater detail in Figure 41(c) and 41(d). The images (an example of which is shown in the inset of Figure 41(c)) were recorded at a constant energy step of $E \approx 0.4$ cm^{-1} ($\varepsilon \approx 2\times10^{-3}$). The static electric field was estimated via a number of different methods. A first estimate was provided by the $n_1 = 0$ and $n_1 = 1$ channel openings. Next, at positive energies we have compared the observed "frequency" of glory oscillations to the one predicted by hydrogenic theory. Finally, the outermost turning point radius of the high energy ($E > -50$ cm^{-1}) radial distributions were fitted to the analytical expression for $\rho_{max}^{cl}(\varepsilon)$ [11,16,52] (Eq. (26)). All the methods converged to a field value of F = 680±10 V/cm, which is used for calculating the reduced energy ε, given in the upper x axes of Figures 41(a)–41(d). The radius ρ of all the maps is scaled to $\rho_{max}^{cl}(\varepsilon=0)$. In fact, at $\varepsilon \approx 0$ this radius is slightly larger than the classical secondary-bow radius ρ_{II} (ε=0) by a factor of ≈ 1.01. By employing this ratio, we found a refined experimental value for $\rho_{max}^{cl}(\varepsilon=0)$ and scaled our radius ρ to it.

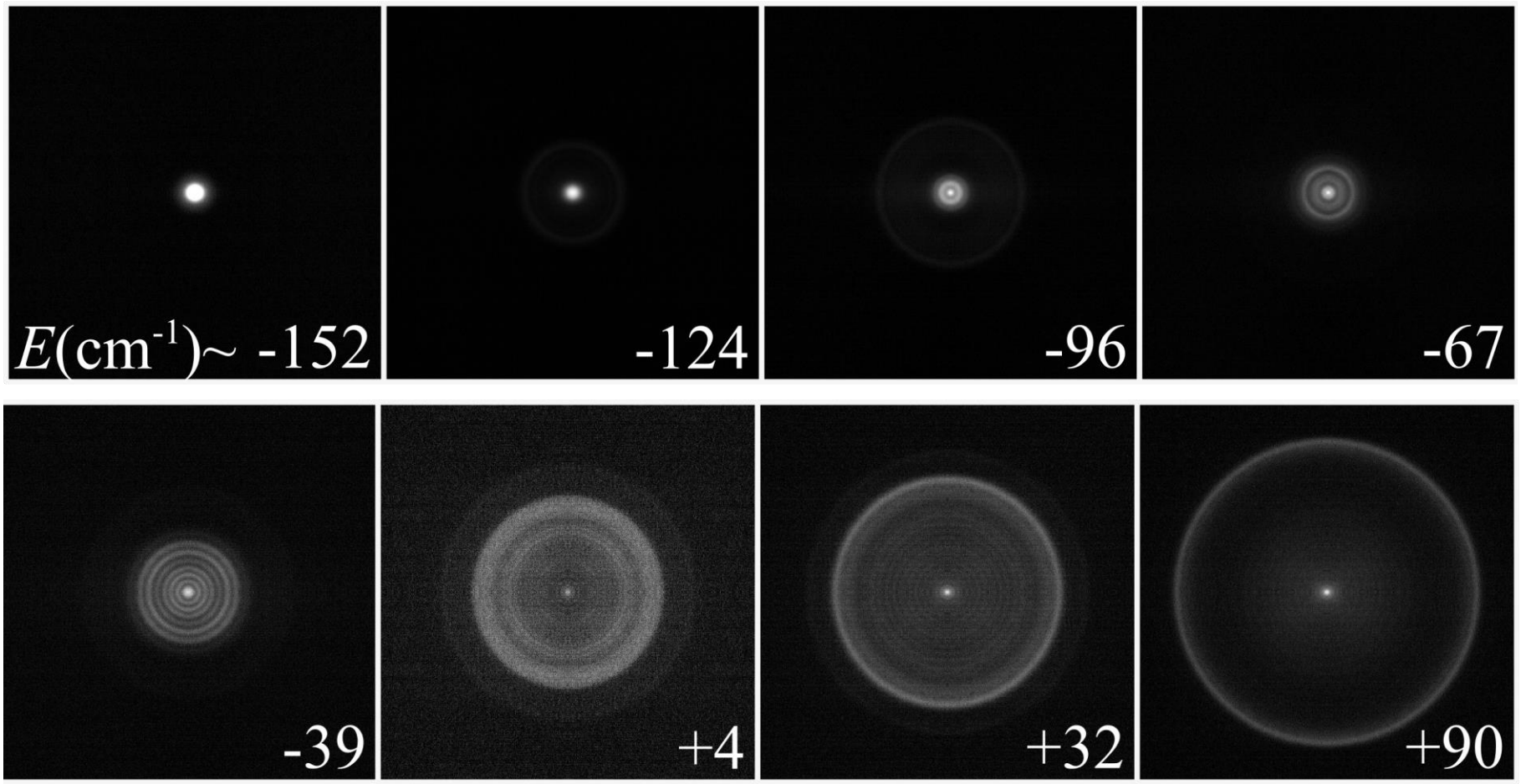

Figure 40. Symmetrized PM images recorded with π-polarization within a large energy range. The static electric field strength is *F*~680 V/cm, leading to an estimated saddle point energy of $E_{sp} \sim -160\ cm^{-1}$. The linear color scale is stretched for each individual image from zero (black) to the maximum intensity value (white). The images exhibit a monotonously increasing size as a function of energy. Note that the indirect fringe system is barely visible but the direct fringe system manifest itself as the dominant feature of the image, along with the glory and bow signals.

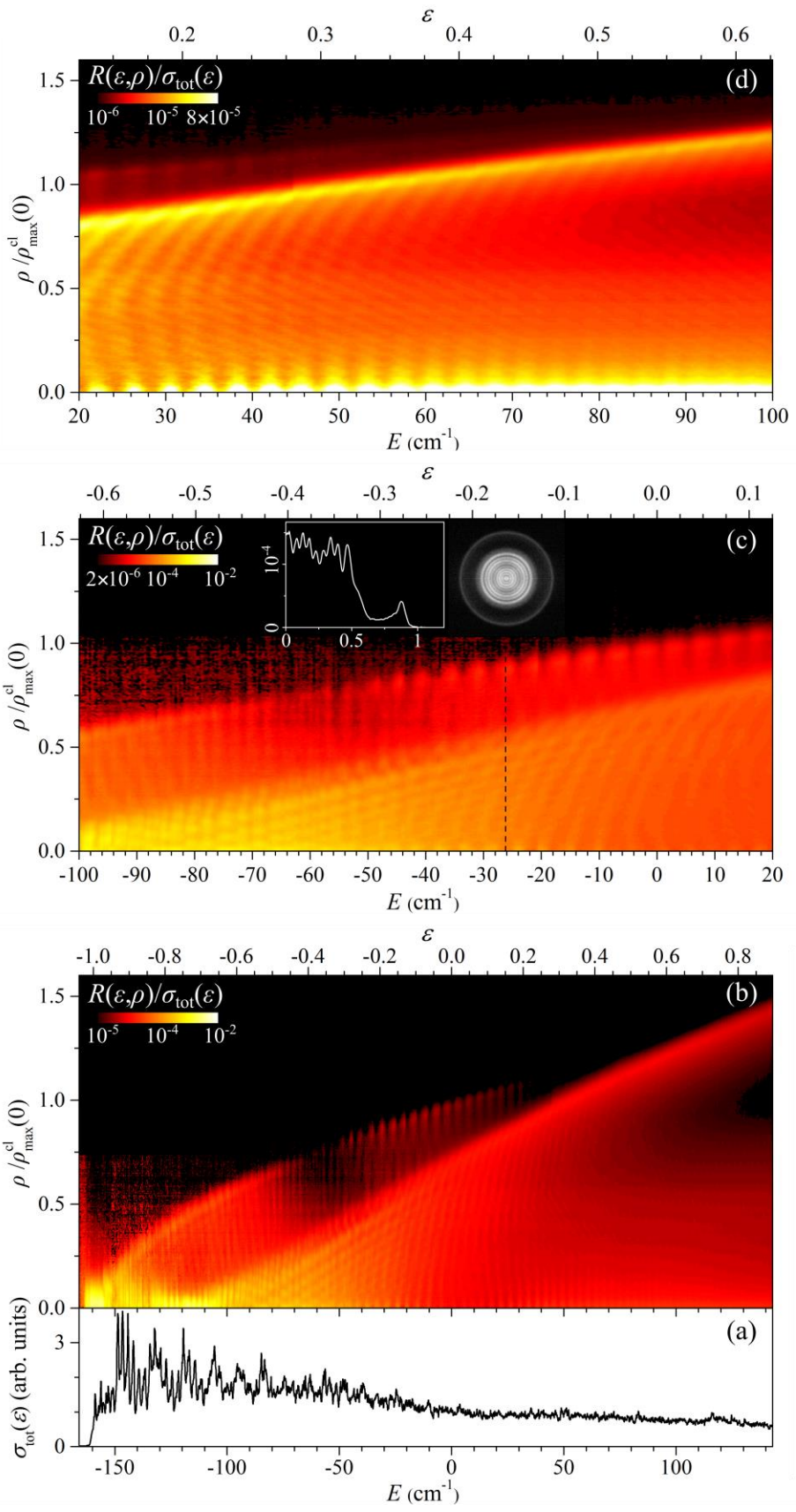
ε
R(ε,ρ)/σtot(ε)
10-6 10-5 8×10-5
(d)
ρ /ρcl max (0)
E (cm-1)
ε
R(ε,ρ)/σtot(ε)
2×10-6 10-4 10-2
(c)
ρ /ρcl max (0)
E (cm-1)
ε
R(ε,ρ)/σtot(ε)
10-5 10-4 10-2
(b)
ρ /ρcl max (0)
(a)
σtot(ε) (arb. units)
E (cm-1)

Figure 41. (a) Experimental total two-photon excitation (π-polarization) cross section of Mg out of its $3s^2$ ground state and under the presence of an $F = 680 \pm 10$ V/cm static field. The scan covers the range -165 cm$^{-1} \leq E < +145$ cm^{-1} ($-1.03 \leq \varepsilon < +0.91$, shown in the upper axis). Positive energy SFIS resonances are not observed, because their small modulation depth is comparable to the signal's noise. (b) Scaled radial distribution contour map $R(\varepsilon,\rho)/\sigma_{tot}(\varepsilon)$, in the energy range of (a). The noise of the radial distributions is enhanced near $\varepsilon \sim -1$ due to the quasi-zero $\sigma_{tot}(\varepsilon)$ values, in the same energy range and the logarithmic color-scale of the graph. The radius ρ (y axis) is scaled to ρ_{max}^{cl}, in (b-d). (c) Negative energy detail of (b) featuring the checkerboard structure and the secondary-bow and glory signal oscillations. The inset shows an image at a given energy (vertical black dashed line) and the corresponding radial distribution, where beating effects leading to magnitude modulation of the finer fringes are clearly observed. (d) Positive energy detail of (b) where the secondary-bow and glory signal oscillations are again visible.

Due to the small energy step employed for the measurements, the recording of the map was accomplished within several days. Each scan part overlaps with the previous by a number of ~3 images for the same day or ~15 images for different days. The connection between two image series parts is based on the comparison between the images from these two parts. The Mg^+ ions signal (Figure 41(a)) exhibits a series of almost equidistant spectral lines build upon a slowly varying background signal as expected (see discussion in 3.1.1). Special care was taken to record unsaturated electron and ion signals, by keeping the laser intensity to the lowest acceptable level (pulse energy <100 μJ, pulse intensity $<10^{10}$ W/cm^2). However, we were unable to avoid a small gradual decrease of pulse energy with time. For avoiding map magnitude variations attributed to this drift, each experimental radial distribution $R(\varepsilon,\rho)$ is scaled by the total electron signal. Thus, Figures 41(b)–41(d) do not actually show $R(\varepsilon,\rho)$, but the quantity $R(\varepsilon,\rho)/\sigma_{tot}(\varepsilon)$. By comparing non-scaled to scaled parts of the maps we have verified that this operation does not affect the details of the interference and beating patterns. This is also true for the calculated hydrogenic maps and an example will be given in the calculated hydrogenic maps (an example will be given below).

The nature of quantum interferences differs for different parts of the maps. These parts, therefore, deserve a separate discussion. Let us first discuss the zone of Figure 41(b) defined by $0 \leq \rho \leq \rho_{max}^{cl}$,$-1 \leq \varepsilon \leq \varepsilon_{dir} \approx -0.775$ and $\rho_I \leq \rho \leq \rho_{max}^{cl}$ for $\varepsilon \geq \varepsilon_{dir}$, for which the interference pattern is attributed exclusively to the indirect contribution. In this map zone, the faint and low contrast of inner bright fringes for the indirect contribution makes their observation difficult (also due to the logarithmic signal color-scale). This characterizes the $m = 0$ magnesium images recorded by two-photon excitation and cannot be generalized as was shown in the subsection 3.1.2, where the fringes were easily resolved for the $|m|=2$ final state case. However, channel transformations to continua, cause the variation of the outer turning point radii and they are also responsible for an

accompanying quasiperiodic intensity variation of the corresponding radial distributions. Moreover, the channel opening oscillations are quite apparent over the whole indirect contribution. Using scattering terminology [52], we may describe this effect as indirect-bow oscillations. Furthermore, this part of the map is characterized by a slanted quasi-nodal line (or surface) near -50 cm^{-1}, which create some sort of discontinuity in the behavior of the outer distribution radius as a function of energy.

Let us now turn our attention to the most interesting parts of the maps, $\varepsilon \geq \varepsilon_{\mathrm{dir}}$ and $\rho < \rho_{\mathrm{I}}$, which exhibit much more complicated quantum interference patterns. The latter reflect the coexistence and subsequent beating effects between direct and indirect contributions, each one characterized by its own fringe "frequencies." Note first the strong quantum oscillations along the classical primary-bow radius ρ_{I}. Hence, there is no clear boarder between indirect-only and direct-plus-indirect regions. One of the most striking feature is the intense beating pattern observed within the -100 cm$^{-1} \leq E \leq -20$ cm^{-1} ($-0.6 \leq \varepsilon \leq -0.1$) range, which resembles a checkerboard. This range is shown in more detail in Figure 41(c). At higher energy the checkerboard structure is much less intense and evolves to various beating fringe systems (or lines—see Figs. 39(c) and 39(d)), which are expected to be atom-, initial state-, and excitation scheme-dependent. At $\varepsilon > 0$ we may identify in Figure 41(d) a typical system of slanted fringes. Another positive energy feature of the magnesium map concerns the strongly oscillating glory ($\rho = 0$) signal (see Figure 41(d)). Certainly these oscillations are related to SFIS resonances [53,61], despite the fact that the resonances themselves are not evident in $\sigma_{\mathrm{tot}}(\varepsilon)$ (Figure 41(a)), apparently due to their poor contrast. As mentioned above, the "frequency" of the glory signal has been employed for estimating the field strength. To that purpose we made use of the fact that the cross-section "frequency" is the same for either hydrogen or non-hydrogenic atoms [62,92] and additionally, that the (dephased) oscillations of the glory signal and the total cross section have about the same field-dependent "frequency" difference for either hydrogen or non-hydrogenic atoms in the positive energy range. Interestingly, however, the magnesium map shows an additional beating pattern of curved, quasi-vertical beating lines, persisting also to positive energies. The visual effect of these fringes can be noticed in the image and corresponding radial distribution given in the inset of Figure 41(c). They are responsible for the amplitude modulation of the finer fringes of the image.

To compare with the magnesium experimental map, theoretical maps were computed for a field $F = 680$ V/cm and within the energy range $-1 \leq \varepsilon \leq +1$. To facilitate the discussion, we

employ solely $m = 0$ initial and final states (π-polarization). The detector is placed at $\upsilon_{det} = 1000$ a.u. Figure 42 and Figure 43 show the total cross sections $\sigma_{tot}(\varepsilon)$ and maps $R(\varepsilon,\rho)$ for, respectively, single-photon excitation out of the $|1,0,0,0\rangle$ ground state (Figure 42) and two-photon excitation out of the ground state (Figure 43). As it is observed, for $-1 < \varepsilon < 0$, $\sigma_{tot}(\varepsilon)$ is characterized by a non-resonant background exhibiting an occasional steplike increase and by superimposed resonances. These so-called tunneling states (TS) [53,61] are of various spectral widths, reflecting their lifetime and tunneling probability. On the contrary, for positive energies $\sigma_{tot}(\varepsilon)$ is characterized by oscillations which are attributed to the static-field-induced-states (SFIS) (see Eq. (69) and the discussion therein). The contrast of these oscillations depends on the initial state and excitation scheme [27]. For example, it appears to be larger for the single-photon excitation than for the two-photon excitation out of the ground state.

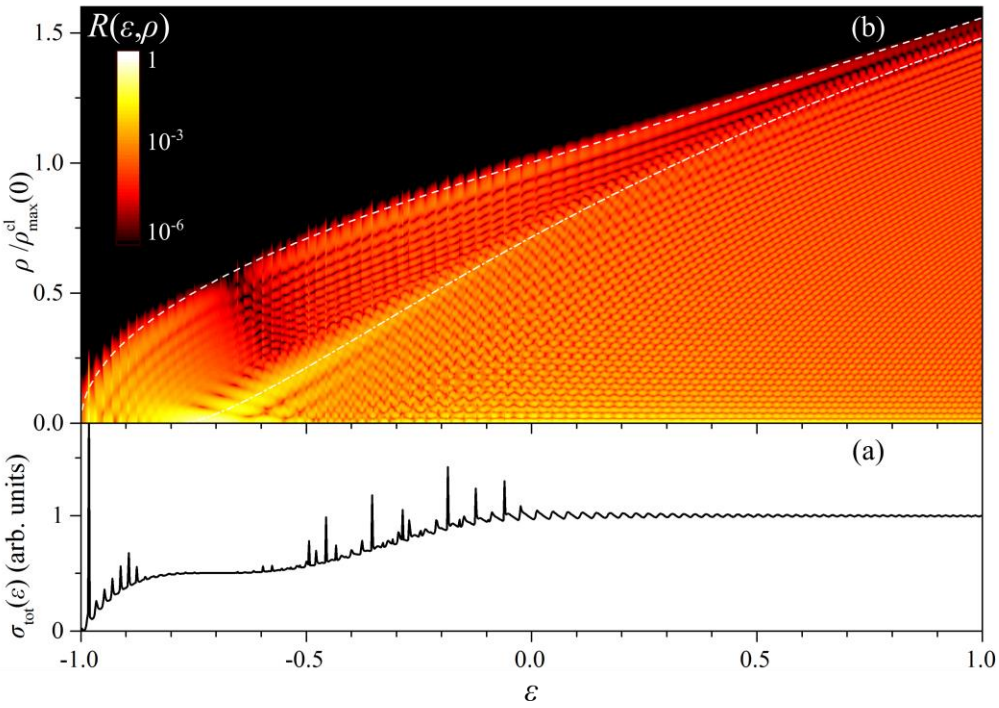

Figure 42. (a) Hydrogenic total cross section within the $-1 \leq \varepsilon \leq +1$ range and $F = 680$ V/cm for single-photon excitation of the $|1,0,0,0\rangle$ ground state to $m = 0$ final states. (b) Logarithmic-scale contour map of the radial distribution $R(\varepsilon,\rho)$ computed for the above field and $\upsilon_{det} = 1000$ au. The classical maximum radius ρ_{max}^{cl}, (white dashed line) and primary bow radius ρ_I (white dashed-dotted line), are also drawn. The map radius ρ is scaled to $\rho_{max}^{cl}(\varepsilon=0)$.

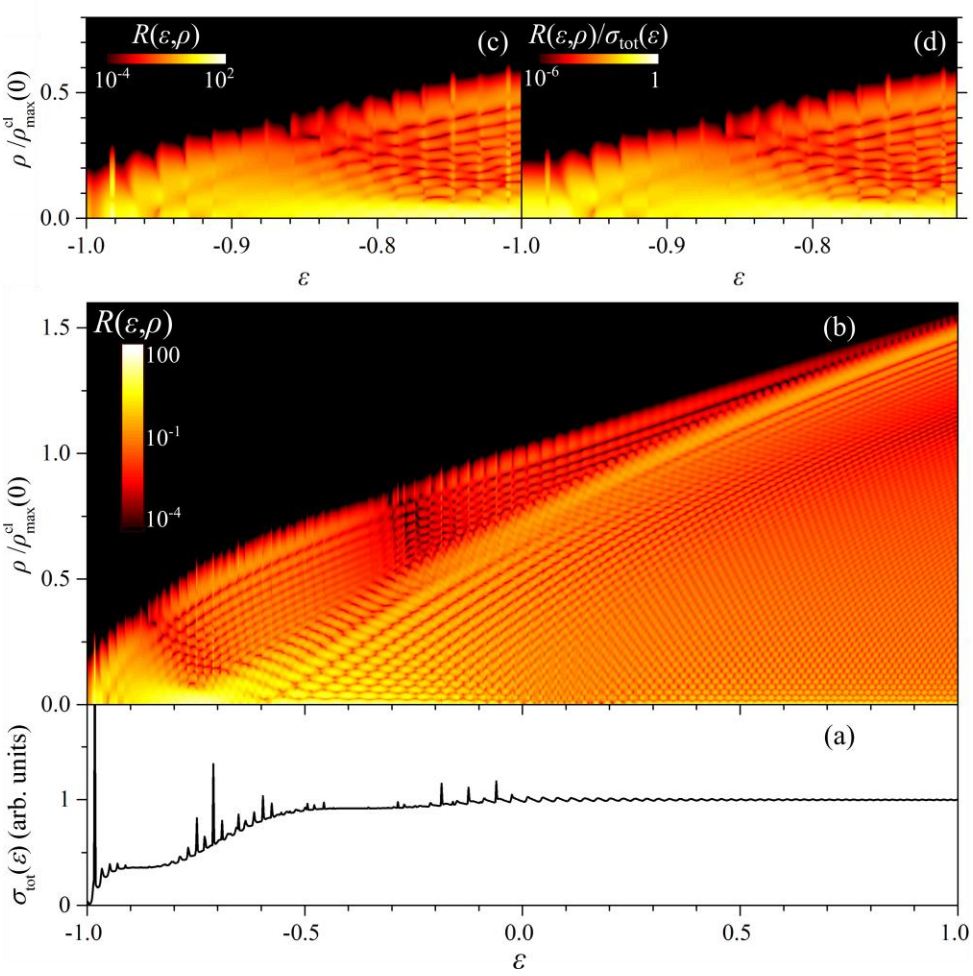

Figure 43. (a) Hydrogenic total cross-section and (b) logarithmic-scale contour map of $R(\varepsilon,\rho)$for the same field and υ_{det} as in Figure 42, but for two-photon excitation out of the $|1,0,0,0\rangle$ ground state. (c) Detail of the map of (b) within the $-1\leq\varepsilon\leq-0.7$ range. The map radius ρ is scaled to $\rho_{max}^{cl}(\varepsilon=0)$. (d) The scaled radial distribution map $R(\varepsilon,\rho)/\sigma_{tot}(\varepsilon)$ for the same range of (c). The scaling slightly affects the n_1-channel opening structures near $\varepsilon\sim-1$ and reduces the strength of resonant manifestations. However, it leaves unaltered the non-resonant fringe patterns over the whole map.

The radial distributions of TS exhibit much larger radial extensions as compared to continuum Stark states (see Figures 42(a) and 43(a)). The most intense of these negative-energy TS resonances are visible in the maps of Figures 42(b)–43(b). This is not so obvious for the weaker ones, due to the logarithmic false color magnitude scale of the maps, used to bring out all of their details without any intensity cuts. Apart from these resonances, the general energy evolution of the radial extensions of the maps evidently presents features of classical origin. This is shown in Figure 42(b) by drawing the maximum radius of impact ρ_{max}^{cl} and the primary-bow radius ρ_I of

the direct contribution [16,50,52]. In fact, we also scale the radius ρ by employing the aforementioned 1.01 ratio between the outermost turning point (ρ_{II}) and $\rho_{max}^{cl}(\varepsilon=0)$. However, the quasiperiodic stepwise increase of the non-resonant outer turning points of $R(\varepsilon,\rho)$ exhibited also in the experimental map (Figure 41(b)) is seen to persist over the whole $-1 \leq \varepsilon \leq 1$ range. These oscillating outer-turning-point radii differ from ρ_{II} ($\varepsilon\approx0$) or $\rho_{max}^{cl}(\varepsilon\approx0)$ by at most 0.5%.

The indirect interference pattern is resolved in the hydrogenic map zone between $0 \leq \rho \leq \rho_{max}^{cl}$ for $-1 \leq \varepsilon \leq \varepsilon_{dir}$ and $\rho_I \leq \rho \leq \rho_{max}^{cl}$ for $\varepsilon \geq \varepsilon_{dir}$. This pattern is rather simple and, excluding the resonant effects, it basically reflects the nodal structure of the dominant continuum n_1 channel at a particular energy. This structure is further modulated by the aforementioned channel transformations to continua, which, as in the magnesium case, do not cause solely the variation of the outer turning point radii, but they are also responsible for an accompanying quasiperiodic intensity variation of the corresponding radial distributions. The indirect contribution is quite intense at $\varepsilon \sim -1$ and gradually becomes fainter as energy increases. We may notice in Figure 42(b) that there is a single $\rho > \rho_I$ nodal line located within the $-0.8 \leq \varepsilon \leq -0.6$ range, while in Figure 43(b) we observe two nodal lines located at at $\varepsilon\approx -0.8$ and $\varepsilon\approx-0.3$. The origin of this indirect-waves-only cancellation effect is at present not fully understood. Nevertheless, since all computed maps deal with the same final Stark states, it is obvious that it should be attributed entirely to the energy evolution of the magnitudes of the relevant excitation matrix elements [27]. This interpretation explains the absence of these quasi-nodal lines in semi-classical hydrogenic PM simulations where, as formulated so far [34], excitation matrix elements are not considered.

Now we turn our attention to the inner, $\varepsilon > \varepsilon_{dir}$ and $\rho < \rho_I$ region of the map, which is dominated by complicated quantum interference patterns. The absence of a sharp ρ_I boarder is additionally noticeable and ρ_I serves merely for guiding the eye. Moreover, the gradual transition from the one map range to the other differs in the maps of Figures 42(b) and 43(b) i.e. for different excitations schemes. The same holds for the various fringe systems which are formed. Also observed, is the checkerboard structure within the $-0.6 \leq \varepsilon \leq 0$ range and as hydrogenic theory and magnesium experimental results imply, if the checkerboard structure is clearly formed, it always appears within the same ε range. Similar structures were observed in recent theoretical calculations [53] and were attributed mainly to the presence of SFIS states. Due, however, to the extreme static fields employed in that work (F = 0.03−0.1 a.u.), most of the presently revealed details were usually washed out. Nevertheless, the $\varepsilon > 0$, $\rho = 0$ oscillating glory signal (see Eq. (72)) persists

also in our weak fields and it is indeed related to the positive energy oscillations of $\sigma_{tot}(\varepsilon)$ attributed to SFIS. However, although the quasi-periodicity of cross-section oscillations and glory oscillations is practically identical, a closer look reveals that the two signals are dephased and, moreover, that their phase difference varies with energy. This is easily explained by a comparison between Eqs. (69) and (72), which shows that, unlike $\sigma_{tot}(\varepsilon)$, the glory signal is not simply related to the energy-varying transition matrix elements, but it additionally contains important information on the wave function phase.

Finally, note that the scaling shown in Figure 43(c,d) ($R(\varepsilon,\rho) \rightarrow R(\varepsilon,\rho)/\sigma_{tot}(\varepsilon)$) slightly affects the n_1-channel opening structures near $\varepsilon \sim -1$ and reduces the strength of resonant manifestations. However, it leaves unaltered the nonresonant fringe patterns over the whole map. The scaling slightly diminishes the visibility of the steplike outer radius increase for $\varepsilon \sim -1$ and reduces the importance of tunneling resonances. Yet, the manifestation of such resonances in magnesium is restricted to the vicinity of the saddle point energy. Thus, the experimental map of Figure 43(b–d) presents the main features of $R(\varepsilon,\rho)$ despite the division with the total cross section.

3.2.2 Glory and Rainbow Signals

Here we turn our attention to the critical effects of classical origin exhibited by the $R(\varepsilon,\rho)$ maps presented in subsection 3.2.1. More specifically, we examine the oscillations of the glory intensity as compared to the appearance of Stark resonances and quantization in the ionization continuum. An atom placed in a static electric field appears to be one of the very few quantum systems where, an infinite series of resonances (quasi-discrete states) can be supported in principle at any arbitrarily large positive energy. Expectedly the intensity of the glory oscillations vanishes with increasing energy. However, glory undulations are visible in photoionization microscopy thanks to the concentration of a strong signal over a limited region, distinguishable even when SFIS resonances are no longer emerging from the background noise of the total ionization cross section.

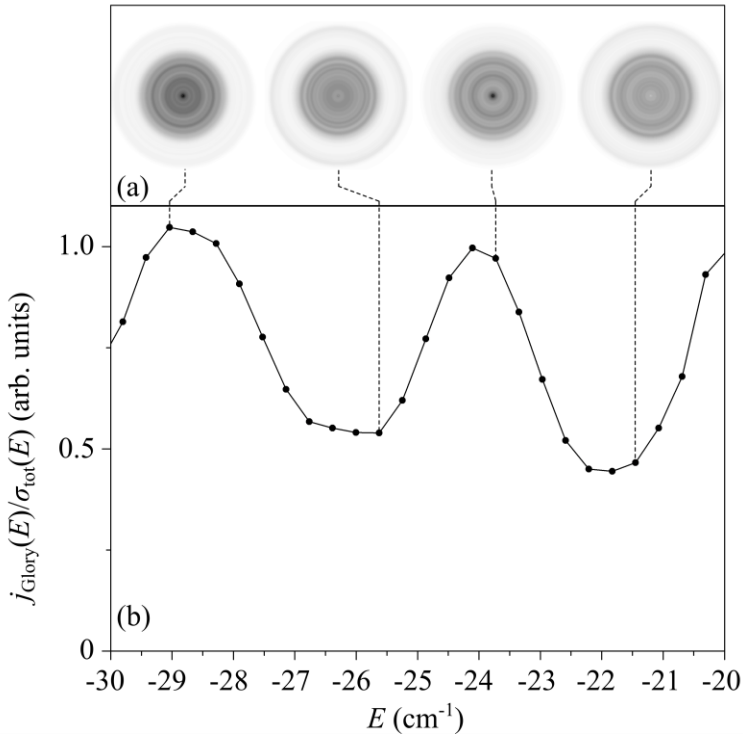

Figure 44. (a) Magnesium experimental symmetrized images recorded for F=680 V/cm The m=0 final states are two-photon excited out of the Mg ground state. These images have been presented in Figure 41 while these selected characteristic images show alternate maxima (images (a) and (c)) or minima (images (b) and (d)) at the center of the image (glory). (b) The variation of the glory intensity over the total electron signal in the corresponding energy range. For the glory the image intensity is integrated over a radius of 2% of $\rho_{max}^{cl}(\varepsilon=0)$. The graph reveals a maximum-to-minimum ratio of about ~2..

The above signatures of classical critical effects were experimentally observed at several instances [18,21,22,24,27,34]. They are also clearly imprinted in the presently acquired images, a sample of which is given in Figure 44(a) and concern near-threshold photoionization of Mg atoms in the presence of a static electric field. Apart from the quantum interference and beating phenomena that were previously discussed, quite noticeable is the intensity modulation of the glory signal as a function of the energy. In fact, this is more clearly observed in the plot of Figure 45(b) that includes the full set of measurements within the corresponding fraction of the full "glory spectrum". It is also interesting to notice in Figure 44(a) the similar intensity modulation of the outer (rainbow) image ring, where at this energy range bright rainbow signals occur when the glory intensity exhibit minima and vise-versa (although this cannot be generalized).

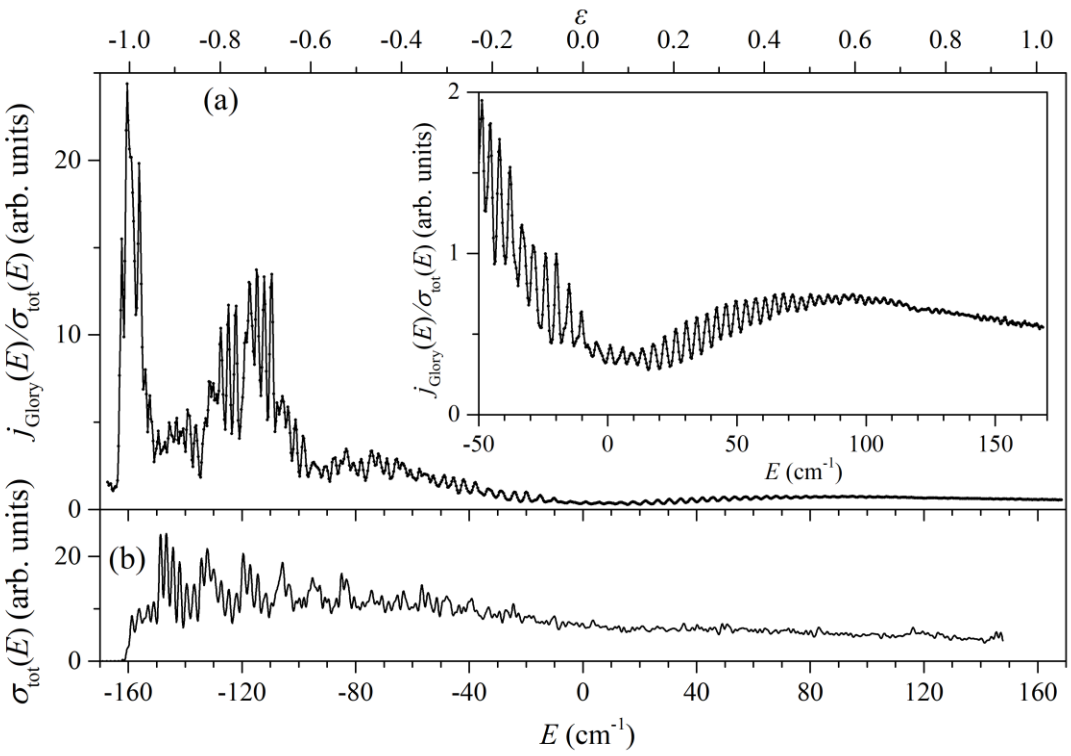

Figure 45. Glory scaled signal J_{Glory}/σ_{tot} as in Figure 44 but for the whole energy range -165 cm$^{-1}\leq E<+145$ cm^{-1} ($-1.03\leq\varepsilon<+0.91$, shown in the upper axis). The inset shows the positive energy detail of the curve.

Experimental images from two-photon ionization of Mg atom were recorded with the linear laser polarization parallel to the direction of the static electric field and as described in subsection 3.2.1. Consequently, only m=0 final Stark states can be excited, which allow for the emergence of the glory effect. The static field strength was estimated as described earlier [27] to be F=680±10 V/cm ($E_{sp}\approx$–159.6 cm^{-1}). The two-photon excitation energy was scanned by increments of $\Delta E\approx$0.4 cm^{-1} ($\Delta\varepsilon\approx2\times10^{-3}$), covering the full $-1\leq\varepsilon\leq1$ range. In fact, Figure 45 (a) (as well as Figure 44(b)) shows the energy evolution of the quantity J_{Glory}/σ_{tot}, i.e. of integrated electron signal within a small circle, having a radius of 2% of the maximum image radius at ε=0, divided by the integral over the whole image. The use of J_{Glory}/σ_{tot} , as well as its consequences, are described in the subsection 3.2.1. Comparison between the Mg^+ ion spectrum (Figure 45(b)) and the glory signal in the vicinity of the saddle point energy, shows that the glory signal is affected by the presence of tunnelling resonances, but the scaling helps in "decorrelating" the glory magnitude from this presence. On the contrary, it is obvious that the contrast of positive energy (SFIS) modulations is so low that it is hindered by noise and cannot be observed in σ_{tot}. Consequently, the shape and periodicity of the

$\varepsilon \geq 0$ glory undulations with energy remain unaltered by the scaling operation. The experimental glory intensity (Figure 45(a)) shows local maxima around $\varepsilon \approx -1$ and around $\varepsilon \approx -0.75$ ($\approx\varepsilon_{dir}$) and cancellations of the signal around $\varepsilon \approx -0.9$, -0.6, 0.0 and +0.8. Moreover, strong oscillations are exhibited throughout the full energy range. For $E > -50$ cm^{-1} (see Figure 45(a) inset), we observe oscillations that are almost evenly spaced locally but with a spacing decreasing smoothly with energy.

Our intention is to go beyond the classical description of critical scattering phenomena given in Ref. [52] and consider these additional features whose interpretation requires a quantum mechanical description. To this purpose we employ the hydrogenic expressions of Eq. (72) for the total cross section and Eq. (69) for the glory signal in order to qualitatively compare with experimental results regarding the non-hydrogenic Mg atom. Such a comparison is important because it allows for the distinction of those features which are of global nature from those which are specific to the examined atom and excitation scheme. Furthermore, because the rainbow radii vary with the energy and are difficult to accurately define and follow, the relevant signals are only partially discussed in connection with the glory ones. Therefore, here we focus mainly on the glory effect, because the signal at the image center is easy to define and record, its relative intensity near threshold dominates over all other image features and its observation does not require any particular performance from the imaging spectrometer.

In order to have a smoother connection with the quantum description, Figure 46(a) shows the semi-classically calculated energy evolution of the glory signal (black solid line). Here we follow the discussion presented in the theoretical subsection 1.1.3, and calculate the electron wave-function of Eq. (29) where the most frequent choice of equal weights c_j is employed. Then, we integrate the electron signal within a small circle, having a radius of 1% of the maximum image radius at ε=0. Note that the overall behavior of this quantity is practically identical for smaller or slightly bigger radii. Also shown is the classical glory signal (black dashed line) (see Eq. (25) and the discussion therein), which presents a similar gross energy dependence with its semi-classical counterpart. Note that, the semi-classical curve is characterized by undulations of appreciable amplitude and intense beating effects, while the “carrier frequency” of these undulations is field strength- and energy-dependent.

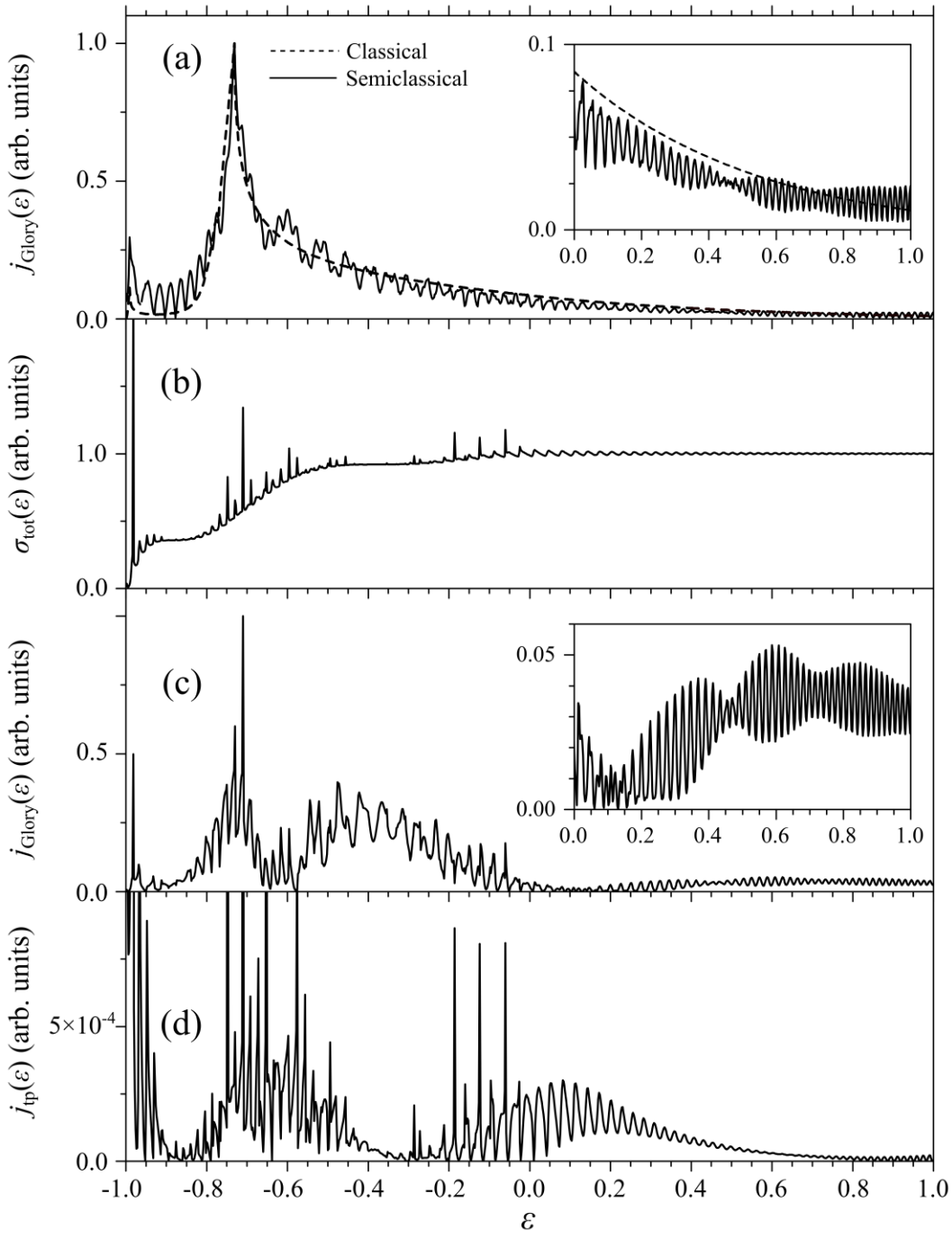

Figure 46. (a) Classical and semi-classical calculations of the glory signal. Hydrogenic total cross-section (b) and glory signal (c) for the same field and υ_{det} as in (a). (d) Signal of each image on the maximum classical radius $J_{\mathrm{det}}(\varepsilon, \rho=\rho_{max}^{cl})$. The curves of (c,d) are extracted from the map given in Figure 43(b).

Quantum calculations for the H atom are presented in Figure 46(b–d). We employ a two-photon excitation scheme out of the ground state, for F=680 V/cm and the detector placed at 2000

a.u. Evidently, the quantum glory calculation (Figure 46(c)) shows local overall maxima around $\varepsilon = -1$ and (mainly) around $\varepsilon = \varepsilon_{dir}$ and oscillations with practically the same "carrier frequency" as the semi-classical curve. The quantum beating structures, however, are apparently much more complicated and richer, occasionally comprising almost complete cancellations of the glory signal. As it may be understood by a simple comparison with the total cross section of Figure 46(b), this should be partly attributed to the inclusion of resonances which are absent in either the classical or semi-classical calculations. Nevertheless, even without the presence of tunneling states the differences would persist because of the non-equal weighting of the contributing waves (contrary to the semi-classical result). In fact, the weights in Eq. (72) are decomposed to the smooth normalization factors $A_{X,n_1,0}$ which are independent of the excitation process and the energy-dependent transition matrix elements $d_{n_1,0}$, which make the detailed structure of the glory signal initial state- and excitation scheme-dependent. This has been fully verified by quantum glory computations for single-photon excitation from the ground and low-lying hydrogenic states.

Oscillations as a function of energy and rich beating structures may be also exhibited by the bow signals. This is evident in Figure 46(d), showing the computed secondary bow signal, which, it is here defined as $J_{BOW}=R(\varepsilon, \rho_{max}^{cl})$ (see Figure 42(b)) instead of $R(\varepsilon,\rho_{II})$. Interestingly, the information provided by J_{BOW} on quantum interferences appears to be as profound as to that of J_{Glory}. It is also remarkable that the range $-0.2< \varepsilon <+0.2$ is characterized by an intensity beating maximum of J_{BOW} and a beating minimum for J_{Glory}, thus reproducing qualitatively the behavior noticed in Figure 44(a). As mentioned earlier, however, J_{BOW} presents some drawbacks. First, it is difficult to define and follow the energy evolution of ρ_{II}. This is by-passed here by defining $\rho_{II}\approx\rho_{max}^{cl}$. Note that the J_{BOW} quantity probes intensity variations of the current density and is not to be confused with the the non-smooth energy evolution of ρ_{tp} [27,70]. Second, the secondary bow signal (as all bow signals) is quite weak as compared to the glory intensity. It is due to the above reasoning that we focus our attention here mainly to the glory signal and make only qualitative comparisons with the rainbow ones.

Let us now focus on the most interesting energy range around $E=0$ ($-60\leq E \leq+100$ cm^{-1}) and present our experimental Mg results together with the two photon hydrogenic calculations in Figure 47. Note first that the comparison of the total cross sections of Figure 47(a) is inconclusive. The resonances exhibited by the hydrogenic spectra within the negative energy range are not expected to be present in the multielectron data and vise-versa. Moreover, the positive energy SFIS

resonances are not observed in the Mg curve due to their small amplitude as compared to the experimental noise. Nevertheless, for non-hydrogenic atoms the periodicity of SFIS is predicted to be the same as for the hydrogenic case, but the modulation may be in- or out-of phase with respect to that of hydrogen, depending on the values of the quantum defects of the zero-field Rydberg states for the particular atom [62,92]. The small SFIS amplitude is also a characteristic feature in the case of the two-photon excitation scheme of the hydrogenic total cross section calculations (see also the discussion in subsection 3.2.1).

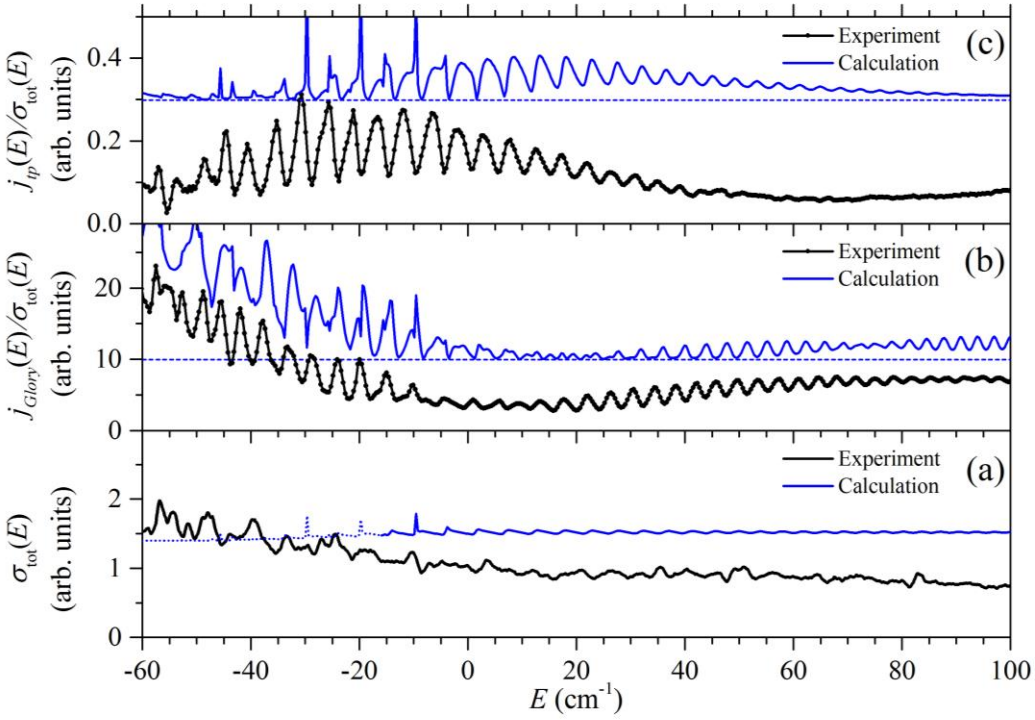

Figure 47. Comparison between experimental measurements and hydrogenic quantum mechanical calculations. The experimental measurements concern the Mg PM images of m=0 final states, excited via a two-photon excitation scheme out of the Mg ground state. Hydrogenic calculations are performed for two-photon excitation out of the H ground state. F=680 V/cm and υ_{det}=2000 au. (a) Total cross sections in common arbitrary scale. The SFIS states are visible but with a low contrast on the calculations while they are hidden within the noise for the experimental data. (b) Glory signal normalized over σ_{tot} and obtained by following the same procedure in both experimental and calculated images (integration over the circle with radius ρ=2% of $\rho_{max}^{cl}(\varepsilon=0)$). (c) Primary rainbow signal obtained by the $R(\varepsilon,\rho)$ maps as $J_{tp}(\varepsilon)=J_{det}(\varepsilon, \rho=\rho_{max}^{cl})$.

On the other hand, the theory-experiment comparison is striking (apart from the hydrogenic resonant features on the negative energy range) for the glory and primary bow signals of Figure 47(b,c) respectively. First, the cancelations/maximizations of the glory/rainbow signal occur around the same energy locations for both H and Mg and are qualitatively similar. In fact, Mg data exhibit those features at slightly lower energies that, considering our hydrogenic calculations for different excitation schemes, imply their matrix-element-dependence. The "carrier" frequencies of both Mg glory and bow intensity oscillations are almost equal to their hydrogenic counterparts apart an almost constant phase difference. More specifically this frequency for the Mg glory signal varies smoothly with energy and the spacing between maxima is $\Delta E \approx 4.5$ cm^{-1} for $E \approx 0$ and $\Delta E \approx 3.0$ cm^{-1} for $E \approx 100$ cm^{-1}. The magnesium-hydrogen frequencies similarity is indeed to be expected in the positive energy range where the PM observables present global and nearly-atom-independent features.

As discussed above, the Mg experimental data do not allow for a comparison between the positive energy dependence of the total photoionization cross-section and the glory signal. Nevertheless, the hydrogenic calculations show that the evolutions of these two quantities at positive energy are highly correlated. Let us first try to firmly establish this correlation between the glory oscillations of J_{Glory} and those of σ_{tot} within the semi-classical framework. Then, any departure from these semi-classical predictions should be attributed to atom-, initial state- and excitation scheme- specificities of these signals. We begin by simulating the periodicity of the total cross section using the phase relations of Eq. (31) and the quantization condition of Eq. (30). Then, the carrier phase of the SFIS signal may be defined as, $S_T = 2S'_\chi(\varepsilon) - \pi$. The carrier phase of the glory signal has already been defined in Eq. (32). Now by setting $S_{GT}=S_G-S_T$ we finally proceed to the definition of the number of additional oscillations A, exhibited by J_{Glory} the with respect to the SFIS number of oscillations and within the energy interval $[0,\varepsilon>0]$,

$$A(\varepsilon) = (2\pi)^{-1}[S_{GT}(\varepsilon \gg 1) - S_{GT}(\varepsilon = 0)] \,. \tag{110}$$

In fact, as defined, A equals zero at $\varepsilon=0$. Figure 48 presents these excess of glory oscillations as a function of energy. Two y-scales have been employed in the graph, one directly given by the above definition of Eq. (110) and one scaled by the field strength, $A^{scaled} = F^{\frac{1}{4}}A^F$.

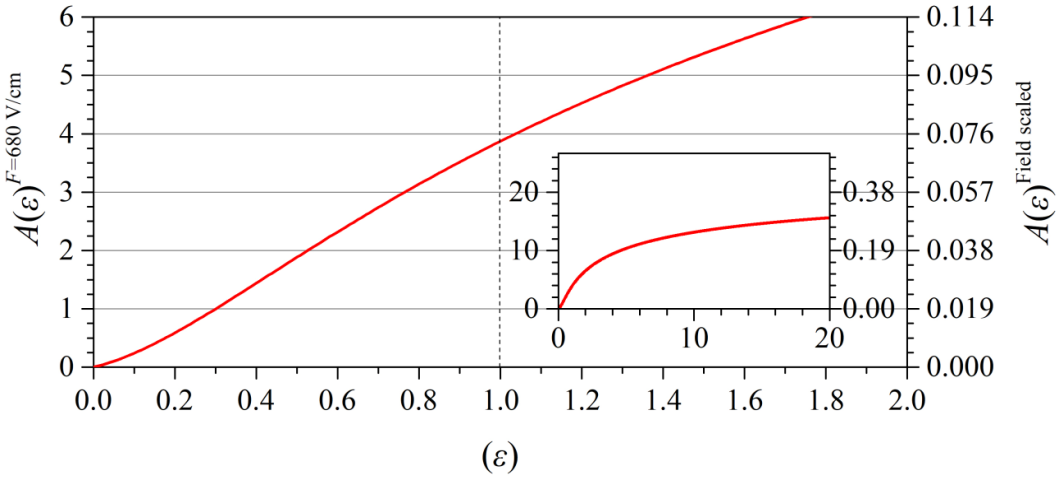

Figure 48. Number of additional glory oscillations with respect to the number of SFIS states ($A(\varepsilon)$) for the positive energies, as given in Eq. (110). In fact, A is defined as the difference between the glory phase (S_G of Eq.(32)) and the total cross section SFIS phase ($2S'_\chi(\varepsilon) - \pi$, see Eq.(30)), after dividing each one of them by 2π. The values $v_{det}\rightarrow\infty$ and F=680 V/cm were adopted for the calculation. Nevertheless, the y-axis can be nominally scaled with the static field value as $A^{scaled} = F^{\frac{1}{4}}A^F$ (right side). The inset shows the number $A(\varepsilon)$ of additional oscillations at extremely high positive energies. The maximum y-axis range of this inset is equal to $A^{scaled}(\varepsilon\rightarrow\infty)\approx 0.508734$.

This relation is compatible with the coincidence of SFIS and Glory maxima observed in the work of [53] due to the extreme field strengths that were employed. Figure 48 in conjunction with the fully quantum calculations of Figures 46 and 47, show that the glory and total signal oscillations can be well predicted by a simple semi-classical description. Indeed, comparing with the fully quantum mechanical calculations of Figure 47 we see that the additional glory oscillations are are to a good approximation equal to the semi-classically predicted value $A^{F=680\ V/cm}(\varepsilon=+1)=3.85$. This fact proves that, for positive energies, the gross features of the glory and total signal oscillations can be calculated without considering matrix elements which bring excitation specificities into play. This result points towards more accurate descriptions that will identify atom specific effects due to additional phase shifts manifested in the intensity beating positions.

As a final task, let us connect these findings with the electron dynamics of the system. Oscillations of the current density maps $R(\varepsilon,\rho)$, were recently connected to time delays of arrival at the detector between pairs of electron trajectories, by using the Eisenbud-Wigner time delay definition (see Eq. (33)). The proposed treatment involves the selection of a given constant radius and the measurement of the energy difference ΔE between successive maxima observed at this

radius. Obviously, the phase difference between these two maxima is $\Delta S \equiv 2\pi$. Then, the resulting time delay Δt is compared with the classically calculated time delay of the most relevant pair of trajectories [34]. Here we extend these considerations to the ρ=0 case i.e. to the glory signal. This selection of ρ, apart from the practical advantages mentioned above, introduces an additional simplification to the calculations. Assume, for example, that one is interested in calculating the Eisenbud-Wigner time delay for F=680 V/cm, around ε=0 and for a scaled radius $\rho/\rho_{max}^{cl}(\varepsilon = 0)$=0.4. With the help of Figure 4(b) we could claim that for the chosen scaled radius the most relevant pair of trajectories corresponds to $\beta_1 \approx 0.85\pi$ and $\beta_2 \approx 0.4\pi$. In fact, to a first approximation this is indeed the case. Nevertheless, a third trajectory corresponding to $\beta_3 \approx 0.23\pi$ might also contribute with strength comparable to that of β_2. We remind that the trajectory strength is determined through Eq. (29) and involves the slope of $\rho(\beta)$. This problem is absent for ρ=0 where indeed one pair with $\beta_1 \approx \pi$ and $\beta_2 \approx \beta_o$, is dominant.

In order to calculate the inverse energy spacing between adjastent glory maxima (see Eq. (33)) we employ the Fourier transformation of the signal within a limited energy window and repeat the calculation over an extended energy range. For this we employ the build-in capabilities of Origin® software. As compared to the simple measurement of ΔE between successive maxima described above, Fourier analysis provides a much more detailed view of the full frequency landscape involved. In Figure 49(a-c) we present the "short time" Fourier transform of the calculated hydrogenic and experimental Mg J_{Glory} data respectively. The emerging y-(time) axis is expressed in picoseconds. The tradeoff between time and energy resolution implies that the employed energy window imposes a lower time uncertainty limit to the calculated time which, for our case is chosen to be ≈1.5 ps.

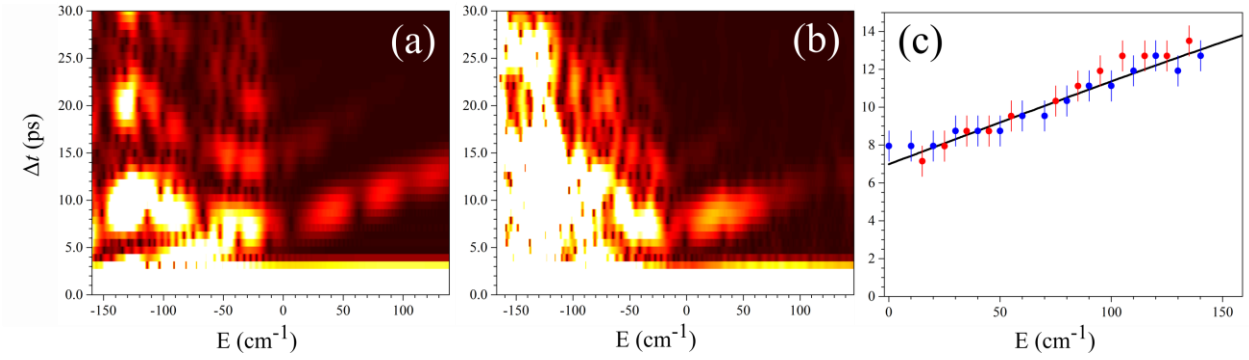

Figure 49. Linear color-scale map of the "short time" Fourier transform for the calculated hydrogenic (a) and the experimental magnesium (b) glory signals. The Fourier window (Blackman type [120]) has a width of ≈21 cm^{-1}. The vertical axes are multiplied by the factor $4\pi\, t_o\, Ryd_{Mg}$, where t_o the atomic unit of time in picoseconds and Ryd_{Mg} the mass-corrected Rydberg constant of magnesium (in cm^{-1}). (c) The primary maximum of the experimental (blue points) and the calculated (red points) short time Fourier spectra, see (a), (b) respectively. The quantum calculations are compared with the semi-classical curve (black solid line) which is obtained by differentiating the number of glory oscillations as a function of energy and multiplying with the aforementioned factor. These graphs are directly connected to the time of flight of the trajectories $\beta=\beta_0$ and $\beta=\pi$ (see main text).

The Fourier transform of the Hydrogenic J_{Glory} of Figure 49(a) shows a complex behavior for $\varepsilon<0$ and a well-organized pattern for slightly negative and positive energies. In fact, the main slanted and almost linear "moving frequency" [1] comprises of two components and presents a series of magnitude variations (minima-maxima), thus reproducing the glory beating effects. The corresponding Fourier transform of the hydrogenic σ_{tot} (not shown) exhibits a qualitatively similar behavior. As implied by the $A(\varepsilon)$ fringe excess function of Eq. (110), however, the differences in the $\varepsilon\geq 0$ range are non-negligible and measurable. This positive energy pattern is dominated by the "moving frequency" of the SFIS oscillations, the latter found to be somewhat smaller than the one corresponding to the glory signal. This is exactly what the function $A(\varepsilon)$ predicts. In fact, classical calculations show that for $\varepsilon>>1$ the SFIS and Glory periodicities coincide.

Probably the most interesting aspect of the present work is the fact that, we were able to extract the same information discussed above from the experimental glory signal of Mg, the corresponding Fourier transform of which is presented in Figure 49(b). The resolution is high enough that not only the primary (the "frequency" line found near Δt~5 ps for E~0 and Δt~15 ps for E~140), but also a secondary slanted (i.e. "moving") "frequency" to be clearly observed. Our theoretical and experimental results are summarized in Figure 49c. Each point refers to the dominant "frequency" ("frequency" with the maximum amplitude, excluding the $\Delta t<3$ ps range) of Figures 49(a,b) and for each energy window. The agreement between the H theory (red points) and the Mg experiment (blue points) is striking.

These results of the primary "moving frequencies" (time delays) are compared to the predictions (solid line) derived from the semi-classical model described in 1.1.3 and by taking into account only two trajectories, corresponding to $\beta_1\approx\pi$, $\beta_2\approx\beta_o$, respectively. In particular, the plotted

[1] The reader should keep in mind that *y*-axis "frequencies" in Figure 49(a,b) are actually expressed in time units.

curve corresponds to the derivative of the glory phase of Eq. (32) divided by 2π, i.e. $\frac{1}{2\pi}\frac{\partial S_G(E)}{\partial E}$. Interestingly, the semi-classical model shows excellent agreement with the fully quantum calculations and the experimental results. Nevertheless, it cannot reproduce the full complexity of our observations, such as the manifestation of a double dominant "frequency" (e.g. see Figure 49(a) within $0<E<10$ cm^{-1}. This implies that there may be more than two trajectories contributing to the dominant double "frequency".

Let us now make a connection between the above semi-classical analysis and the actual classically computed time of flight differences between the involved trajectories. To this purpose the arrival times (i.e. the times of flight) and their difference were calculated through Eq. (23) for the two classical trajectories corresponding to $\beta_1\approx\pi$ and $\beta_2\approx\beta_o$. These classical calculations completely validated our semi-classical (and quantum) findings. For example, for the employed field value of 680 V/cm, the two trajectories ($\beta_1\approx\pi$, $\beta_2\approx\beta_o$) have a time difference of $\Delta t\approx7.7$ ps at $E\approx16$ cm^{-1} and $\Delta t\approx13.8$ ps at $E\approx157$ cm^{-1}. These numbers are to be compared to the corresponding semi-classical results extracted from Figure 49(c) $\Delta t\approx7.7$ ps and $\Delta t\approx13.7$ ps respectively. Finally, the classical calculations show that the observed higher order slanted "frequency" lines in Figure 49(a,b) could be attributed to the time delay between other glory trajectory pairs, such as , β_1 and β_3 , and so on. Nevertheless, we have avoided here a more detailed treatment of those higher order slanted "frequencies", as well as the study of the $R(\varepsilon,\rho)$ map at constant but non-zero radii, $\rho\neq0$. Certainly, such extensions of this kind of analysis are now in order.

In conclusion, we believe that we have theoretically and experimentally established the importance of the study of the glory signal. Let us briefly comment on this conclusion. The information on the system dynamics through interferometric measurements is interesting per se. Of course, this interference persists even for high positive energies, while it can be fairly easily experimentally observed and resolved. Moreover, the Coulomb-Stark problem is one of the few that can exhibit level quantization within the continuum (SFIS) and, in principle, at arbitrarily high positive energy. The established connection between those two phenomena help us probe quantized levels to energies up to the classical limit ($\hbar\rightarrow0$).

3.3 Polarization Effects

3.3.1 Linear Laser Polarization Rotation Effects in Magnesium Images

Here we discuss the rotation of the linear ionizing-laser-beam polarization with respect to the electric field direction. Evidently Eq. (89) reveals that two-photon ionization out of an m=0 initial state allows for the population of $|m|$=0,1,2 Stark states. The resulting multiple $|m|$-presence and $|m|$-beating effects [30] in the PM images are demonstrated here theoretically for the hydrogen atom and experimentally for the magnesium atom. Note that Mg images involving $|m|$=0,2 Stark states have been presented in section 3.1.2. Our theoretical discussion as well as the analysis of subsection 3.2.1., suggests that non-resonant PM images produced by the hydrogenic theory near $\varepsilon \geq -1$ could be compared, at least qualitatively, with those recorded on non-hydrogenic atoms. As a first example experimental images recorded after two-photon ionization of ground state magnesium atoms in the presence of a field $F = 680 \pm 10$ V/cm and $\varepsilon \approx -0.76$ are presented in Figure 50. The angle between laser-ionizing-field polarization and the static field Θ is varied in the $(0, \pi)$ range, since images recorded for $\Theta' = \pi - \Theta$ are simply reversed with respect to the vertical direction. These experimental data are compared with the theoretical images of Figure 50(b), computed via two-photon excitation of hydrogen out of the ground state $|1,0,0,0\rangle$. The slightly different reduced energies at which recorded and computed images better resemble to each other, are compatible with our field uncertainty. Let us first focus on the images for which we employ either π – (m = 0 final Stark states, $\Theta = 0^o$) or σ-polarization ($|m|$ = 0 and 2 final Stark states, $\Theta = 90^o$).

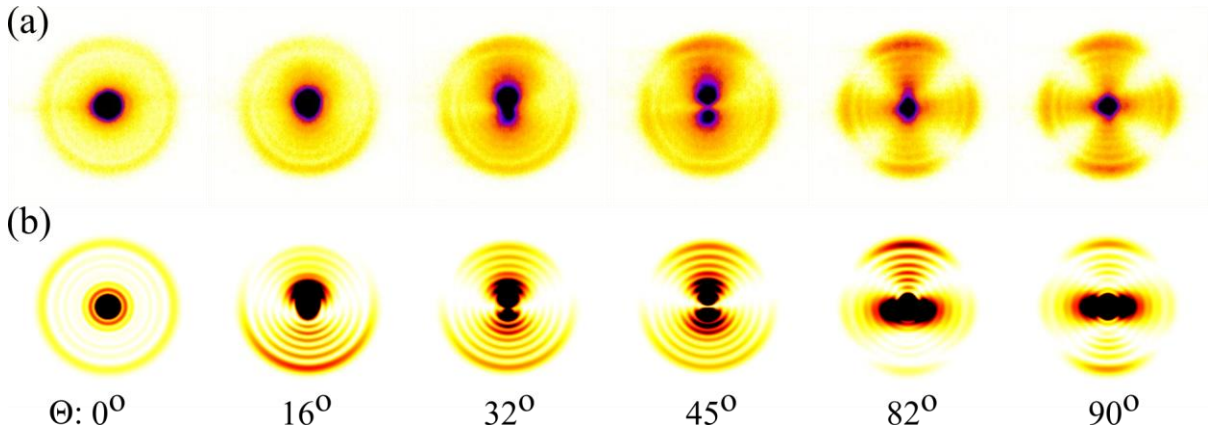

Figure 50. Comparison between non-resonant experimental magnesium images (a) and hydrogenic theoretical images (b). The horizontal and vertical axes refer to the *x* and *y* coordinates, respectively, of electron impact on the detector. The laser beam propagates along *x* axis. Mg final states were two-photon excited out of the $3s^2$ ground state for an estimated static field value F=680±10 V/cm and $\varepsilon\approx$–0.76. The hydrogenic calculation refers to two-photon excitation from the 1s ground state, for the same field, υ_{det} = 1000 au and a slightly different reduced energy ($\varepsilon\approx$–0.78), to reproduce as close as possible the experimental bright fringe intensity distribution. The light polarization vector forms an angle Θ with the static field. We have verified that the images are reversed with respect to the vertical direction for Θ'=π–Θ.

In fact, despite the different characteristics of the initial states, the π-polarization images bear many similarities, namely (i) the disc-like shape that shows no angular distribution (ii) the very intense central glory spot, (iii) a quite intense outer bright (rainbow) fringe, and, more interestingly, (iv) the rather faint and low contrast inner bright fringes. Although this last observation may not be generalized, it characterizes the m=0 magnesium images recorded by two-photon excitation, as long as the reduced energy is lower than the onset of the direct trajectories ($\varepsilon_{dir}\approx$–0.755). As for the σ-polarization images, they also have many features in common. First of all, they both exhibit the expected $\cos^2(2\varphi)$ angular dependence, which implies the dominance of the m=2 waves over the m=0 ones. Nevertheless, the m=0 contribution manifests itself in a number of ways. First, by the very bright glory signal at the center of each image, whose origin cannot be other than the m=0 waves (Eq. (72)). Second, by an m-beating effect [27,30] (see the coherent summation over different values of m in Eq. (89)), resulting to φ-dependent bright fringe intensities and radii. The effect is present in both experimental and theoretical images, but more evident in the latter ones. One may notice that for Θ=90°, the fringe pattern in the horizontal direction is different and fainter than that in the vertical one. Since, the transition matrix elements may change sign and magnitude as a function of energy, the image direction where the fringes are brighter may also change.

The m-beating effect is even more interesting for intermediate angles Θ≠0, π where the excitation of $|m|$=1 final Stark states is also permitted (see Eq.(89)) and the radial interference pattern presents a strong φ-dependence. Note that all images are symmetrical with respect to the vertical axis and only the Θ=0 images are symmetric with respect to the image center. Most of the Θ≠0, π experimental images of Figure 50(a) show a quasi-horizontal nodal axis signaling the strong $|m|$=1 contribution. These results are qualitatively similar to hydrogenic calculations of Figure 50(b). However, a fully quantitative comparison between theory and experiment is not possible due to the lower spatial resolution of the experimental images and the generally different

matrix elements expect for the multielectron case with respect to the hydrogenic one. This lower spatial resolution of the experimental image is to be expected since the computed data are not convoluted with the resolution of the detector. Such an operation was avoided because it is unnecessary for a qualitative comparison.

3.3.2 |*m*|-Decomposition of Magnesium Total Cross Section

In the previous section we studied the polarization rotation effects on the differential cross section, for a two photon transition out of a m=0 initial state. Those images exhibited the |m|-beating effect, which follows from the simultaneous excitation of different-m final states. These observations show that the static field axis is the preferable direction in space (quantization axis). Here, for providing additional experimental evidence of this fact, we aim at measuring the non-hydrogenic "densities of states" $\Delta_{l,l'}^{|m|}(E)$ in the presence of a static field (see Eq. (101)) (|m|=0,1,2) [32]. In other words, the recording of |m|-dependent "density of states" constitutes another direct proof that the static field axis is indeed the quantization axis.

Let us begin by examining the energy dependence of the differential cross section, i.e. the energy dependence of the |m|-beating effect observed in the PM images. Figure 51(a,b) shows such images recorded as a function of the excitation energy for a constant angle Θ and for F~500 V/cm.

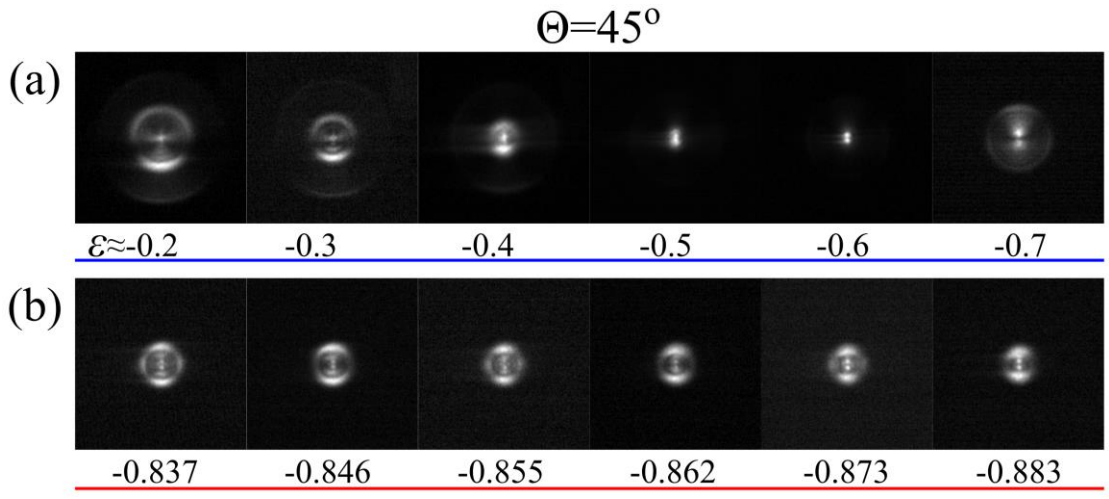

Figure 51. Experimental Mg images in the energy range ε:(–0.2, –0.7) (a) and ε:(–0.837, –0.883) (b). Magnesium final states were two-photon excited out of the $3s^2$ ground state for an estimated static field value F~500 V/cm and for $\Theta=45^o$.

The Mg final states are excited out of the Mg ground state via a two-photon transition. Fixing the angle Θ, also fixes the angular factors of Eq. (89) and allows for monitoring the (collective) energy evolution of the matrix element integrals $D^{\pi/\sigma(2)}_{n_1,|m|}$ and the phase factors $e^{i\theta^*_{n_1,|m|}}$. As we already mentioned, the form of the current density of Eq. (89) remains the same after substituting the hydrogenic integrals and phases with their non-hydrogenic counterparts. The choice of Θ is guided by the results of Figure 16, which shows that the relative contribution of $|m|=1$ states is maximized for $\Theta=45^o$. Figure 51(a) shows PM images separated by $\Delta\varepsilon$~0.1 within a broad energy range. For $\varepsilon>-0.4$, all images exhibit almost the same angular distribution and they are characterized by a quasi-horizontal nodal curve. More specifically, the angular function of Eq. (109) has the same form but, of course, the φ-dependent radial distribution evolves with the energy. This shows that as the energy increases, new open channels contribute to the interferogram but have a small impact on the general angular distribution of the image. Thus, the differences should be carefully searched within the complex and φ-dependent radial interference pattern. On the other hand, for $\varepsilon\leq$-0.5, the angular distribution of the images has a strong dependence on the excitation energy and especially for the images of Figure 51(b) for which $\varepsilon \sim -0.8<\varepsilon_{dir}$. For example, we seem to probe $|m|=1$ final states (resonances) at $\varepsilon=\{-0.846, -0.862, -0.883\}$ or $|m|=2$ ones in the rest of the given set of images.

In either the multielectron or hydrogenic case the total cross section depends solely on the matrix element integrals and not the phase factors (see Eqs.(69,97,101)). It follows that the examination of σ_{tot} would conclude whether the energy dependence of $|m|$-dependent effects observed in PM images, could be attributed on the matrix element integrals or the phase factors. For this purpose, let us now focus on the most interesting energy range $\varepsilon \sim -1$ and record the total electron signal of PM images as a function of energy and for different angles Θ. Figure 52(a) shows the two-photon spectra out of the Mg ground state for, $\Theta=0$ (π-polarization), $\Theta=90^o$ (σ-polarization) and $\Theta=\Theta_{magic}=54.7^o$, while $F\approx$750 V/cm. The observed spectral lines have a width slightly greater than expected (1 cm^{-1}). This is attributed to a weak power broadening effect which is induced by the high laser pulse energy of <200 μJ/pulse.

Based on the discussion of section 1.3.2 we ignore the $p \rightarrow s$ zero-field transitions [93] in our two-photon excitation model. Then we use the simplified Eq. (105) and the recorded spectra of Figure 52(a) in order to calculate the non-hydrogenic "density of states" $\Delta_{l=l'=2}^{|m|}(E)$, which are shown in Figure 52(b). Note first that the onset (first strong resonance) of each $\Delta_{2,2}^{|m|}$-spectrum is compatible with Eq. (27). The corresponding saddle point energies for the estimated field value, $F \approx 750$ V/cm, are: $E_{\mathrm{sp},m=0}^{\mathrm{cl}} = -167.6$ cm^{-1}, $E_{\mathrm{sp},|m|=1}^{\mathrm{cl}} = -166.0$ cm^{-1} and $E_{\mathrm{sp},|m|=2}^{\mathrm{cl}} = -164.3$ cm^{-1}. Note that $\Delta_{2,2}^{m=0}$ is proportional to the experimental spectrum $\sigma_{tot}^{(2)}(\Theta = 0^{\mathrm{o}}, E)$. Moreover, the quasi-degeneracy of $|m|=0$ and 2 states [62,65,117] is again confirmed here by visually inspecting the $m=0$ (solid black line) and $|m|=2$ (dotted blue line) curves of Figure 52(b). More interestingly, the $|m|=1$ resonances manifest themselves between the $|m|=0,2$ ones.

In order to verify the validity of the employed approximation $\Lambda \sim 0$ (see Eq. (101)), we compute a "synthetic spectrum" for $\Theta = 20^{\mathrm{o}}$ by employing the known $\Delta_{l,l'}^{|m|}(E)$ curves. This "synthetic" spectrum (dotted gray line) is constructed as $\sigma_{tot}^{(2)}(\Theta = 20^{\mathrm{o}}, E) \propto 67.99\%\, \Delta_{2,2}^{|0|} + 30.99\%\, \Delta_{2,2}^{|1|} + 1.02\%\, \Delta_{2,2}^{|2|}$ according to Eq. (105) and is shown together with an experimental one (solid black line), in Figure 52(c). The two curves are almost identical and this proves that the decomposition along these lines can be safely used for the magnesium near-saddle-point energy spectra. In fact, we also recorded Mg^+ spectra (instead of the total electron signal) for the same Θ values. The analysis of these ion spectra gave the same results and reached the same conclusions, and, therefore, they are omitted here for the sake of clarity. Note that, the $\Theta = 20^{\mathrm{o}}$ experimental spectra bears many similarities with the $\Delta_{2,2}^{|0|}$ "density of states" but the spectral lines are not so sharp due to the presence of the $\Delta_{2,2}^{|1|}$ resonances in-between of the $m=0$ ones.

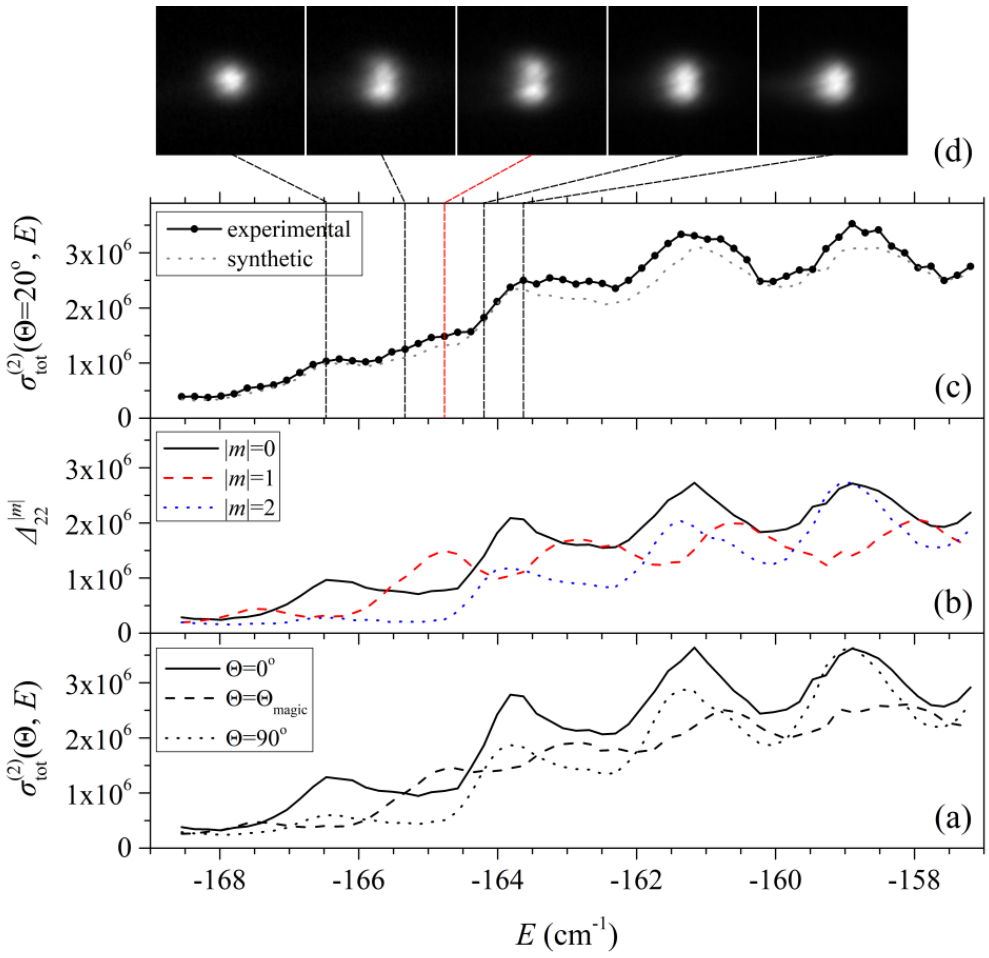

Figure 52. (a) Total integrated electron signal of PM images for F=750 V/cm and Θ=0°, Θ_{magic} and 90°. (b) The decomposed $|m|$-contributions (non-hydrogenic "matrix elements") obtained by employing the spectra of (a). (c) Recorded and "synthetic" spectra for Θ=20°. (d) PM images for the same conditions of (c) in the energy range around an $|m|$=1 resonance.

Let us now examine the images of the Θ=20° data set in Figure 52(d). The majority of the images are almost spot-like and do present faint angular dependence. On the other hand, around E= –164.75 cm^{-1} the images exhibit a horizontal nodal curve which is typical of $|m|$=1 final states. Indeed, this energy coincides with a spectral line maximum of the $\Delta^{|1|}_{2,2}$ "density of states". This verifies that the PM images probe the complete Stark spectrum of the relevant accessible quantum numbers $|m|$. This fact has been proven here by comparing the PM images and the decomposed total cross section spectra. The above discussion shows that the study of the Stark structure (particularly near the saddle-point energy) is important for probing multiple-$|m|$ excitation caused by the rotation of the laser polarization vector with respect to the static electric field. In turn, this

multiple-|*m*| excitation proves that the field axis is indeed the axis of quantization. As a consequence, the emergence of multiple-|*m*| excitation poses great challenges to the development of tomographic wave function reconstruction methods when dealing with slow electrons. We remind that the main goal of tomographic techniques is the reconstruction of the 3-dimensional electronic momentum distribution. In fact, these techniques typically assume the presence of a single electronic momentum distribution that is simply rotated in the three-dimensional space as the linear polarization vector is rotated [48,49]. Equivalently, the polarization vector is assumed to be the quantization axis. According to the above discussion, for the meV electrons energies and static field strengths considered in the present work, these typical tomographic assumptions appear to be not inapplicable.

3.3.3 Detection and Characterization of Misalignments

Generally speaking, quite complex radial patterns are not uncommon at higher energy, as evident in the maps of Figure 41. Such is the case for images recorded after two-photon ionization of ground state of magnesium ground state in the presence of a field $F = 680 \pm 20$ V/cm and $\varepsilon \approx -0.4 > \varepsilon_{dir}$ (Figure 53(a)) Apart from the different excitation energy and the appearance of the direct fringe system as Θ is varied within the $[0, \pi]$ range the images exhibit the aforementioned characteristics of Figure 50(a). On the other hand, most of the images do not show vertical axis symmetry, but they are “tilted” with respect to it. This tilt possibly stems from misalignment of the ionizing beam with respect to the plane normal to the static field. In fact, this image set is selected to highlight these features. Misalignment effects were already discussed in subsection 1.3.1 and here we are able to calculate all the relevant angles via the use of the barycenter coordinates of Eqs. (94,95).

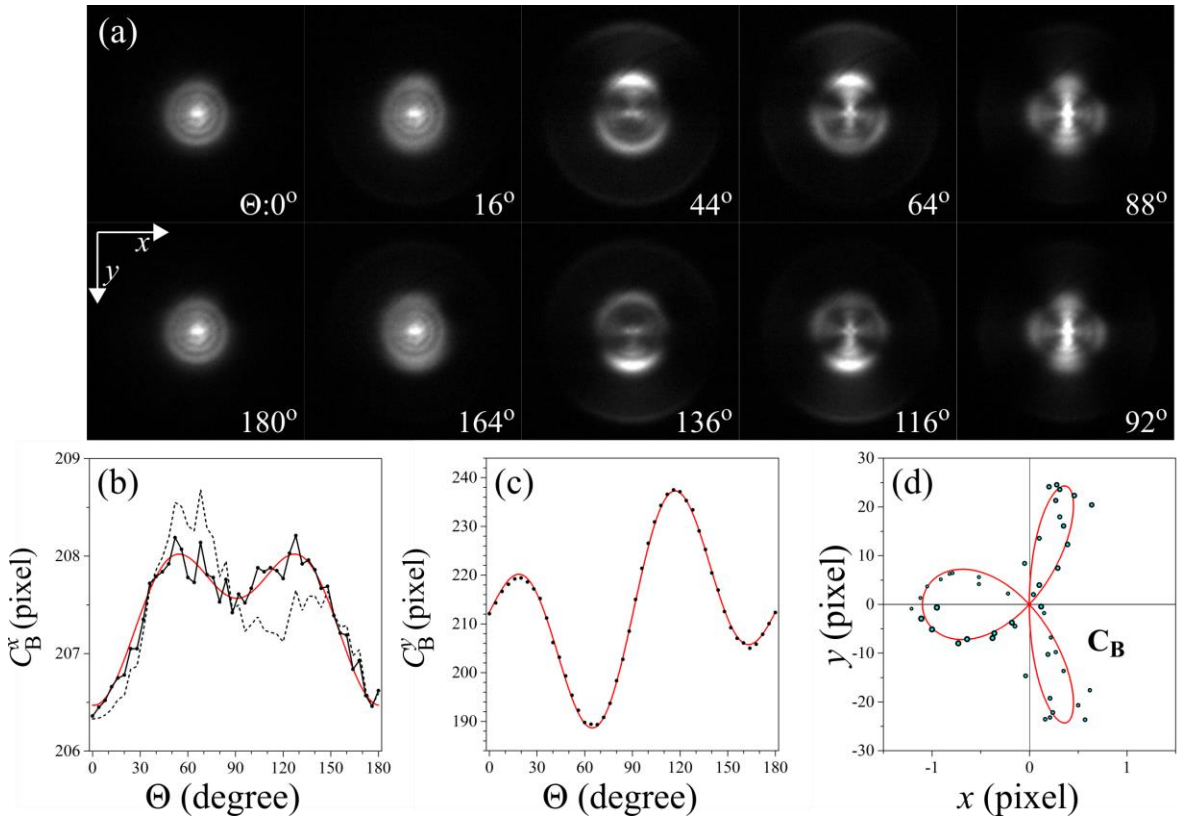

Figure 53. (a) Experimental non-resonant magnesium images for the two-photon excitation scheme out of the $3s^2$ ground state for an estimated static field value F=680±10V/cm and $\varepsilon\approx$–0.4. The horizontal and vertical axes refer to the x and y coordinates but note that the positive y-axis points downwards (typical convention of image-handling software packages). The laser beam propagates along x axis. The light polarization vector forms an angle Θ with the static field. (b) Barycenter in the x-coordinate before (black dashed line) and after (black solid line) the correction of the camera misalignment. Also shown the fitted curve (red solid line). (c) Same as (b) but for the y-coordinate. Higher y values signify the image barycenter moves downwards with respect to the image center. (d) The barycenter position in the cartesian coordinate space as Θ is varied (points of increasing size as Θ increases). Also shown is the position as predicted by the fitted curves of (b) and (c). We have verified that the images are reversed in the vertical direction for Θ'=π–Θ.

More specifically the barycenter in cartesian coordinates $C_{\mathrm{B}}^{x}(\Theta)$, $C_{\mathrm{B}}^{y}(\Theta)$ and $\mathbf{C}_{\mathrm{B}}$ are presented in Figure 53(b–d) respectively. First, note that C_{B}^{x} (black dashed line) of Figure 53(b) is asymmetric with respect to Θ=π/2 in contrast to the corresponding theoretical epectation (Eq. (94)). Experimentally, this effect is attributed to an additional misalignment between the detection reference frame and the laser beam. By employing this theoretically predicted symmetry of C_{B}^{x}, we found that the camera was tilted with respect to the laser beam by β=1.4° ±0.3° degrees. After rotating all images by –β we obtain the solid C_{B}^{x} curve of Figure 53(b), which is symmetrical with

respect to $\Theta=\pi/2$ (we do not present the rotated images because the visual effect is insignificant). Then we fit the $C_{\mathrm{B}}^{x}(\Theta)$, $C_{\mathrm{B}}^{y}(\Theta)$ curves using the forms of Eqs. (94,95) and additionally we allow the angle Θ to have an experimental uncertainty $\Delta\Theta$. The fit gives that $\Delta\Theta=0.88\pm0.07^{o}$ and $\Phi=-1.8\pm0.1^{o}$ degrees (see Figure 53(b,c)). The experimental data (points) and the fitted barycenter vector curve (red solid line) are shown in Figure 53(d). Note the huge difference in the scale of the vertical and horizontal axes. The experimental uncertainty $\Delta\Theta$ is compatible with the $\lambda/2$ waveplate rotation mount accuracy of 2^{o} (which leads to an accuracy of 4^{o} for the angle Θ).

In most applications the laser beam is aligned with external geometric procedures. In other words, these procedures do not consider the laser beam alignment with respect to the geometry of the VMI spectrometer electrodes. Moreover, the inhomogenous electric field of the VMI spectrometer in addition to the inaccurate knowledge of the exact position of the focused laser beam inside the spectrometer, introduces an uncertainty of the direction of the electric field vector. These facts may lead to misalignment angles of $|\Phi|\leq2^{o}$. A self-consistent alignment procedure as is the one shown here, that corrects the beam propagation vector with respect to the static electric field itself, could be very useful in typical VMI applications.

Outlook and Perspectives

The work presented in this thesis is devoted to a comprehensive photoionization microscopy study along three main directions. The first direction (that initially provided our major motivation) concerned the recording and characterization of resonant images in atoms of appreciable size. The intermediate complexity Mg atom (Z=12) was chosen as the target atom that was excited/ionized by two-photon absorption out of its ground state. Furthermore, in the course of this project two other directions emerged, each of equal importance to the first. Therefore, the second direction concerned the detailed recording of the (primarily non-resonant) momentum distributions of the outgoing electron transversely to the static electric field. The purpose here was the exploration of the global (i.e. of that met in any atom and irrespective of excitation conditions) information these distributions may provide through the analysis of their interference patterns. Finally, the third direction concerned the recording of slow photoelectron images when the linear polarization vector of the ionizing-laser is rotated with respect to the static field axis. Of particular interest here were the implications of the observed phenomena in tomographic angular distribution reconstruction techniques.

All the experimental data obtained in this work (and for any of the above directions) were fruitfully compared to relevant results of our theoretical calculations concerning the fundamental Coulomb-Stark problem. In fact, these calculations referred to all levels of rigor, beginning with the classical formulation of the hydrogenic Stark effect and proceeding to its semi-classical and fully quantum descriptions. Our theoretical modeling is based on the computationally advantageous semi-parabolic coordinate system and was found to support the experimental data. In addition, our theoretical treatment provided the proof-of-principle of several effects that may prove to be a guiding tool for future studies.

Below we briefly discuss the outlook of the present thesis and the perspectives emerging by it. For clarity, each of the aforementioned directions is discussed separately.

As a first step towards the search of non-hydrogenic resonant manifestations, we first employed our quantum hydrogenic theory to explore the most prominent energy range, lying just

above the saddle-point energy. Theoretically calculated electron current probability density distributions successfully reproduced the experimentally recorded hydrogenic resonant images [24]. These images present an additional dark fringe with respect to the nearby non-resonant images and a striking non-monotonic variation of the outer turning point. In fact, the energy evolution of the continuum images was found to be quite interesting as well. Consequently, their characteristics were additionally studied within this energy range around the resonances and in more detail than in earlier studies. As a main outcome, it was discovered that channel openings may frequently (but not always) lead to abrupt increases of the radial extensions of the images.

Having analyzed the above theoretical hydrogenic results, we subsequently presented a quite detailed experimental photoionization microscopy study of the two-photon excited Stark states of Mg just above the saddle-point energy range. As a first result of this study, the evolution of the angular distributions of the recorded magnesium images as a function of energy confirmed the long-ago predicted [58] existence of m-dependent saddle-point energies (one for m=0 and one for $|m|$= 2 in the present case). Furthermore, the outer turning points of the radial distributions of the images were overall found to monotonically increase with energy. Occasionally, however, they increased discontinuously and each observed jump signaled the opening of an n_1 channel, the latter becoming a continuum one. This behavior, therefore, was found to be in complete agreement with the aforementioned hydrogenic calculations in the energy range just above the saddle point limit. Interestingly, in the same energy range there were a number of cases where the outer turning points additionally showed a non-monotonic variation near the resonant maxima of the total ionization cross section. This variation was found to be due to an on-resonance appearance of an intensity halo at the outer part of the relevant images. The halo may be interpreted as an additional bright fringe, which is characteristic of the quasi- bound state participating non-negligibly to the photocurrent probability density. Moreover, resonant signatures on the recorded Mg images were apparently somewhat weaker than those in Li [21,22]. Leaving aside ionic-core size effects, this may be explained by the larger effective laser linewidth of the present study, as well as by the increased “parasitic” ionization signal stemming from the simultaneous excitation of the non-resonant m=0 contribution, in addition to the $|m|$=2 resonant and non-resonant contributions. On the contrary, excitation of single-$|m|$ Stark states was possible in the Li experiment.

On the perspectives side along this first direction, future experiments need to profit from the experience gained from the present as well as earlier studies. First, in order to unbury the resonant character from the recorded images, a number of precautions have to be taken and a number of special excitation strategies have to be devised. For example, it appears that the spectrally sharp Stark resonances require a spectral laser resolution much better than 0.8 cm^{-1}. Ideally, cw lasers (possibly pulsed amplified [99]) could be employed in conjunction with single-photon transitions, or, when necessary, multistep, multicolor, excitation schemes. In terms of the appropriate field strengths, the present study followed the earlier theoretical suggestions [33] and found indeed that there are values of F for which the resonant manifestations may be somewhat optimized. Nevertheless, the effect was much weaker than predicted. Clearly, working near avoided crossings, as in the He experiment [23], presents a quite promising direction, which appears to be potentially applicable to any non-hydrogenic atom. Finally, another interesting possibility is to achieve excitation near avoided crossings by means of bichromatic laser fields and apply phase-sensitive coherent control techniques. By employing such schemes, the continuum excitation could be minimized, in favor of the excitation of the quasi-bound states [121].

Along the second thesis direction, our attention was focused to m=0 transverse momentum distribution maps of the outgoing electron $R(\varepsilon,\rho)$ within the $-1\leq\varepsilon\leq+1$ energy range. The two-photon experimental maps revealed quite complex interference and beating patterns, particularly whenever the direct and indirect contributions to $R(\varepsilon,\rho)$ overlap. Most noticeable is the emergence of the so-called "checkerboard" pattern, first observed in hydrogen quite recently [34]. Our quantum theoretical treatment allowed for computing $R(\varepsilon,\rho)$ maps, for static electric fields whose strengths are small and compatible with current photoionization microscopy studies. Calculations included single- and two-photon excitation out of the ground state of hydrogen. The presented analysis suggested that near the ionization threshold a number of gross features of $R(\varepsilon,\rho)$ are common to all Rydberg atoms in the presence of a static electric field, appear irrespective of the initial state and excitation scheme and may be predicted by fairly simple semi-classical theoretical treatments [27]. That latter work provided a first global classification of direct-indirect beating phenomena. Furthermore, in recent theoretical works [53], many important details of the $R(\varepsilon,\rho)$ maps were washed out by the extreme static field strengths employed. These details have emerged in the present low-field work, revealing a much richer fringe structure, which depends fairly

strongly on the initial state, excitation scheme and the target atom (as the Mg experiment has shown).

Subsequently, attention was focused on the glory and primary rainbow signals of the $R(\varepsilon,\rho)$ maps and in particular, the quantum oscillations they exhibited. The $-1\leq\varepsilon\leq+1$ energy range was studied both experimentally and theoretically. These glory and bow signals present a rather complicated behavior in the negative energy range where resonances come also into play. On the contrary, in the positive energy range the absence of quasi-bound states range results to a fairly simple oscillatory pattern. As experimentally observed in the magnesium atom and also theoretically predicted for the hydrogen atom, this oscillatory pattern is characterized by a static-field and energy dependent "carrier periodicity" as well as beating maxima and minima. The exact positions of the latter, however, are atom- and excitation-scheme-dependent. In fact, these features concern only a small part of the aforementioned maps, but their study provides a first step towards the extraction of the full information contained in these maps. Following the recent theoretical work of Ref. [53], the connection between the energy locations of the static-field-induced-states (SFIS) and glory oscillations has been established within the semi-classical framework. Moreover, in the quest of novel approaches towards encoding electron dynamics, the time delay corresponding to pairs of trajectories has been extracted from the glory signals. The semi-classical and hydrogenic quantum calculations are in excellent agreement to the classically calculated time of flights. More importantly, the time delays which are extracted from the experimental Mg data agree with the aforementioned times of flight at least within the experimental uncertainty. This last result implies that the electron dynamics for $E>0$ are dominated by the long-range Coulomb-Stark field and weakly influenced by the ionic core (note that the core introduces observable zero-field phase shifts to the excited/outgoing electron wave-functions).

In future studies along this direction a multi-electron quantum mechanical theory should be able to predict the details of the glory and primary bow signals and particularly the beating maxima/minima. Semi-classical works that could calculate the electron time of flights, as modified by the non-hydrogenic core effects, could lead to very important results and could easily be tested with experimental data along the lines proposed here. Another interesting possibility is to study the energy range of doubly excited states. In that case, the electron dynamics of the ionized electron are expected to be greatly influenced by the inner excited electron thus, the glory signal may probe the electron-electron interactions.

Let us finally conclude with the third direction of the present work. Although the experimentally employed two-photon excitation/ionization scheme appears to slightly complicate the analysis of the recorded observables (as compared to a single-photon excitation one), it is proved to be more adequate for providing a solid testing ground for our theoretical study on the rotation of the linear laser polarization vector with respect to the static electric field axis. Indeed, the effects observed in non-resonant experimental images for the magnesium atom and for different polarization rotation angles Θ have been successfully reproduced theoretically. In the absence of misalignments, all images have vertical axis symmetry and show a complicated angular and radial distributions. The former distribution features a Θ-dependent *m*-beating effect due to the simultaneous excitation of $|m|=0,1,2$ final Stark states.

The above conclusions were strengthened by our findings on the total ionization cross section measurements. Specifically, by employing relevant complex-atom expressions for the total cross section it was made possible to identify and isolate the *m*-character of each spectral line. To this purpose, we made use of the fact that for the magnesium atom the zero-field $p\rightarrow s$ transitions are suppressed as compared to $p\rightarrow d$ ones [93]. Under this (valid) approximation the total ionization cross section may be decomposed into different-*m* contributions by simply recording two-photon spectra for three different angles Θ. As a cross check of the correctness of the above data treatment, synthetic spectra for arbitrary angles Θ were produced and successfully compared to experimental ones, recorded at the same angles. One result of particular importance concerns the clear identification of $|m|=1$ resonances, in both the decomposed contributions *and* the corresponding images recorded under the same conditions. Note that, strictly speaking, the *m*-decomposition is only relevant to the magnesium atom. It is valid, however, in any situation where the zero-field $p\rightarrow s$ transitions are very weak (which is a quite frequently the case [87]). Nevertheless, ab initio calculations would be required in order to accurately estimate the exact excitation strength ratio ($p\rightarrow s/p\rightarrow d$), for the general case.

As a byproduct application of our calculations we proposed (and successfully tested experimentally) a self-consistent method of laser beam and polarization alignment. The latter is based on the use of the image first moment and can be extended beyond the two-photon excitation scheme. The method may check the laser propagation axis and the angle Θ with high accuracy, a task that is of great interest in many applications other than slow photoelectron imaging.

Automatization of this method could provide a useful tool that could be integrated in imaging software.

The present experimental procedure of image recording at different angles Θ is closely related to tomographic techniques aiming at reproducing the 3-dimensional electronic momentum distribution. However, the non-negligible effects caused by the static electric field presence (making its inclusion to relevant calculations absolutely necessary) sets new challenges to these techniques. In short, since the *m*-composition of the outgoing electron flux depends on Θ, the "object" changes with the polarization rotation. Hence, it cannot be reconstructed by standard tomographic methods which assume the rotation of just a single object. Instead, a slow photoelectron tomographic theory is required, that includes both the static electric field and the coulomb center.

A possible, subsequent work on the subject could include the single photon excitation by employing elliptic polarization radiation. The π- and σ- selection rules will be the ones described for the simple single photon cases but the phase difference between the two orthogonal polarization vectors enters the interferogram. Experimentally controlling this phase difference (ellipticity) could provide phase information about the wave function.

Newly developed computational techniques such as a deep neural network algorithm could also be implemented in conjunction to the presently developed multielectron theory. The hybrid algorithm could be trained by computed images and then used to extract information of the experimental images. This is further aided by the form of the electron current density which is comprised by two unknown finite sets of non-hydrogenic matrix element magnitudes and phases (whose determination is an easy task for neural network codes).

The strength of photoionization microscopy lies in the spatial resolution of electronic interference patterns. Thus, limiting its use solely in imaging of resonant Stark states hinders the rich capabilities of the method. At this point, the conjunction of PM with other experimental techniques seems to be the most prominent perspective. We believe that the present study shed new light upon previously unexplored features of both resonant and particularly non-resonant images and suggested a number of novel approaches that aim at extracting information from the photoionization microscopy interferogram. The discussed perspectives of the present work, along with earlier ones call for additional photoionization microscopy experiments. For example, one of

the first applications of photoionization microscopy, as proposed by its inventors, was the study of the Bohm-Aharonov effect [11]. In fact, the authors concluded that the glory signal would act as a sensitive detector of magnetic fields. The effects of parallel electric and magnetic fields on the radial distributions were also theoretically studied by the authors of Ref. [122]. The PM setup could indeed be used for magnetic field sensing purposes but the sensitivity could be greatly affected by our accuracy in determining other parameters, such as the electric field strength and the excitation energy (assuming that atom-specific complexities are ignored). Photoionization microscopy of hydrogen atom in a non-uniform electrical field in the *z* coordinate was treated in Ref. [123]. Note that, the VMIS electrode geometry produces inhomogeneous electric fields but the gradient of the electric field should be high enough in order to have an impact on the trajectories near the Coulomb center, <5 μm, and on the same time the laser-atom interaction region should be kept smaller than this value, at least in the *z* coordinate. The substitution of the static electric field with a slow-varying time dependent one [53], is an interesting but experimentally challenging photoionization microscopy variant. The interest of such works lies in the characteristics of the low-lying states characteristics (position, width, lifetime etc.) which are strongly affected by the presence of a strong quasi-static electric field, a subject of great interest in strong field physics. Last but not least, PM near a metal [124] or dielectric surface [125] can be employed in the study of the surface characteristics (dielectric constant etc.) or manipulate the ionization time delays experimentally.

References

[1] J. Repp, G. Meyer, S.M. Stojkovic, A. Gourdon, and C. Joachim, Phys. Rev. Lett. **94**, 026803 (2005).

[2] M. Feng, J. Zhao, and H. Petek, Science **320**, 359 (2008).

[3] P. Puschnig, S. Berkedile, A.J. Flemming, G. Koller, K. Emtsev, T. Seyller, J.D. Riley, C. Ambrosch-Draxl, F.P. Netzer and M. Ramsey, Science **326**, 702 (2009).

[4] D. Shafir, Y. Mairesse, D.M. Villeneuve, P.B. Corkum and N. Dudovich, Nature Physics **5**, 412 (2009).

[5] J. Itatani, J. Levesque, D. Zeidler, H. Niikura, H. Pépin, J.C. Kieffer, P.B. Corkum, and D.M. Villeneuve, Nature **432**, 867 (2004).

[6] Y. Aharonov, D.Z. Albert, L. Vaidman, Phys. Rev. Lett. **60**, 1351 (1988).

[7] S. Kocsis, B. Braverman, S. Ravets, M.J. Stevens, R.P. Mirin, L.K. Shalm, A.M. Steinberg, Science **332**, 1170 (2011).

[8] J.S. Lundeen, B. Sutherland, A. Patel, C. Stewart, and C. Bamber, Nature **474**, 188 (2011).

[9] Y. N. Demkov, V. D. Kondratovich, and V. N. Ostrovskii, JETP Lett. **34**, 403 (1981).

[10] V. D. Kondratovich and V. N. Ostrovsky, J. Phys. B **17**, 1981 (1984); **17**, 2011 (1984); **23**, 21 (1990).

[11] V. D. Kondratovich and V. N. Ostrovsky, J. Phys. B **23**, 3785 (1990).

[12] I. I. Fabrikant, Z. Eksp. Teor. Fiz. **79**, 2070 (1980) [Sov. Phys. JETP **52**, 1045 (1980)].

[13] H. A. Bethe and E. E. Salpeter, Quantum Mechanics of One andTwo-Electron Atoms (Springer, Berlin, 1957), and references therein.

[14] T. F. Gallagher, Rydberg Atoms (Cambridge University Press, Cambridge, 1994), and references therein.

[15] C. Nicole, I. Sluimer, F. Rosca-Pruna, M. Warntjes, M. J. J. Vrakking, C. Bordas, F. Texier, and F. Robicheaux, Phys. Rev. Lett. **85**, 4024 (2000).

[16] C. Bordas, Phys. Rev. A **58**, 400 (1998).

[17] C. Blondel, C. Delsart, and F. Dulieu, Phys. Rev. Lett. **77**, 3755 (1996).

[18] C. Nicole, H.L. Offerhaus, M.J.J. Vrakking, F. Lépine, and C. Bordas, Phys. Rev. Lett. **88**, 133001 (2002).

[19] C. Bordas, F. Lépine, C. Nicole and M.J.J. Vrakking, Phys. Rev. A **68**, 012709 (2003).

[20] F. Lépine, C. Bordas, C. Nicole and M.J.J. Vrakking, Phys. Rev. A **70**, 033417 (2004).

[21] S. Cohen, M. M. Harb, A. Ollagnier, F. Robicheaux, M. J. J. Vrakking, T. Barillot, F. Lépine, and C. Bordas, Phys. Rev. Lett. **110**, 183001 (2013).

[22] S. Cohen, M. M. Harb, A. Ollagnier, F. Robicheaux, M. J. J. Vrakking, T. Barillot, F. Lépine, and C. Bordas, Phys. Rev. A **94**, 013414 (2016).

[23] A. S. Stodolna, F. Lépine, T. Bergeman, F. Robicheaux, A. Gijsbertsen, J. H. Jungmann, C. Bordas, and M. J. J. Vrakking, Phys. Rev. Lett. **113**, 103002 (2014).

[24] A. S. Stodolna, A. Rouzée, F. Lépine, S. Cohen, F. Robicheaux, A. Gijsbertsen, J. H. Jungmann, C. Bordas, and M. J. J. Vrakking, Phys.Rev.Lett. **110**, 213001 (2013).

[25] L. B. Zhao and J. B. Delos, Phys.Rev.A **81**, 053418 (2010).

[26] L. B. Zhao, D. H. Xiao and I. I. Fabrikant, Phys.Rev.A **91**, 043405 (2015).

[27] P. Kalaitzis, S. Danakas, F. Lépine, C. Bordas and S. Cohen, Phys.Rev.A **97**, 053412 (2018).

[28] M. L. Zimmerman, M. G. Littman, M. M. Kash, and D. Kleppner, Phys. Rev. A **20**, 2251 (1979); S. Feneuille, S. Liberman, E. Luc-Koenig, J. Pinard, and A. Taleb, J. Phys. B **15**, 1205 (1982); J. Y. Liu, P. McNicholl, D. A. Harmin, J. Ivri, T. Bergeman, and H. J. Metcalf, Phys.Rev.Lett. **55**, 189 (1985); P. McNicholl, T. Bergeman, and H. J. Metcalf, Phys.Rev.A **37**, 3302 (1988).

[29] L. B. Zhao, I. I. Fabrikant, J. B. Delos, F. Lépine, S. Cohen and C. Bordas, Phys.Rev.A **85**, 053421 (2012)

[30] F. Texier, Phys.Rev.A **71**, 013403 (2005).

[31] L. B. Zhao, I. I. Fabrikant, M. L. Du and C. Bordas, Phys.Rev.A **86**, 053413 (2012)

[32] P. Giannakeas, F. Robicheaux, and C. H. Greene, Phys. Rev. A **91**, 043424 (2015).

[33] L. B. Zhao, Europhysics Lett. **109**, 23002 (2015).

[34] A. S. Stodolna, F. Lépine, A. Rouzée, S. Cohen, A. Gijsbertsen, J. H. Jungmann-Smith, C. Bordas and M. J. J. Vrakking, J. Phys. B **50**, 164001 (2017).

[35] E. Diesen, U. Saalmann, M. Richter, M. Kunitski, R. Dörner and J. M. Rost, Phys.Rev.Lett. **116**, 143006 (2016).

[36] S. D. López and D. G. Arbó, Phys. Rev. A **100**, 023419 (2019).

[37] X. Y. Lai, S. G. Yu, Y. Y. Huang, L. Q. Hua, C. Gong, W. Quan, C. F. de Morisson Faria, and X. J. Liu, Phys.Rev.A **96**, 013414 (2017).

[38] G. M. Lankhuijzen and L. D. Noordam, Phys. Rev. Lett. **76**, 1784 (1996).

[39] K. Klünder, J. M. Dahlstrom, M. Gisselbrecht, T. Fordell, M. Swoboda, D. Guénot, P. Johnsson, J. Caillat, J. Mauritsson, A. Maquet, R. Taıeb, and A. L'Huillier, Phys. Rev. Lett. **106**, 143002 (2011).

[40] J. Mauritsson, T. Remetter, M. Swoboda, K. Klünder, A. L'Huillier, K. J. Schafer, O. Ghafur, F. Kelkensberg, W. Siu, P. Johnsson, M. J. J. Vrakking, I. Znakovskaya, T. Uphues, S. Zherebtsov, M. F. Kling, F. Lépine, E. Benedetti, F. Ferrari, G. Sansone, and M. Nisoli, Phys. Rev. Lett. **105**, 053001 (2010).

[41] L. D. Landau and E. M. Lifshitz, Quantum Mechanics: Non-relativistic Theory (Pergamon, New York, 1965).

[42] H. Rottke and K. H. Welge, Phys. Rev. A **33**, 301 (1986).

[43] C. Smeenk, L. Arissian, A. Staudte, D. M. Villeneuve and P. B. Corkum, J. Phys. B **42**, 185402 (2009).

[44] C. Bordas, F. Pauling, H. Helm and D. L. Huestis, Rev. Sci. Instrum. **67**, 2257 (1996).

[45] V. Schyja, T. Lang, and H. Helm, Phys. Rev. A **57**, 3692 (1998).

[46] R. Wiehle, B. Witzel, H. Helm and E. Cormier, Phys. Rev. A **67**, 063405 (2003).

[47] S. J. Smith and G. Leuchs, Advances in Atomic and Molecular Physics, Volume **24**, (Academic Press Inc., 1988).

[48] M. Wollenhaupt, M. Krug, J. Köhler, T. Bayer, C. Sarpe-Tudoran and T. Baumert, Appl. Phys. B **95**, 647 (2009).

[49] P. Hockett, M. Wollenhaupt, C. Lux, and T. Baumert, Phys. Rev. Lett. **112**, 223001 (2014).

[50] T. Barillot, R. Brédy, G. Celep, S. Cohen, I. Compagnon, B. Concina, E. Constant, S. Danakas, P. Kalaitzis, G. Karras, F. Lépine, V. Loriot, A. Marciniak, G. Predelus-Renois, B. Schindler and C. Bordas, J. Chem. Phys. **147**, 013929 (2017).

[51] L. B. Zhao and J. B. Delos, Phys. Rev. A **81**, 053417 (2010).

[52] S. Cohen, P. Kalaitzis, S. Danakas, F. Lépine and C. Bordas, J. Phys. B **50**, 065002 (2017).

[53] S. Ohgoda, O. I. Tolstikhin and T. Morishita, Phys. Rev. A **95**, 043417 (2017).

[54] V. V. Beletsky, Essays on the Motion of Celestial Bodies (Birkhäuser Verlag, Basel, Switzerland, 2001).

[55] G. Lantoine and R. P. Russell, Celest. Mech. Dyn. Astr. **109**, 333 (2011).

[56] C. Blondel, C. Delsart, F. Dulieu and C. Valli, Eur. Phys. J. D **5**, 207 (1999).

[57] M. V. Berry, Contemp. Phys. **56**, 2 (2015).

[58] W. E. Cooke and T. F. Gallagher, Phys. Rev. A **17**, 1226 (1978); M. G. Littman, M. M. Kash, and D. Kleppner, Phys. Rev. Lett. **41**, 103 (1978).

[59] M. L. Du and J. B. Delos, Phys. Rev. A **38**, 1913 (1988).

[60] V. V. Kolosov, Pis'ma Zh. Eksp. Teor. Fiz. **44**, 457 (1986) [Sov. Phys. JETP Lett. **44**, 588 (1986)].

[61] A. V. Gets and O. I. Tolstikhin, Phys. Rev. A **87**, 013419 (2013).

[62] D. A. Harmin, Phys. Rev. A **24**, 2491 (1981); **26**, 2656 (1982).

[63] E. Luc-Koenig and A. Bachelier, J. Phys. B **13**, 1743 (1980); **13**, 1769 (1980).

[64] R. R. Freeman, N. P. Economou, G. C. Bjorklund and K. T. Lu, Phys. Rev. Lett. **41**, 1463 (1978); R. R. Freeman and N. P. Economou, Phys. Rev. A **20**, 2356 (1979).

[65] A. K. Kazansky, V. N. Ostrovsky and D. A. Telnov, J. Phys. B **23**, L433 (1990).

[66] J. Gao, J. B. Delos and M. Baruch, Phys. Rev. A **46**, 1449 (1992); **46**, 1455 (1992).

[67] W. L. Glab and M. H.Nayfeh, Phys. Rev. A **31**, 530 (1985).

[68] J. I. Lo, C. C. Chu, H. S. Fung, Y. Y. Lee, and T. S. Yih, Chinese J. Phys. **51**, 56 (2013).

[69] J. W. Cooper and E. B. Solaman, Phys. Rev. A **26**, 1452 (1982).

[70] P. Kalaitzis, S. Danakas, C. Bordas and S. Cohen, Phys. Rev. A **99**, 023428 (2019).

[71] S. Watanabe, Phys. Rev. A **126**, 107 (1987).

[72] R. Gaillac, M. Vacher,A. Maquet, R. Taïeb and J. Caillat, Phys. Rev. A **93**, 013410 (2016).

[73] R. J. Damburg and V. V. Kolosov, J. Phys. B **9**, 3149 (1976).

[74] A. Alijah, J. T. Broad and J. Hinze, J. Phys. B **19**, 2617 (1986).

[75] G. Alvarez, R. J. Damburg and H. J. Silverstone, Phys. Rev. A **44**, 3060 (1991).

[76] A. Alijah, J. Phys. B **25**, 5043 (1992).

[77] L. Fernández-Menchero and H. P. Summers, Phys. Rev. A **88**, 022509 (2013).

[78] V. I. Osherov and V. G. Ushakov, Phys. Rev. A **90**, 045401 (2014); **95**, 023419 (2017).

[79] H. Cartarius, J. Main, T. Losch and G.Wunner, Phys. Rev. A **81**, 063414 (2010).

[80] P. A. Batishchev, O. I. Tolstikhin and T. Morishita, Phys. Rev. A **82**, 023416 (2010).

[81] W. E. Milne, Phys. Rev. **35**, 863 (1930).

[82] A. Dalgarno and J. T. Lewis, Proc. R. Soc. London, Ser. A **233**, 70 (1955).

[83] E. S. Toma and H. G. Muller, J. Phys. B **35**, 3435 (2002).

[84] T. Topçu and F. Robicheaux, J. Phys. B **40**, 1925 (2007).

[85] C. Bracher, T. Kramer, M. Kleber, Phys. Rev. A **67**, 043601 (2003); T. Kramer, C. Bracher and M. Kleber, J. Phys. A: Math. Gen. **35**, 8361 (2002).

[86] H. Friedrich, Theoretical Atomic Physics (Springer-Verlag Berlin Heidelberg, 1990)

[87] R. D. Cowan, The Theory of Atomic Structure and Spectra (University of California Press, 1981).

[88] M. Aymar, C. H. Greene and E. Luc-Koenig, Rev. Mod. Phys. **68**, 1015 (1996).

[89] A. Dimitriou, Published doctoral dissertation (University of Ioannina, Ioannina, Greece, 2013).

[90] M. J. Seaton, Rep. Prog. Phys. **46**, 167 (1983).

[91] U. Fano, Phys. Rev. A **24**, 619 (1981).

[92] D. A. Harmin, Phys. Rev. Lett. **49**, 128 (1982); **30**, 2413 (1984).

[93] M. Rafiq, M. A. Kalyar and M. A. Baig, J. Phys. B **40**, 3181 (2007).

[94] A. T. J. B. Eppink and D. H. Parker, Rev. Sci. Instrum. **68**, 3477 (1997).

[95] M. M. Harb, S. Cohen, E. Papalazarou, F. Lépine and C. Bordas, Rev. Sci. Instrum. **81**, 125111 (2010).

[96] H. L. Offerhaus, C. Nicole, F. Lépine, C. Bordas, F. Rosca-Pruna, and M. J. J. Vrakking, Rev. Sci. Instrum. **72**, 3245 (2001).

[97] H. Liebl, Applied Charged Particle Optics (Springer-Verlag Berlin, Heidelberg, 2008)

[98] Lambda Physik ScanMate 2EC-400 dye laser, user manual.

[99] W. Demtröder, Atoms, Molecules and Photons (Springer Berlin Heidelberg, New York, 2006).

[100] U. Brackmann, Lambdachrome® Laser Dyes (Lambda Physik AG, Goettingen, Germany, 2000).

[101] T. J. McKee, J. Lobin and W. A. Young, Applied Optics **21**, 725 (1982).

[102] R. W. Boyd, Nonlinear Optics: Third Edition (Academic Press, 2008).

[103] K. C. Smyth and P. K. Schenk, Chem. Phys. Lett. **55**, 466 (1978).

[104] A. Kramida, Yu. Ralchenko, J. Reader and NIST ASD Team, NIST Atomic Spectra Database (ver. 5.6.1) (2018).

[105] A. A. Voronin & A. M. Zheltikov, Sci. Rep. **7**, 46111 (2017).

[106] D. W. Chandler, P. L. Houston and D. H. Parker, Review J. Chem. Phys. **147**, 013601 (2017).

[107] D. W. Chandler and P. L. Houston, J. Chem. Phys. **87**, 1445 (1987).

[108] A. J. R. Heck and D. W. Chandler, Annu. Rev. Phys. Chem. **46**, 335 (1995).

[109] M. Vrakking, Rev. Sci. Instrum. **72**, 4084 (2001).

[110] D. A. Chestakov, S. M. Wu, G. Wu, D. Parker, A. T. J. B. Eppink, and T. N. Kistopoulos, J. Phys. Chem. A **108**, 8100 (2004).

[111] D. Strasser, X. Urbain, H. B. Pedersen, N. Altstein, O. Heber, R. Wester, K. G. Bhushan and D. Zajfman, Rev. Sci. Instrum. **71**, 3092 (2000).

[112] V. Koulianou, Unpublished bachelor dissertation (University of Ioannina, Ioannina, Greece, 2017).

[113] G. Scoles, Atomic and Molecular Beam Methods (Oxford University Press, 1988).

[114] https://imagej.nih.gov/ij/plugins/index.html

[115] A. Koulouklidis, Unpublished master dissertation (University of Ioannina, Ioannina, Greece, 2010).

[116] E. Pavlou, Unpublished master dissertation (University of Ioannina, Ioannina, Greece, 2012).

[117] M. H. Rice and R. H. Good, J. Opt. Soc. Am. **52**, 239 (1962).

[118] K. Botsiou, Unpublished bachelor dissertation (University of Ioannina, Ioannina, Greece, 2016).

[119] T. F. Gallagher, L. M. Humphrey, W. E. Cooke, R. M. Hill, and S. A. Edelstein, Phys. Rev. A **16**, 1098 (1977); J. L. Vialle and H. T. Duong, J. Phys. B **12**, 1407 (1979).

[120] R. B. Blackman and J. W. Tukey, The Bell System Technical Journal **37**, 185 (1958).

[121] S. Cohen, J. Phys. B **44**, 205402 (2011).

[122] M. Deng, W. Gao, Rong Lu, J. B. Delos, L. You and H. P. Liu, Phys. Rev. A **93**, 063411 (2016).

[123] S. H. Cheng, D. H. Wang, Z. H. Chen, and Q. Chen, Chin. Phys. B **25**, 063201 (2016).

[124] H.F. Yang, L. Wang, X.J. Liu and H.P. Liu, Chin. Phys. B **20**, 063203 (2011).

[125] Q. Chen and D. Wang, Philosophical Magazine **95**, 3712 (2015).